ISTANBUL TECHNICAL UNIVERSITY ★ GRADUATE SCHOOL

MISSION MANAGEMENT AND CONTROL FOR CUBESATELLITES

M.Sc. THESIS

Aybüke Ağırbaş

Department of Aeronautical and Astronautical Engineering

Aeronautical and Astronautical Engineering Programme

OCTOBER 2024

ISTANBUL TECHNICAL UNIVERSITY ★ GRADUATE SCHOOL

MISSION MANAGEMENT AND CONTROL FOR CUBESATELLITES

M.Sc. THESIS

Aybüke Ağırbaş
(511211110)

Department of Aeronautical and Astronautical Engineering

Aeronautical and Astronautical Engineering Programme

Thesis Advisor: Prof. Dr. Alim Rüstem ASLAN

OCTOBER 2024

İSTANBUL TEKNİK ÜNİVERSİTESİ ★ LİSANSÜSTÜ EĞİTİM ENSTİTÜSÜ

YETENEKLİ KÜP UYDULAR İÇİN GÖREV YÖNETİMİ VE KONTROLÜ

YÜKSEK LİSANS TEZİ

Aybüke Ağırbaş
(511211110)

Uçak ve Uzay Mühendisliği Ana Bilim Dalı

Uçak ve Uzay Mühendisliği Programı

Tez Danışmanı: Prof. Dr. Alim Rüstem ASLAN

EKİM 2024

Aybüke Ağırbaş, a M.Sc. student of İTU Graduate School student ID 511211110, successfully defended the thesis/dissertation entitled "MISSION MANAGEMENT AND CONTROL FOR CUBESATELLITES", which he/she prepared after fulfilling the requirements specified in the associated legislations, before the jury whose signatures are below.

Thesis Advisor : **Prof. Dr. Alim Rüstem Aslan** ....
Istanbul Technical University

Jury Members : **Prof. Dr. Cengiz Hacızade** ....
Istanbul Technical University

Assist. Prof. Dr. Tuncay Yunus Erkeç ....
National Defence University

Date of Submission : 26 September 2024
Date of Defense : 01 October 2024

“Keep a little fire burning; however small, however hidden.”
- Cormac McCarthy

FOREWORD

I would like to express my sincere gratitude to Prof Dr. Alim Rüstem Aslan for his invaluable support and guidance during my graduate studies. I am deeply grateful for his mentorship and encouragement.

I would like to express my sincere gratitude to all professors of Faculty of Aeronautics and Astronautics.

I would also like to thank my colleagues, members of the Space Systems Design and Testing Laboratory: MSc. Barış BEYNEK, BSc. Bilge MEMİŞ, MSc. Boğaç KARABULUT, MSc. Egemen ÇATAL, MSc. Emirhan Eser GÜL, Kaan GÖKTÜRK, MSc. Kaan SARICA, MSc. Mehreen AZAM, MSc. Onur ÖZTEKİN, Rümeysa ÜSTÜNCAN for their support and assistance during the course of my research.

2024 Aybüke Ağırbaş
Astronautical Engineer

TABLE OF CONTENTS

Page

ABBREVIATIONS

ADCS	: Attitude Determination and Control System
AFSK	: Audio Frequency-Shift Keying
ASM	: Attached Sync Marker
CAN	: Controller Area Network
CCD	: Charge-couple device
CMOS	: Complementary Metal-Oxide Semiconductor
CoG	: Centre of Gravity
CoM	: Centre of mass
CSS	: Coarse Sun Sensor
dB	: Decibel
DEC	: Declination
ECEF	: Earth Centred Earth Fixed
ECI	: Earth Centred Inertial
EDM	: Electrical Discharge Machining
EKF	: Extended Kalman Filter
EPS	: Electrical Power System
EQM	: Engineering Qualification Model
ESOQ	: Estimator of the Optimal Quaternion
FOAM	: Fast Optimal Attitude Matrix
FoV	: Field of View
FSS	: Fine Sun Sensor
GMSK	: Gaussian Minimum Shift Keying
GS	: Ground Station
GSD	: Ground Sampling Distance
GPS	: Global Positioning System
HPOP	: High Precision Orbit Propagator
I2C	: Inter-Integrated Circuit
IGRF	: International Geomagnetic Reference Field (IGRF)
ITU	: Istanbul Technical University
iXRD	: improved X-ray Detector
LEO	: Low Earth Orbit
LEOP	: Launch and early Operation Phase
LTDN	: Local Time on Descending Node
MB	: Mega-byte
MEMS	: Micro-electromechanical System
MP	: Mega-pixel
OBC	: On Board Computer
OQPSK	: Offset Quadrature Phase-Shift Keying
QPSK	: Quadrature Phase Shift Keying
QUEST	: Quaternion Estimator
RA	: Right Ascension

RF	: Radio Frequency
SAA	: South Atlantic Anomaly
SAASST	: Sharjah Academy for Astronomy, Space Sciences, and Technology
SGP4	: Simplified General Perturbations 4
SPI	: Serial Peripheral Interface
SSDTL	: Space Systems Design and Test Laboratory
SSO	: Sun Synchronous Orbit
SU	: Sabancı University
SVD	: Single Value Decomposition
SW	: Software
TC	: Telecommand
TLE	: Two Line Element
TLM	: Telemetry
TRIAD	: Triaxial Attitude Determination
U	: Unit
UART	: Universal Asynchronous Receiver / Transmitter
UHF	: Ultra High Frequency
VHF	: Very High Frequency

SYMBOLS

C_D : Drag Coefficient
C_R : Solar Radiation Coefficient
^{o} : Degree
W : Watt
km : Kilometre

LIST OF TABLES

Page

LIST OF FIGURES

Page

MISSION MANAGEMENT AND CONTROL FOR CUBESATELLITES

SUMMARY

Here in this thesis mission management and control for a CubeSat from attitude determination and control perspective is explained.

First, the purpose of the thesis is presented, followed by a literature review of CubeSats and attitude determination methods.

Secondly, a 3U+ CubeSat, SharjahSat-1, mission overview and the system block diagram which includes all the subsystems within the CubeSat are presented. Then, each subsystem within the CubeSat is explained briefly. This section includes main payload, secondary payload, structures and mechanisms, on-board command and data handling system, communication system, electrical power system (EPS), attitude determination and control system (ADCS) are presented. The orbital analyses including lifetime, power generation, star access, and camera access analyses, and the system budgets including, mass, power, data, and link budgets are presented in order to give a clear understanding for the subsystem requirements. Then general operation phases of the SharjahSat-1 are explained. These include Launch and Early Operation Phase (LEOP), normal operation phase, safe operation phase and mission specific operation phases. At the end of this section, the ground station (GS) interface prepared specifically for the SharjahSat-1 mission is presented.

Thirdly, attitude determination algorithms and sensors used in this study are presented. Following that, attitude determination and control in SharjahSat-1 is explained in detail. Some of the sensor performances on different control modes are discussed. Also, the telecommands and telemetries related to ADCS operations in the GS is explained. At the end of this section, ADCS flowcharts that are implemented in SharjahSat-1 operations, are explained briefly.

In the next section, current condition of the SharjahSat-1 in the orbit is explained. The mission current mission scenarios based on the data received from the SharjahSat-1 in orbit and the performance of the satellite is discussed.

Then, the findings from the data collected in orbit and the results from the attitude determination algorithm used in the study is compared and discussed.

Lastly, the conclusion of the thesis is presented.

YETENEKLİ KÜP UYDULAR İÇİN GÖREV YÖNETİMİ VE KONTROLÜ

ÖZET

Bu tezde bir KüpUydu'nun görev yönetimi ve kontrolü yönelim belirleme ve kontrol perspektifinden anlatılmaktadır.

Öncelikle tezde ele alınan 3U+ boyutlarındaki, Sharjah Astronomi, Uzay Bilimleri ve Teknoloji Akademisi, Uzay Sistemleri Tasarım ve Test Laboratuvarı ve Sabancı Üniversitesi iş birliğinde geliştirilen SharjahSat-1 küpuydusuna dair genel bilgiler sunulmuştur. Alçak Dünya yörüngesine yerleştirilmiş bu uydunun 2 görev yükü bulunmakta ve bunlar Sabancı Üniversitesi tarafından geliştirilen geliştirilmiş X-ışını dedektörü ve Uzay Sistemleri Tasarım ve Test Laboratuvarı tarafından yerleştirilen ikili kamera sistemidir. Yönelim belirleme ve kontol sisteminin iki görev yükü için de beklenen performansta çalışmasının önemi, devam eden bölümlerdeki KüpUydular ve yönelim belirleme üzerine yapılmış olan literatür taramasıyla da desteklenmiştir. KüpUyduların kütle, hacim, performans ve maliyet açısından ne kadar avantajlı olduğu belirtilmiş ayrıca bu uydularda kullanılabilecek yönelim belirleme sensörlerine, bunlarla birlikte kullanılabilecek yönelim belirleme algoritmalarına ve bunların performans açısından karşılaştırılmasına yer verilmiştir.

İkinci bölümde, SharjahSat-1 görevine daha detaylı bir şekilde değinilmiştir. SharjahSat-1 üstünde geliştirilmiş x-ışını dedektörü, ikili kamera sistemi, elektrik güç sistemi, iletişim sistemi, uydu bilgisayarı, yönelim belirleme ve kontrol sistemi ve arayüz kartı olmak üzere çeşitli altsistemi bulundurmaktadır. Ana görev yükü olan geliştirilmiş x-ışını dedektörünün kullaım amacı, dedektörü belirli parlak galaktik x-ışın kaynaklarına yöneltip ölçüm olarak bunların durumlarını gözlemlemek veya Güneşe yönlendirip ölçüm alarak meydana gelen Güneş patlamalarına ait x-ışını spektrumlarını ve Güneş koronal deliklerini gözlemlemektir. İkincil görev yükü olan ikili kamera sisteminin amacı ise alçak Dünya yörüngesinden yer gözlemi yapmaktır. Uydudaki görev yükleriyle diğer sistemleri, yapı ve mekanizma elemanları bir arada tutmaktadır. Ayrıca bu elemanlar uydunun çevresel testleri sırasında karşılaması gereken isterleri de karşılamaktadır. Uydu bilgisayarı, uydu sistemlerinin görev kontrolü için kullanılır, ayrıca çeşitli iletişim arayüzleri ve çevresel işlevler sunar. İletişim sistemi olarak 2 farklı sistem kullanılmaktadır. Bunlardan ilki çok yüksek frekans ve ultra yüksek frekans alıcı-vericis ve diğeri de S-band frekansı vericisi. Bu iki iletişim sistemi için bulunan modemler, yer istasyonuyla uydu bilgisayarı arasındaki iletişimin kurulmasını sağlamaktadır. Kurulan iletişim sayesinde bir yandan uydu sistemlerinin sağlık verilerine, uydunun yönelim bilgisine, sensör ölçümlerine ulaşılırken öbür yandan yer istasyonundan uyduya bilgisayarına komut gönderilebilmektedir. Elektrik ve güç sistemi, Güneş paneli hücreleri aracılığıyla güç üretiminden ve üretilen gücün bataryalarda depolanıp sistemlerin tüketim gereksinimlerine göre dağıtılıp kullanılmasından sorumludur. Sistem elektrik güç yönetim birimi, 25 güneş paneli hücresi ve 3 bataryadan oluşmaktadır. Yönelim belirleme ve kontrol sistemi kapsamında çeşitli sensör ve kontrolcülerle birlikte bunlardan gelen verileri işleyip kullanan bir yönelim belirleme ve kontrol bilgisayarı

da bulunmaktadır. Sistemde yönelim belirlemek için biri yedek 2 manyetometre, 10 kaba güneş sensörü, hassas Güneş sensörü, ufuk sensörü, açısal hız sensörü, yıldız izler sensörü bulunmaktadır. Yönelim kontrolü için de 3 reaksiyon tekeri ve aktif manyetik kontrol kullanılmaktadır. Uydunun görev ve sistem gereksinimlerinin detaylı olarak tanımlanabilmesi için çeşitli yörünge analizleri yapılmıştır. Ömür, güç üretimi, yıldız erişim ve kamera erişim analizlerini içeren yörünge analizleri ile kütle, güç, veri ve iletişim bütçelerini içeren sistem bütçeleri, alt sistem gereksinimlerini net bir şekilde tanımlanmıştır. Uydunun ömür analizi sonucu 2035 sonrasına kadar yörüngede kalacağı görülmektedir. Güç analizi sonuçlarına göre bir yörüngede üretilen ortalama güç en az 3.704 watt olarak bulunmuştur. Yıldız erişim ve kamera erişim analizleri sonuçlarına göre 2 görev yüküyle de rahatça görev gerçekleştirilebilecek zaman aralıkları bulunmaktadır. Analiz sonuçları, sonrasında sunulmuş olan kütle, güç, veri ve link bütçeleriyle uyuşmaktadır. Bölümün devamında uydu bilgisayarı tarafında tanımlanan genel operasyon fazlarından bahsedilmektedir. Fırlatma ve erken operasyon fazı, normal operasyon fazı, güvenli operasyon fazı, iki görev yükü için de ayrı ayrı tanımlanmış görev fazları adım adım verilmiştir. Son olarak SharjahSat-1 yer istasyonu uygulamasıyla ilgili bilgiler paylaşılmıştır.

Üçüncü kısımda olarak bu çalışmada kullanılan yönelim belirleme algoritmaları ve sensörleri sunulmaktadır. Proje bazında yönelim belirlemek için kullanılmak üzere literatür taramasında değinilen TRIAD ve QUEST algoritmaları seçilmiştir. Bu algoritmaların işleyişlerine ve hesaplamalarına dair bilgiler paylaşılmıştır. Hem proje içinde kullanılabilecek hem de SharjahSat-1 üzerinde bulunan sensörlerden üçü kullanılmak üzere seçilmiştir. Seçilen Güneş sensörleri, manyetometre ve ufuk sensörleri için algoritmalarda kullanılmak üzere sensörlerin tahmini hata payları göz önünde bulundurularak sensör modelleri oluşturulmuştur. Bölümün devamında SharjahSat-1'de kullanılan yönelim belirleme ve kontrol sistemi detaylıca anlatılmaktadır. Uydunun üzerindeki yönelim belirleme sensörlerinin yerleşimi verilmiş. Sistemin içinde tanımlanmış yönelim belirleme ve kontrol modları sırayla paylaşılmıştır. Farklı yönelim belirleme ve kontrol modlarına yönelik sistemin performansını inceleme amacıyla yapılan simulasyonlar ve sonuçlar paylaşılmış, uydunun yönelim belirleme sensörlerinden beklenen performans incelenmiştir. Bu kısımlarda sırasıyla verilen zaman dilimi için her mod için simule edilmiş açısal hız sensörünün x, y ve z eksenlerindeki ölçümleri, açılır manyetometre ve yedek manyetometre sensörünün maksimum ve ortalama hatası, kaba Güneş sensörlerinden ve hassas Güneş sensöründen hesaplanan Güneş vektörünün maksimum ve ortalama hatası, ufuk sensörünün maksimum ve ortalama hatası, yıldız izler sensörünün maksimum ve ortalama hatası paylaşılmıştır. Yönelim belirleme ve kontrol sistemi için kullanılan telekomut ve telemetriler paylaşılmıştır. Bu komutlarla birlikte yönelim belirleme ve kontrol mod tanımları kullanılarak operasyon fazları aşama aşama tanımlanmıştır. Bu fazlar sırasıyla, fırlatma ve erken operasyon fazı, güvenli mod fazı, Güneş'e yönelme fazı, iletme fazı, kamera fazı ve iXRD fazıdır. Bu modlar içinde yapılan yönelim belirleme ve kontrol operasyonlarıyla birlikte gönderilmesi gereken komutlar ve istenilen telemetriler aşama aşama açıklanmıştır.

Dördüncü kısımda yörüngede gerçekleştirilen operasyonlar detaylı olarak anlatılmıştır. Uydunun fırlatma tarihi olan 3 Ocak 2023'ten Mayıs 2024'ün sonuna kadarki dönemde karşılaşılan aksaklıklar tek tek kısaca açıklanmıştır. Bunların temel nedenleri durumdan duruma değişiklik göstermektedir. Bu nedenlere örnek olarak, uydu bilgisayarı kaynaklı sıkıntılar, yönelim belirleme ve kontrol sistemi bilgisayarı kaynaklı sıkıntılar, yer istasyonu iletişiminde görülen sıkıntılar, SharjahSat-1 yer istasyonu yazılımında yapılan hatalar, uydu yazılımında yapılan hatalar gösterilebilir. Bunların arasından operasyonları en çok etkileyenler uydu yazılımındaki hatalar ve yer istasyonu iletişimi sırasında karşılaşılan aksaklıklardır. Bu hatalar sonucunda yörünge operasyonlarının değişmesinden kaynaklı izlenilen yeni operasyon adımları bu bölümde tanımlanmış ve nedenleriyle açıklanmıştır. Planlanan bir kamera veya iXRD görevini tamamlamak için gereken 5 yer istasyonu geçiş planı açıklanmıştır. Bunlardan ilki uydu açısal hızlarını düşürmeye yönelik telekomut ve telemetrileri içermektedir. Tanımlanan ikinci ve üçüncü aşamalar, ikinci geçişte yapılmak için planlanmıştır. İkinci aşamada uydu yörünge parametreleri ve yönelim belirleme ve kontrol sistemi zamanı güncellenmektedir. Üçüncü aşamada yönelim belirleme ve kontrol sistemine yönelik belirli birkaç parametrenin güncellenmesi ve kaydedilmesine yönelik komutlar paylaşılmıştır. Dördüncü aşama kamera ya da iXRD görevleri sırasında gönderilen telekomutları içermektedir. Bu telekomutlar sırasıyla uydu genel telemetri kontrolü, açısal hız kontrolü, yönelim belirleme modu değişimleri, yönelim kontrol modu değişimleridir. Bunlarla birlikte ilgili görev yükünün çalıştırılmasına yönelik komutlar da gönderilmektedir. Son aşama operasyon tamamlandıktan sonra gerçekleştirilir ve toplanan telemetrilerle birlikte görev yükünün operasyonu sonucunda elde edilen veriler indirilmektedir. Bölümün devam eden kısmında tanımlanmış bu operasyon adımları izlenerek 3 farklı tarihte gerçekleştirilen görevlerden toplanan veriler sunulmuştur. Her durum için veriler ayrı ayrı incelenip yorumlanmış ve uydunun yönelim durumu çıkarılmaya çalışılmıştır. 11 Ocak 2024 tarihine ait veri grubu uydu hızlı-açısal hız düşürme yönelim kontrol modundayken x, y ve z eksenlerindeki açısal hız ölçümleri, kaba Güneş sensörü ve hassas Güneş sensörü ölçümleri sunulmuştur. 225 saniye boyunca toplanan açısal hız verilerinden yönelim kontrol modunun hızlı-açısal hız düşürme moduna değiştirilmesi sonucunda açısal hızların 48.1 °/s'den 41.8 °/s'ye düştüğü gözlemlenmiştir. Toplanan kaba Güneş sensörü ve hassas Güneş sensörü ölçümlerinin birbirleriyle uyumlu olduğu, ayrıca açısal hız sensör ölçümleriyle de uyumlu olduğu görülmüştür. 5 Şubat 2024 tarihine ait ver grubunda, açısal hız sensörü ölçümleri, açılır ve yedek manyetometre ölçümleri ve bunların kaba halleri, kaba ve hassas Güneş sensörü ölçümleri paylaşılmıştır. Bir önceki veri grubundan çıkarılan sonuçlara ek olarak, manyetometre sesnörlerinin kendi içinde tutarlı ölçüm verdiği gözlemlenmiştir. Ayrıca kalibre edilmemiş kaba manyetometre ölçümleri ile uydunun konumu için modellenmiş Dünya manyetik alanı değerleri karşılaştırıldığında, manyetometrenin kalibre edilmemiş durumda olduğu görülmektedir. 4 Mart 2024 tarihine ait veri grubunda açısal hız sensörü ölçümleri, kaba ve hassas Güneş sensörü ölçümleri ve ufuk sensörü ölçümleri paylaşılmıştır. Ufuk sensörü ölçümlerinden, bu sensörün hassas Güneş sensörüne kıyasla daha az veri topladığı görülmektedir. Bu çıkarımlardan sensörlerin birbirleriyle tutarlı olacak şekilde ölçüm yaptığı ve bazı sensörlerin diğerlerine kıyasla daha sık ölçüm yaptığı görülmüştür.

Beşinci kısımda proje kapsamında kullanılan TRIAD ve QUEST algoritmalarının modellenmiş sensör verilerinden alınan değerlerle performansına bakılmıştır. Öncelikle yerde modellenmiş yörünge ilerletici ve sensör modellerinden elde edilmiş yönelim belirleme sensörlerinden elde edilen sonuçlarla farklı sensör ve algoritma kombinasyonları karşılaştırılmıştır. Sonrasında bu algoritmalar SharjahSat-1'den toplanan sensör verileri girdi olarak kullanılarak çalıştırılmış ve sonuçları karşılaştırılmıştır.

Son olarak tezin sonuç kısmı ileride yapılabilecek çalışmalarda dikkat edilebilecek noktalara değinilerek sunulmuştur.

1. INTRODUCTION

This study is conducted in Space Systems Design and Testing Laboratory (SSDTL) of Istanbul Technical University (ITU) where undergraduate and graduate students work on the development of Cube Satellites (CubeSats). Up until now, SSDTL had developed 7 CubeSat projects which were designed and tested, and already launched into space.

1.1 Purpose of Thesis

One of the latest projects conducted in SSDTL is SharjahSat-1. It is a 3U+ CubeSat that is developed by Sharjah Academy for Astronomy, Space Sciences, and Technology (SAASST) of the University of Sharjah, SSDTL, and Sabancı University (SU). The project started development in 2019. The CubeSat is launched in Low Earth Orbit (LEO) in early 2023 and is still working. The primary payload of the CubeSat is the improved X-Ray Detector (iXRD) developed by the SU and the secondary payload is the dual camera system developed by SSDTL. The mission specific requirements from the payloads of the mission are presented in Table 1.1.

Table 1.1: Mission specific requirements [1] [2]

Payload	Requirement
iXRD	Detect hard X-rays from very bright galactic X-ray sources such as very bright black hole and neutron stars
	Observe and study the bright sun flares and development of solar coronal holes, responsible for driving the stellar wind at an early phase
	Contribute to the knowledge on miniaturized x-ray detectors for in space weather research
Dual Camera System	Acquire the images of regions on Earth from low orbit
	Take photo of SAASST and its surroundings

Attitude determination is one of the major issues for most of the satellite missions, and for this aspect, there are many different solutions in terms of sensor and estimation algorithm selection, which result in more accurate attitude determination for satellites. [3]

1.2 Literature Review

1.2.1 CubeSats

Small Satellites are one of the many classes of satellites that have lower costs and faster development processes than large satellites. The satellites which are those with a mass of under 500 kg, are defined to be small satellites. Within this category, sizes are classified into subclasses such as microsatellite, nanosatellite, picosatellite and femtosatellite. The satellite categories by their masses and approximate development costs are shown in Table 1.2. [4]

Table 1.2: Satellite categories by mass and approximate cost [4]

Category	Mass (kg)	Cost (USD)
Large Satellite	>1000	0.1-2 B
Medium Satellite	500-1000	50-100 M
Minisatellite	100-500	10-50 M
Microsatellite	10-100	2-10 M
Nanosatellite	1-10	0.2-2 M
Picosatellite	0.1-1	20-200 K
Femtosatellite	< 0.1	0.1-20 K

Even though small satellites are advantageous in terms of development costs, the system has mass, volume and power constraints, which effects the attitude determination accuracy by sensor performance and redundancy limitations. However, with the growing small satellite industry, these requirements are simplified and latest available technology sensors are integrated into the missions mostly because of CubeSats.

A CubeSat is a standardized cubic nanosatellite form factor that is ten centimetres on each side with a mass of approximately one kilogram. Larger CubeSats are multiples of this single CubeSat unit (U). For example, a 3U CubeSat is a common configuration that is approximately $10 \times 10 \times 30$ cm^3 and 3.3 kg. The standardization facilitates relatively frequent and low-cost access to space through launch as secondary payloads. Originally, CubeSat development has been started in academia, the rapid growth in CubeSat development has spread, and the CubeSats are currently being developed by universities, private industry, and both civil and defence-related government organizations. [5] Since, the CubeSat missions are focused on specific missions at lower costs, they are more preferred compared to the larger satellites. Thus, CubeSats has started to succeed especially in low-Earth orbit (LEO) missions. With that, they are currently developed even in the areas of astrophysics, heliophysics, and planetary sciences. [6] They have been used for payload tests and performance validations in the space environment for usage of future large-scale missions. Many CubeSats test new design methods, algorithms, and systems that would be considered risky for more expensive and more vital missions. But after demonstration on CubeSats, they can be used on larger systems.

Even though they are advantageous in described ways, they present some technical challenges due to power, mass and volume constraints. For example, the decreased surface area results in a low power generation, and the use of deployable solar panels add to development times, costs and risks. Also, these deployables may limit sensors and payloads on board. Additionally, in result of the volume and mass constraints, the close physical proximity of the various components leads to a high risk of electromagnetic interference on-board the satellite, such as the interaction of magnetometers used for attitude determination with nearby electronics. [7]

1.2.2 Attitude determination

Essentially ability to control the attitude of a satellite requires both actuator and sensor hardware at the same time. Together with the specific algorithms, sensors are used to measure the initial attitude state of the satellite while actuators change its current state into a desired one. Attitude determination combines the vector components of the mathematical models and sensor measurements in satellite and other related reference frames. By collecting and combining this information with several algorithms, attitude of the spacecraft is determined in terms of quaternions, rotation matrices and Euler angles.

The traditional types of sensors that can be used for attitude determination are sun sensors, star trackers, horizon sensors, magnetometers, and rate gyroscopes. [3] [8] The general information on performance, mass and power for each sensor is given in Table 1.3.

Table 1.3: Performance, mass and power information for attitude sensors [8]

Sensor	Typical Performance Range	Mass (kg)	Power (W)
Sun Sensor	Accuracy of 0.005 deg to 3 deg	0.1 to 2	0 to 3
Star Tracker	Accuracy of 0.0003 deg to 0.01 deg	2 to 5	1 to 20
Nadir Sensor	Accuracy of 0.1 deg to 0.25 deg	0.5 to 3.5	0.3 to 5
Magnetometer	Accuracy of 0.5 deg to 3 deg	0.3 to 1.2	<1
Rate Gyroscope	Drift rate of 0.003 deg/hr to 1 deg/hr	0.1 to 15	< 1 to 200

Sun Sensors provide a measurement of one or two angles between the sensor boresight direction and the sun, providing information about the line-of-sight vector to the sun in the satellite body-fixed frame. Analog coarse Sun sensors (CSS) give only one angle while digital fine Sun sensors (FSS) give two angles. [9]

Star trackers, also referred to as star cameras, are the most accurate type of attitude sensor. They are basically a digital camera with a focal plane populated by either charge-coupled device (CCD) or complementary metal-oxide semiconductor (CMOS) pixels (picture elements). A full attitude solution can be derived by comparing the star field image taken by the sensor to a star catalogue stored onboard. [9]

Nadir sensors, also known as horizon sensors, are infrared sensors that detect the contrast between cold of space and the heat of Earth's atmosphere. Through detection of the edges of the earth, the sensors measure Earth phase and chord angles to derive a measurement of the nadir direction in the body-fixed frame. [9]

Magnetometers measure the direction and magnitude of Earth's magnetic field. Given the decreasing strength of the geomagnetic field as distance from the Earth increases, they are generally used only at altitudes below 1000 km. [9]

Rate gyroscopes, also referred to simply as gyros, do not provide a measure of attitude, but are commonly used in spacecraft as they provide a measurement of angular velocity. They are combined with other directional or attitude measurements in recursive attitude estimators. [9]

Different algorithms give different results and accuracies while at the same time requiring different number and types of inputs, sensors and models. Information about some of the algorithms for 2 vector observations are shown in Table 1.4.

Table 1.4: Mission specific requirements [10]

Algorithm	Accuracy	Speed	Output Format
TRIAD	Low	Very High (120 flops)	Rotation Matrix
Q- Method	High	Low (>900 flops)	Quaternion
SVD	High	Low (<650 flops)	Rotation Matrix
QUEST	Low	High (<400 flops)	Quaternion
FOAM	Medium	High (<300 flops)	Quaternion
ESOQ/ESOQ 1	Low	High (<400 flops)	Quaternion
ESOQ 2	Low	High (<200 flops)	Quaternion

All these algorithms simply aim to solve Wahba's problem, which seeks to find a rotation matrix between two coordinate systems from a set of vector observations. Solutions are often used in satellite attitude determination utilising sensors. The cost function that Wahba's problem seeks to minimise is given in (1.1). [11]

$$Q(M) = \sum_{i=1}^{n} \|v_i^* - Mv_i\|^2 \tag{1.1}$$

Where v_i^* is the i-th 3-vector measurement in the reference frame, v_i is the corresponding i-th 3-vector measurement in the body frame and M is a 3 by 3 rotation matrix between coordinate frames. [11]

Implementation of Triaxial Attitude Determination (TRIAD) algorithm is simple but does not give an optimum solution. It consists on constructing two triads of orthonormal unit vectors using the vector information available. The algorithm assumes one of these vector measurements as more accurate compared to the other one. At the end of the operations, it will give an attitude matrix. [12]

Q-Method aims to solve Wahba's Problem by determining the rotational matrix as a quaternion. This algorithm also calculates the eigenvector which can be quickly done since only two vector observations are used. [10]

The single value decomposition (SVD) method consists of performing a single value decomposition on a matrix B and using the outputs of the unitary matrix U and V to calculate the optimal rotation matrix. However, it can be only used for analytical studies. [10]

The quaternion estimator (QUEST) method is one of the fastest algorithms and is also used for real time applications. However, it is less robust compared to Q-method. [10]

Fast Optimal Attitude Matrix (FOAM) algorithm computes its quantities without having to perform the SVD. [10] FOAM is the slowest of the four fast algorithms (QUEST, FOAM, ESOQ and ESOQ2), but also the most robust and reliable. [12]

Estimator of the optimal quaternion (ESOQ) method uses a priori attitude estimates of the attitude to perform a fast calculation of a quaternion. [10]

Second Estimator of the optimal quaternion (ESOQ2) works similar to the ESOQ method but also takes additional parameters into account. [10]

2. SHARJAHSAT-1 MISSION DESIGN

2.1 Mission Overview

SharjahSat-1 is a 3U+ CubeSat that is developed by SAASST, SSDTL and SU. Main payload, iXRD, is developed by SU, while satellite bus and dual camera system payload is developed by SSDTL. SSDTL is also responsible for mission design, and development of the CubeSat. Besides from 2 payloads, the CubeSat houses EPS, communication system, on-board computer (OBC), ADCS, and an interface board, which are represented in Figure 2.1.

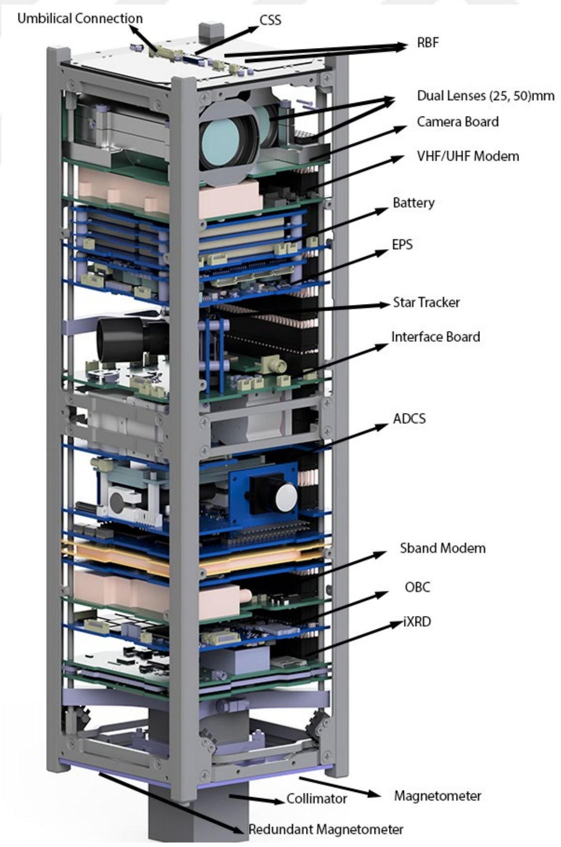

Figure 2.1 : SharjahSat-1

2.2 System Block Diagram

System block diagram of the SharjahSat-1 with power and data busses is represented in Figure 2.2. The subsystems will be described in detail in following subsections.

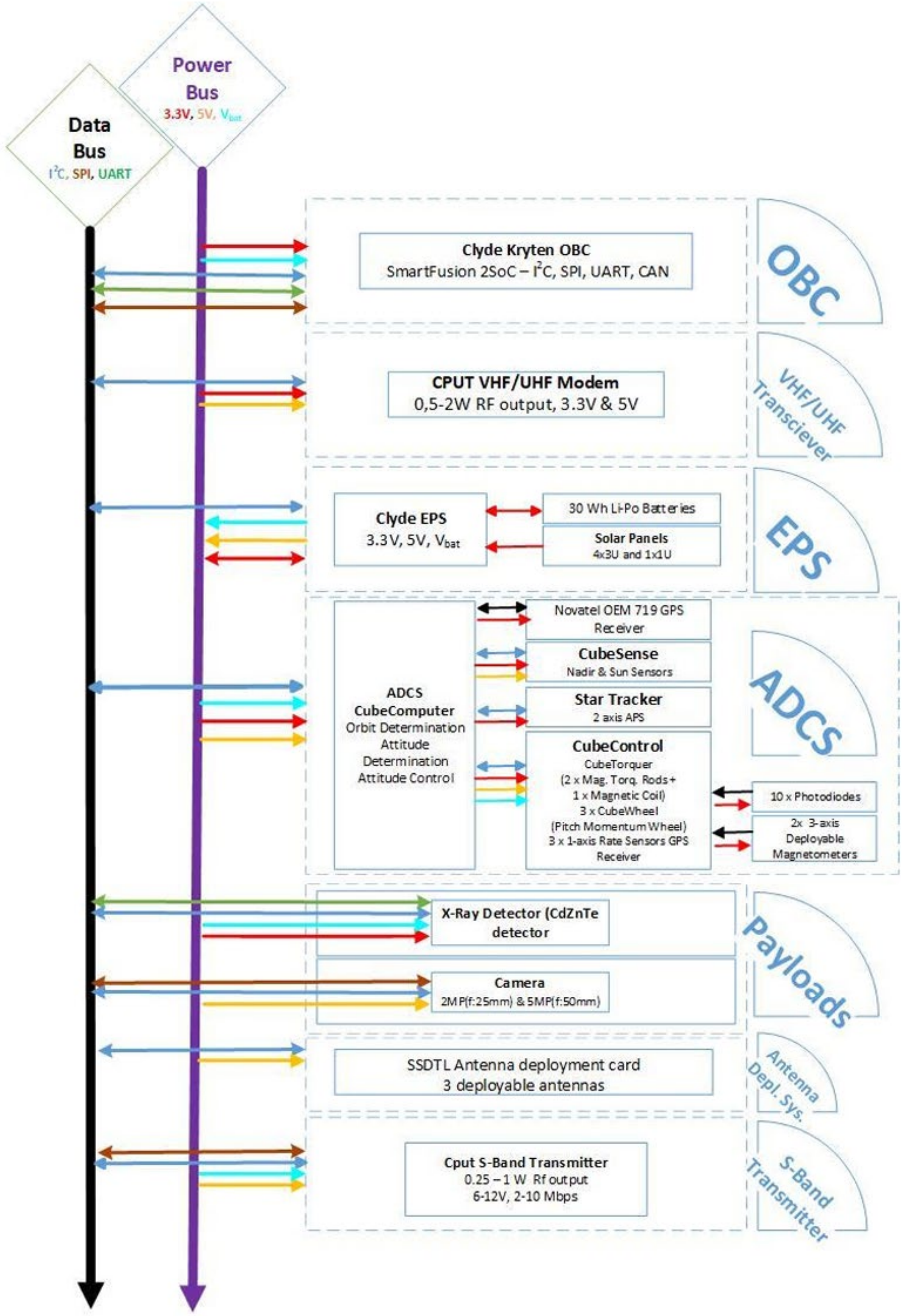

Figure 2.2 : System block diagram of SharjahSat-1

2.3 Subsystems

2.3.1 Main payload

iXRD is the main payload of SharjahSat-1, which can carry out science missions such as observation of bright galactic X-ray sources and solar flares.

The design of the iXRD stems from the XRD on BeEagleSat, a 2U CubeSat launched on May 26, 2017 and de-orbited in April 2019. Compared to the XRD, three important improvements are part of the design of the iXRD:

- a Tungsten collimator to limit the field of view,
- a larger and thicker CdZnTe crystal to increase the collecting area and efficiency,
- an improved electronics design to reduce the electronic noise.

Using a collimator opened up two important main science objectives:

- Detect hard X-rays from very bright galactic X-ray sources such as very bright black hole and neutron stars to study state transitions
- Observe and study the hard X-ray spectrum of the bright sun flares and development of solar coronal holes, responsible for driving the stellar wind at an early phase

In addition, it can contribute to the studying cosmic X-ray background in small fields, catching very bright gamma-ray bursts and soft gamma-ray repeater bursts, testing an electrical discharge machining manufactured Tungsten collimator, evaluating a software that determines particle rates in a detector volume in a given orbit [13].

For the main objective, the brightest hard X-ray sources that can be followed for long times have been determined and provided in Table 2.1 [14]

Table 2.1: Bright x-ray sources to be followed [14]

Source	RA (°)	DEC (°)	Mean cts	Max cts	Expected iXRD rate
Crab	83.633	22.015	1000	1762	1.0 – 2 cts/s
Sco X-1	244.979	-15.640	1143	3380	1.0 – 4 cts/s
Cyg X-1	299.591	35.202	220	1734	0.3 – 2 cts/s
Vela X-1	135.529	-40.555	119	2614	0.1 – 3 cts/s
GRS 1915+105	288.798	10.946	153	692	0.1 – 1 cts/s

A stable pointing shall be maintained for at least 600 s in one observation for the visible cosmic source chosen in each observation. This is required to provide a signal to noise ratio to produce a daily spectrum of observed sources. In order to obtain a good signal to noise, collimator loss should be minimized. An error of 1 degree in pointing means 25% loss, whereas 2 degrees means 50% loss. Thus, pointing knowledge shall be better than 1 degree [13].

For the second objective, the instrument will be pointed towards the Sun. Only very bright solar flares can be detected with a small detector. In the meantime, when the spacecraft is not pointing at bright sources or the Sun, cosmic X-ray background observations will be conducted to obtain a better estimate of the background.

Scheduling of the iXRD operation is critical for the mission performance. Depending on the orbit, and time of the year, a decision must be made to try to observe the point sources chosen. The performance of the detector is affected by the position of the Sun, Moon, and the Earth with respect to the position of the source.

2.3.2 Secondary payload

Second payload of the SharjahSat-1 is an Electro-Optic Camera Subsystem. The CubeSat has a dual-camera system that utilizes two different focal lengths of 50mm and 25mm to achieve a ground sampling distance (GSD) of 50m/pixel or better. The system utilizes dual sensors and lenses: OV5642 and OV2640; Fujinon CF50ZA-1S, and Fujinon HF25XA 1S, specifications are presented in Table 2.2 and Table 2.3.

Table 2.2: Sensor specifications [15] [16]

Sensor	Size	Resolution	Pixel Size	Sensitivity	Interface
OV5642	1/4"	2592 x 1944	1.4 µm x 1.4 µm	600 mV/Lux-sec	SPI
OV2640	1/4"	1600 x 1200	2.2 µm x 2.2 µm	600 mV/Lux-sec	SPI

Table 2.3: Lens specifications [15] [16]

Lens	Focal Length (mm)	Aperture (F-Stop)	Lens Length (mm)	Diameter (mm)	Mass (g)
CF50ZA-1S	50 mm	2.4	68 mm	39 mm	155
HF25HX-1S	25 mm	1.6	29.5 mm	46.5 mm	72

2.3.3 Structure and mechanisms

SharjahSat-1's external dimensions are in accordance of 3U+ CubeSat size defined specifications [17]. The iXRD system needs a collimator, and a shield made from tungsten to have adequate performance. Thus, the collimator was forced out of the satellite structure due to the limited volume, which corresponds to 3U+ size.

Internally the CubeSat consists of 2 stacks that are connected via a continuous PC104 bus as presented in Figure 2.3. Structure is responsible for providing a strong platform to hold everything together, while also allowing a free assembly, and enough cavities to route necessary cabling. SharjahSat-1 consists of 2 stacks. Structure itself consists of structure holders, ribs, M3 threaded spacers, rods and necessary spacers and washers for placing other subsystems.

Figure 2.3 : Stacks of SharjahSat-1

ADCS actuators were placed near the centre of mass (CoM) as much as possible. Also, the star tracker of ADCS is connected to satellite structure rods via special holder which also locks the Star Tracker in optimum angle. A stray light blocking hood is also placed on the solar panel where star tracker is aimed out from. Hood is shaped to not collide with field of view (FoV) of Star Tracker.

2.3.4 On-board command and data handling system

The Clyde Space CubeSat OBC is used as the main house-keeping computer for the mission. It is designed as a highly reliable, robust and capable mission control computer. It also offers a wide variety of communications interfaces and peripheral functions. Some of its features are:

- Microsemi SmartFusion 2 Heterogeneous SoC including ARM Cortex-M3 processor @ 50 MHz delivering 62.5 DMIPS
- Integrated cache and Memory Protection Unit (MPU)
- 8 MiB Magnetoresistive RAM (MRAM) and 256 KiB eNVM for code storage and execution 98
- 4 GiB flash memory for bulk data storage, this will be used for saving telemetry logs and storing images from camera and XRD payload.
- Autonomous single event latch-up protection
- EDAC protected memories and FIFOs, this mechanism provides protection against data modifications and errors in the address decode logic.
- JTAG interface for programming and debugging
- Hardware cryptographic accelerator
- Hardware CCSDS accelerator
- Real Time Counter with 40 minutes of backup power
- Operating temperature range: -40°C to 80°C
- 30 GPIO, all GPIOs are controlled by a custom interface (PINMUX) on the programmable logic. By using this interface, GPIOs can be set as an input and output or to their defined alternate functions.
- 1x SPI (7x chip selects), 1x QSPI (7x chip selects), 2x I2C, 1x CAN, 8x LVTTL UART, 1x debug UART, 2x RS485 (Configurable as 1x RS422)
- 1x QSPI over LVDS, 1x SPI over LVDS
- Axis Magnetometer & Angular rate sensors
- 1x DTMF
- 1x MicroSD interface

2.3.5 Communication system

SharjahSat-1 have 2 different communication systems. One very high frequency (VHF) - ultra high frequency (UHF) transceiver and one S-Band transmitter.

VHF-UHF RF Modem provides communication between ground station (GS) and satellites OBC. In this context modem processes and transmits digital data, such as health status of the subsystems and attitude information of the satellite with all raw parameters from the ADCS unit, received from OBC to GS and receives commands from GS and transfers these commands to OBC. For the SharjahSat-1 CPUT UHF/VHF modem will be used. It supports both Gaussian Minimum Shift Keying (GMSK) modulation at 9600bps for downlink and Audio Frequency-Shift Keying (AFSK) modulation 1200bps for uplink. Modem operating frequencies are selected as 145.825 MHz for uplink and is 437.325 MHz for downlink. The transceiver operates in full-duplex mode. Moreover, if needed, transceiver can operate as beacon, too. Output power of transmitter is selectable between the values 27, 30, 33 dBm. For the SharjahSat-1 30dBm (1 watt) configuration is selected as default.

System diagram of CPUT modem is represented in Figure 2.4.

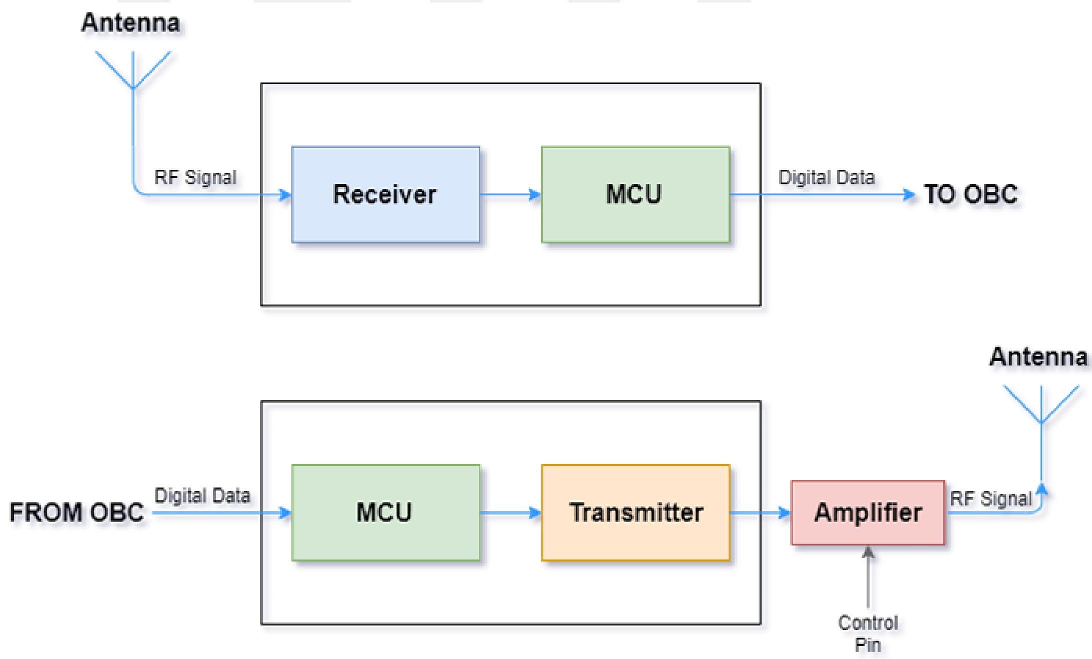

Figure 2.4 : System block diagram of the CPUT modem

S-Band modem in SharjahSat-1 will be used only to provide downlink communication between satellite and GS. Payload data, such as camera images and/or iXRD measurements, will be downloaded by using S-Band transmitter. In SharjahSat-1 CPUT S-Band Transmitter is used. It supports data rates of up to 2 Mbps (1 Mbps user data + 1 Mbps encoding). The transmitter’s frequency of operation is selectable from 2.4-2.45GHz. The transmitter implements offset quadrature phase-shift keying (OQPSK) or quadrature phase shift keying (QPSK) modulation with Intelsat IESS-308 based encoding. Output power is adjustable in 2dB steps from 24 dBm to 30 dBm. It has 4 configurable data transfer rates as 1 2, 1 4, 1 8. The transmitter is configured via an I2C data bus and high-speed payload data is sent via SPI.

In SharjahSat-1 S-band modem will be operated at 2405MHz with 30dBm (1 watt) of output power. For the modulation method (Downlink only) QPSK will be used. The default synchronization word 0x1ACFFC1D, a CCSDS 32bit Attached Sync Marker (ASM), will be used. All these parameters are configurable via I2C communication.

System block diagram of the S-Band transmitter is represented in Figure 2.5.

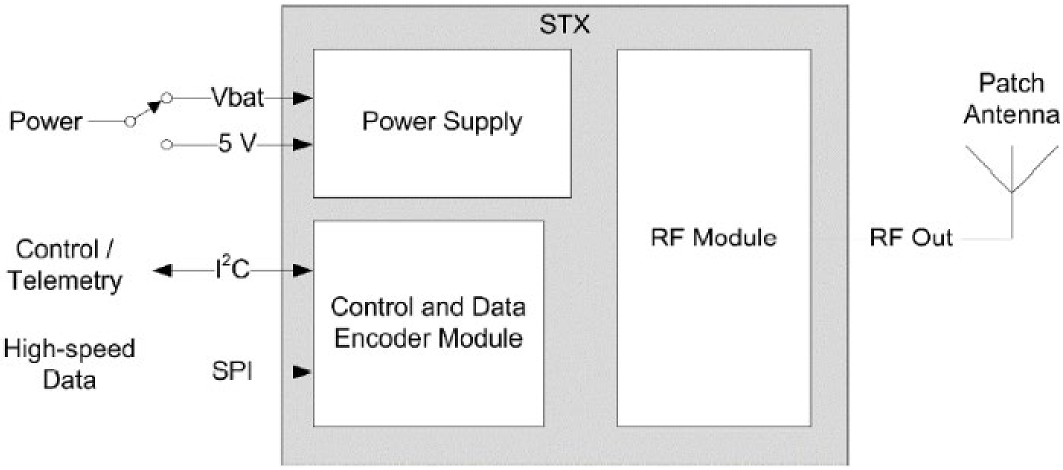

Figure 2.5 : System block diagram of S-Band transmitter

2.3.6 Electrical power system (EPS)

EPS, in general, produces required supply voltages from battery voltage for other systems.

- Converting solar energy to electrical energy with maximum efficiency.
- Maximizing power harvested from solar arrays.
- Controlling charge and de-charge for efficiency and maximum lifetime.
- Regulating harvested or stored energy to supply other spacecraft systems.
- Short-circuit and over-voltage protection.
- Hard-resetting spacecraft power busses if necessary.
- Measuring and calculating battery parameters like state of charge, temperature, current and voltage and reporting these parameters to spacecraft computer.

EPS of SharjahSat-1 consists of 3 sub-elements;

- Electrical Power Management Unit (Power management and distribution unit): EPS management unit is the most critical part of the any satellite system. This subsystem controls and overviews all electrical operations of the satellite. This includes managing battery charging, power distribution and protection of power busses.
- Solar Arrays: SharjahSart-1 employs solar panels to meet electrical power requirements of its subsystems. Solar panels are mounted on its side panels and there will be no deployable panels. Dimensions of the solar panel is 70x40 millimetres. There are a total of 25 solar panels within SharjahSat-1 structure. The number of solar cells for spaceflight is calculated through power budget analysis. They are positioned on the panels as uniformly as possible. Due to the design limitations, the closest distance between two solar cells must be greater than or equal to 1 millimetre.
- Battery Pack: During the orbital operations, harvested solar energy is used by subsystems, and excessive solar energy is stored in the battery. While satellite is in eclipse if there is a power requirement, this required power will be delivered from stored energy in batteries. As it has determined in power budget section, to comply with power budget requirements that from the bower budget calculations, it has been determined that, SharjahSat-1 must include a battery pack with at least 20 W-hr energy capacity. With little extra capacity, Clyde Space 3rd Generation 30 W-hr battery pack was selected to be used in SharjahSat-1. Clyde Space 3rd Generation Battery uses I2C (Inter-Integrated Circuit) interface in slave configuration to communicate with the both EPS and OBC. In default configuration, battery pack uses 0x2A slave address with the 100kHz I2C bus speed at +3.3V level.

Figure 2.6 shows EPS architecture.

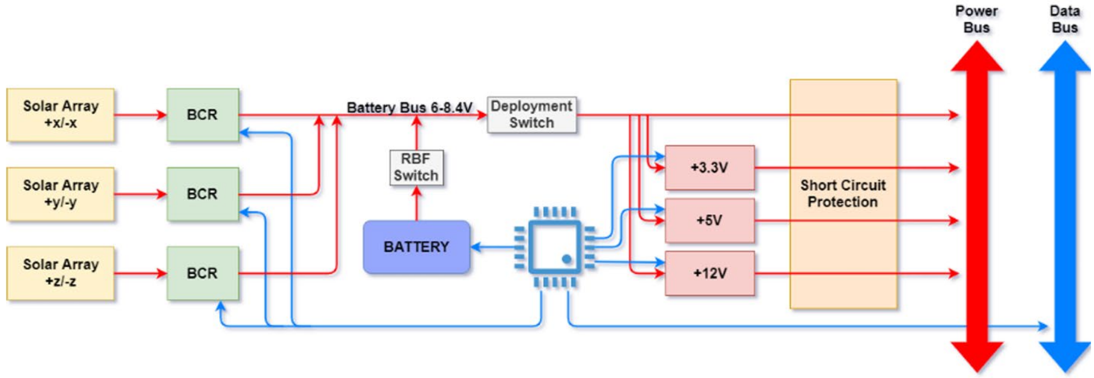

Figure 2.6 : EPS architecture

2.3.7 Attitude determination and control system (ADCS)

The success of the SharjahSat-1's mission depends on the ADCS since payloads of the satellite require accurate pointing and tracking. ADCS is responsible for the quality of the data from the payloads, in addition to right pointing for S-band communications, thermal management, and power. ADCS system is responsible for the pointing of the payloads of the SharjahSat-1, cameras require to be pointed at the desired location for a required amount of time and the iXRD requires to be pointed at the object of interest for at least 600 sec. To provide those, ADCS system was selected to be fully-fledged including 3 reaction wheels, Magnetorquers for three axes, Sun Sensor, Nadir Sensor, Coarse Sun sensors (CSS), Rate sensor, Star Tracker, and a global positioning system (GPS) for time and location information. The specifications of ADCS components are listed in the Table 2.4.

Table 2.4: Specifications of ADCS components

Sensors and Actuators	Type	Range/ FoV	Accuracy (RMS)
Magnetometer	3-axis MagR	±60 µT	< 40 nT
Sun Sensor	2-axis CMOS	Hemisphere	< 0.2°
Nadir Sensor	2-axis CMOS	±45°	< 0.2°
CSS	Photodiodes	Full Sphere	<10°
Rate Sensor	3-axis MEMS	±20°/sec	<0.01°/sec
Star Tracker	2-axis APS	52° x 27°	<0.01° boresight <0.03° rotate
CubeWheel Small	BLDC Motor	±1.7 mNms	<0.0004 mNms <0.001 mNms
Magnetorquer Rod	3-axis Ferro-magnetic coils	±0.24 Am^2	<0.0012 Am^2

CubeADCS from CubeSpace is selected as the ADCS module for the SharjahSat-1. It consists of modules that can be configured for the requirements.

SharjahSat-1 ADCS bundle includes:

- CubeControl: is sensor and actuator interface module
- CubeSense: is an integrated Sun and nadir sensor for the attitude sensing.
- CubeStar: is a compact star tracker.
- CubeComputer: Computer that is used to control ADCS

2.4 Orbit Analyses

Sun-synchronous orbits (SSO) are obtained achieved by matching the angular rotation of Earth around the sun with the nodal regression caused by the J2 (oblateness of Earth). Consequently, the angle between the Earth-Sun vector and the orbital plane remains constant as represented in Figure 2.7. [18]

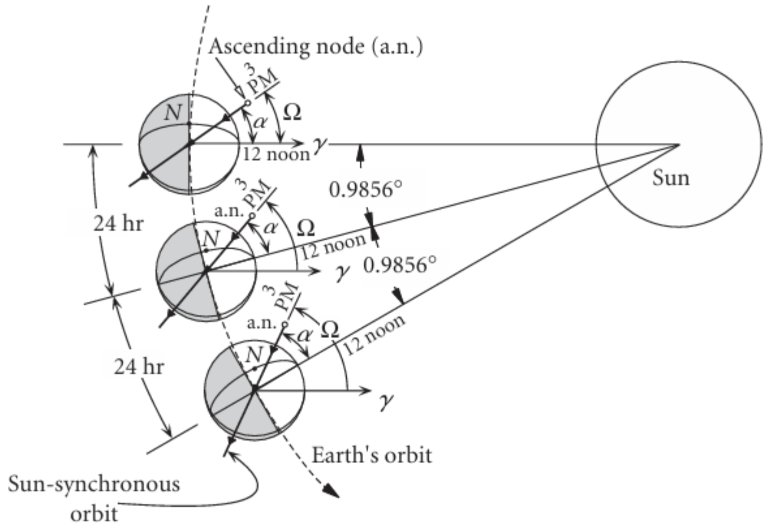

Figure 2.7 : Sun-synchronous orbit [18]

This orbit type was adapted in SharjahSat-1 mission because it is the most optimal for Earth observation due to constant Sun Angle. Thus, the satellite will pass through SAAST at the same local time every time.

2.4.1 Lifetime analysis

Guidelines issued by “Inter-Agency Space Debris Coordination Committee” in 2007 require space objects in LEO to have a maximum lifetime of 25 years after launched into space. In order to comply with this guideline an altitude of 550 km was chosen for SharjahSat-1.

The launch service covers direct insertion to orbit via commercial launch vehicles. Average altitude is 550 km, average period is 95 minutes and orbital velocity is around 7.6 km/s. A lifetime analysis has been performed with the orbital parameters shown in Table 2.5. By using the presented parameters, a lifetime analysis is conducted by using high precision orbit propagator (HPOP). At the end of the analysis, it is concluded that after 13.91 years, SharjahSat-1 will burn in the atmosphere.

Table 2.5: SharjahSat-1 configuration and orbital parameters

Parameter	Value
Launch Date	Fourth Quarter of 2022
Mass	4.107 kg
Drag Area	0.012 m^2
Area Exposed to Sun	0.02 m^2
C_D	2.2
C_R	1
Drag Area/Mass	0.0029218
Area Exposed to Sun/Mass	0.0048697

Since there is no propulsion system present on SharjahSat-1, it will lose altitude throughout the orbit lifetime, and will start to burn upon reaching around 200 and 160 km altitude. Orbital lifetime depends on satellite ballistic coefficient, i.e., the surface area and therefore the drag it experiences in the atmosphere, and the solar radiation pressure. The solar cycle is in its minimum as of 2021, and is expected to peak in 2025 [19]. Therefore, the satellite will start to significantly lose altitude in a few years after launch. The altitude for the SharjahSat-1 over years is presented in Figure 2.8.

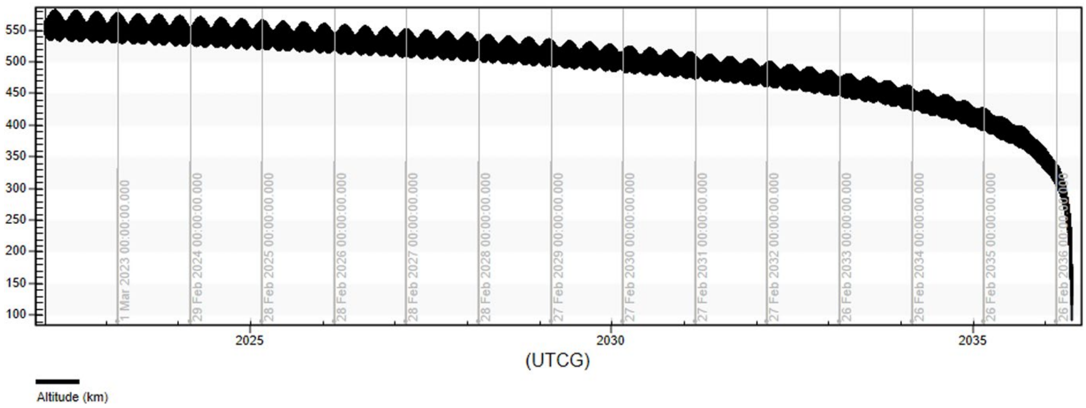

Figure 2.8: Altitude of SharjahSat-1 over years

2.4.2 Power generation analysis

Power generation is done by 25 solar cells which are placed on 5 sides of the SharjahSat-1. The solar cell placement for SharjahSat-1 is shown in Figure 2.9.

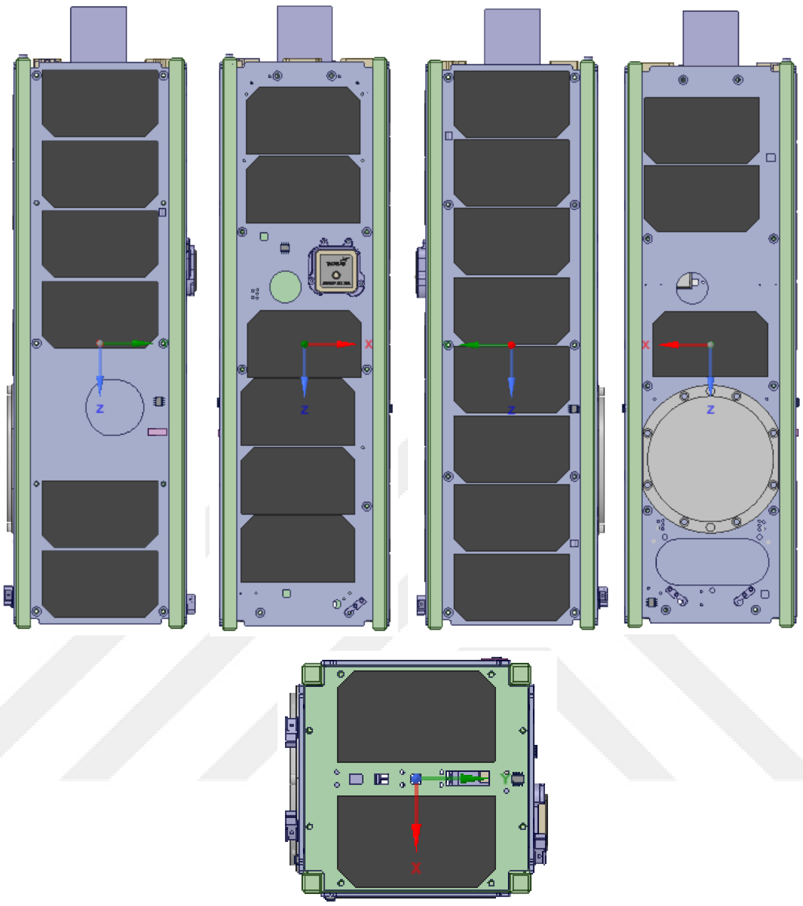

Figure 2.9: Solar Cell Placement

The orbit is Sun-Synchronous with an altitude range of 550 kilometres. Local time on descending node (LTDN) is designated 10:30:00.000 HMS. Also, sun pointing, nadir pointing and spinning of satellite are considered. For the sun pointing cases, attitude type of sun alignment with nadir constraint is chosen with 0º alignment offset, so 8-cell panel of SharjahSat-1 is always facing the sun. In the cases of the nadir pointing, attitude type of aligned and constrained is chosen with aligned vector of (0, -1, 0) and constrained vector of (0, 0, 1) in Cartesian coordinate system. Therefore, the S-band antenna always facing to the centre of the Earth. Also, the time step for the analysis is taken as 1 second. Orbital parameters used in the analysis is shown in Table 2.6.

Table 2.6: SharjahSat-1 orbital parameters for power generation analysis

Parameter	Value
Analysis Start Time	June 1st, 2022
Inclination (º)	97.0346
Altitude (km)	550
LTDN	10:30:00.000
Attitude Control Modes	Sun Pointing
	Nadir Pointing
	Spinning

Obtained results from power generation analysis are represented in Table 2.7. Based on the results, the sun pointing results in more power generation compared to nadir pointing and spinning. Also, nadir pointing is more beneficial compared to spinning in terms of power generation. On the other hand, the highest peak power generation is seen during the spinning.

Table 2.7: SharjahSat-1 orbital parameters for power generation analysis

Attitude Control	Average Generated Power per Orbit (W)
Sun Pointing	5.070359
Nadir Pointing	3.849168
Spinning	3.704066

2.4.3 Star access analysis

The primary mission of the SharjahSat-1 is to collect data from the five selected x-ray resources by using iXRD. Since SharjahSat-1 will be deployed into a sun synchronous LEO, the x-ray readings of iXRD will be affected by high radiation zones and iXRD should perform readings in the outside of these zones. Therefore, the possible time intervals for iXRD operation are investigated.

The RA and DEC values for the five stars are needed in order to determine the positions of the X-Ray sources, which are Crab, Sco X-1, Cyg X-1, Vela X-1, and GRS 1915+105. The corresponding values of the stars are given in Table 2.1. Additionally, some of the parameters for the analysis is assumed as given in Table 2.8.

Table 2.8: Parameters for the analysis

Parameter	Value
Analysis Time Interval	June 1st, 2022 – June 1st, 2023
Orbit Type	SSO
Altitude (km)	550
LTDN	10:30:00.000
Pointing	Targeted
Solar Exclusion Angle	6 degrees
Lunar Exclusion Angle	5 degrees
Orbit Propagator	HPOP

Representation of the SharjahSat-1 during the iXRD operation is shown in Figure 2.10.

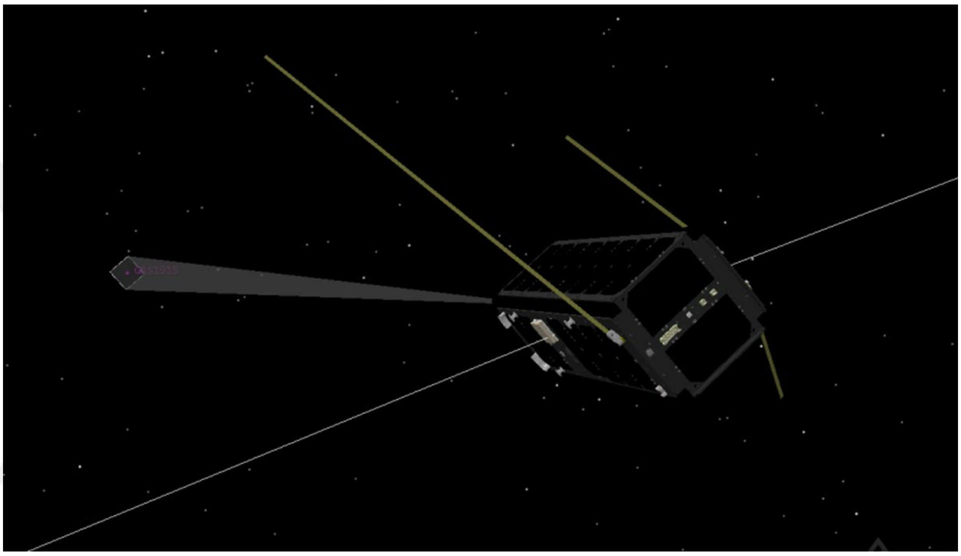

Figure 2.10: Representation of SharjahSat-1 during an iXRD operation

Additionally, some constraints are added into analysis. Since, after the Earth, the Sun and the Moon are closest celestial bodies, which can disrupt the access to the sources, a solar exclusion angle of 6 degrees and a lunar exclusion angle of 5 degrees are selected. Also, the iXRD should not operate at some regions due the increase in the measurement noise. These regions are located around geographic poles and South Atlantic Anomaly (SAA). Since the region in SAA is amorphous, it is divided into smaller regions shown in Figure 2.11.

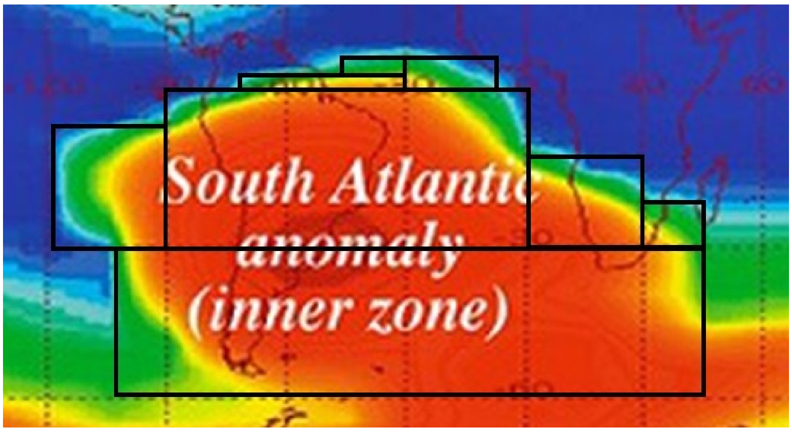

Figure 2.11: Divided regions for the SAA

The minimum and maximum longitudes and latitudes for all the exclusion zones are given in Table 2.9.

Table 2.9: Minimum and maximum latitude and longitude of the exclusion zones

Zone Number	Minimum Latitude (º)	Maximum Latitude (º)	Minimum Longitude (º)	Maximum Longitude (º)
1	60	90	-180	180
2	-90	-60	-180	180
3	-60	-30	-105	45
4	-30	0	-90	0
5	-30	-10	-120	-90
6	-30	-12.5	0	30
7	-30	-20	30	45
8	0	9	-30	-6
9	3	9	-15	0
10	0	3	-42	0

At the end of the analysis, durations of the source targeted pointing are obtained for the time interval. Each selected source can be accessed during the time interval. The number of access and average access duration for each source is given in Table 2.10 and Figure 2.12. All of the average access times exceed the minimum required access time of 600 seconds. Also, SharjahSat-1 has continuous access to the Crab, Sco X-1 and GRS 1915+105 in various times of the year. Crab has full access from 18th September to 14th October, full access from 15th October to 25th October. GRS 1915+105: Full access from 18th October to 14th November, full access from 8th April to 22nd May. Sco x-1: Full access from 27th August to 10th October, full access in September.

Table 2.10: Results from the access analysis

Average Access Time per Orbit for each Month (minutes)	Source Name				
	Crab	Sco X-1	Vela X-1	GRS 1915+105	Cyg X-1
June 2022	33.05	60.21	69.24	67.78	67.83
July 2022	59.71	62.06	63.53	60.97	61.78
August 2022	63.53	72.42	60.53	60.44	60.05
September 2022	72.75	-	60.08	64.58	60.94
October 2022	80.98	73.66	61.54	77.19	63.81
November 2022	67.27	55.48	63.62	77.77	65.54
December 2022	60.34	59.87	63.17	64.62	62.74
January 2023	59.37	61.23	60.81	60.05	60.07
February 2023	60.89	68.15	59.58	60.23	59.67
March 2023	67.86	82.60	60.15	65.82	61.84
April 2023	70.44	68.93	63.35	80.30	68.86
May 2023	62.74	60.91	68.73	78.74	74.62

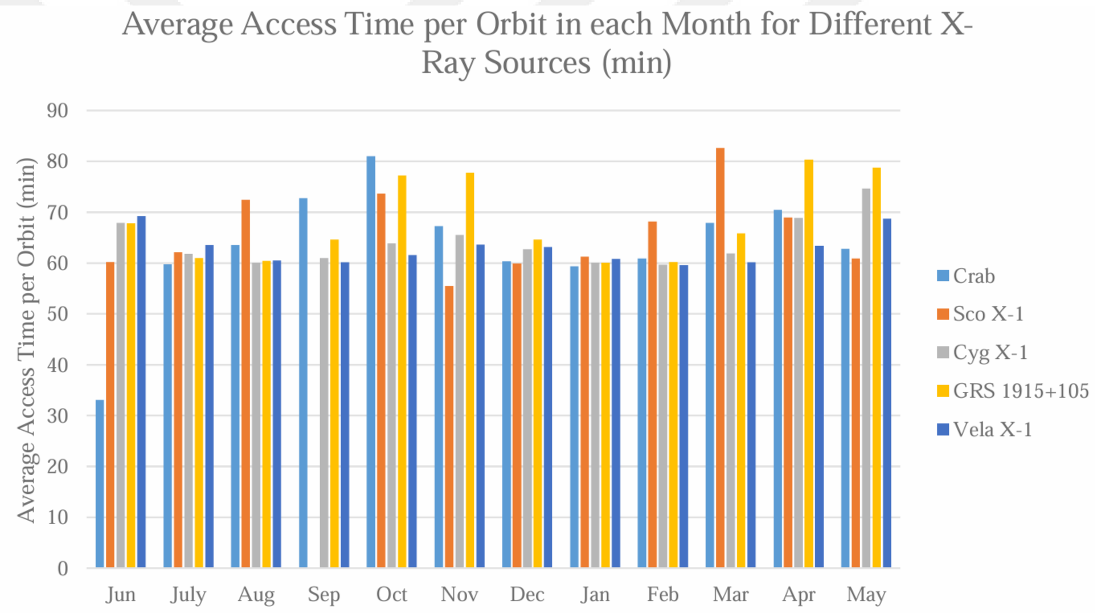

Figure 2.12: Graph showing monthly access times to various stars

2.4.4 Camera access analysis

The secondary mission of the SharjahSat-1 is to take photo of the Sharjah Academy of Astronomy, Space sciences & Technology (SAASST) by using two cameras on board. The parameters for the analysis are given in Table 2.11.

Table 2.11: Parameters for the analysis

Parameter	Value
Analysis Time Interval	June 1st, 2022 – June 1st, 2023
Orbit Type	SSO
Altitude (km)	550
LTDN	10:30:00.000
Pointing	Targeted
Orbit Propagator	HPOP

For the 5 MP camera (50 mm lens), the horizontal and vertical field of view (FoV) angles are 4.208 degrees 3.237 degrees. For the 2 MP camera (25 mm lens), the horizontal and vertical FoV angles are 8.274 degrees and 6.145 degrees. During the analysis process, it was assumed that with active control, the cameras could be tilted 30° to either side. Representation of SharjahSat-1 tracking SAASST is shown in Figure 2.13.

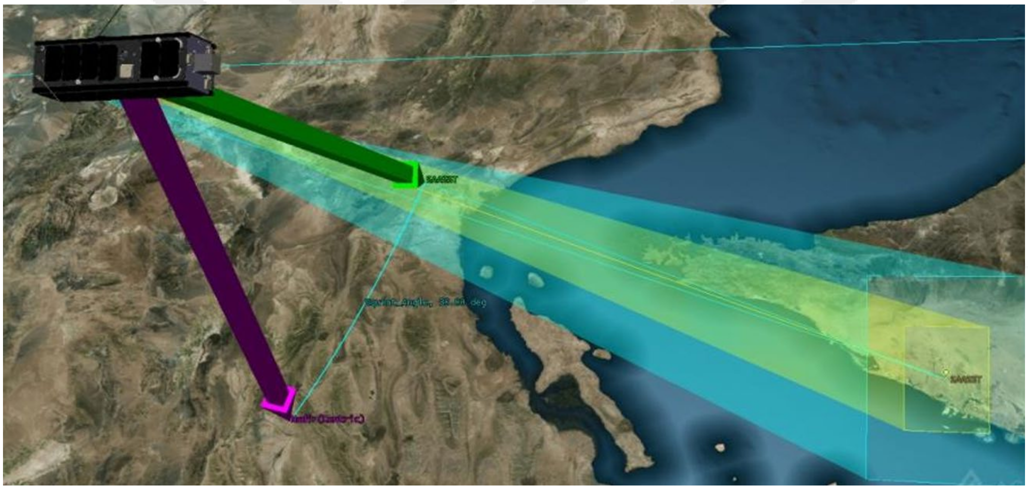

Figure 2.13: Representation of SharjahSat-1 tracking SAASST

The results of the camera access analysis are presented in Table 2.12.

Table 2.12: Camera access analysis results

No pointing capability				
Target	**Average Weekly Pass Count**	**Average Annual Pass Count**	**Average Pass Duration (s)**	**Max Duration Without Access**
SAASST	0.5	26	7.914	17 days
ITU	0.6	30	8.165	21 days
30 degrees tilting capability				
Target	**Average Weekly Pass Count**	**Average Annual Pass Count**	**Average Pass Duration (s)**	**Max Duration Without Access**
SAASST	3.9	201	72.560	11 days
ITU	4.6	243	79.984	14 days

2.5 System Budgets

In order to conclude the subsystem requirements for the SharjahSat-1 mission, several system budgets are conducted and represented.

2.5.1 Mass budget

The simplified mass budget of SharjahSat-1 is given in Table 2.13.

Table 2.13: SharjahSat-1 mass budget

Component	**Mass (gram)**
Structures and Mechanisms	441.67
Camera System	663.77
Interface Card	57.84
Battery	278.79
EPS	179.10
UHF/VHF Modem	128.23
S Band Modem	117.33
OBC	69.57
iXRD	941.93
ADCS	554.64
Busses	76.60
Solar Panels	464.64
Total	3974.00

2.5.2 Power budget

SharjahSat-1 has 3 main operation modes: normal, no payload and safe. Power budget is calculated for these three different cases. As long as the satellite is in normal mode, camera and iXRD operations are performed. It means that the SharjahSat-1 is fully operational, and power levels and attitude control are as desired. If something goes wrong with the ADCS then satellite operates in safe mode. Results from power budget are represented in Table 2.14. The results indicates that, SharjatSat-1 panel system can generate enough power with a safe margin to operate itself based on the mission requirements. SharjahSat-1 will consume about 2853,1 milliwatt in normal operation. Clyde EPS 25-02452 has 3 BCRs. For side panels the BCR efficiency is %90 typical. For 1U panels it is %80. That's why an 80% efficiency is used for produced power as a safe value. For safe mode, there is a %253,9 safety margin. If necessary, this mode can be used to generate more power in a power fail situation.

Table 2.14: SharjahSat-1 power budget

	Normal Mode	**Safe Mode**	**No-Payload Mode**
Total Power Consumption (mW)	2853.1	1125.1	2535.1
Produced Power During Orbit (mW)	3192.0	3982.4	3332.8
Margin (%)	11.9	253.9	31.5

2.5.3 Data budget

To find the data size required to download to the ground station, total data produced by the payloads were calculated. It is required to find how many images or how many iXRD packets can be downloaded during a given time. It is assumed that SharjahSat-1 will take 5 jpeg compressed images with both cameras (2MP and 5MP) in a week, and perform daily X-Ray observations. Total data size may change during the operations based on the power budget and coverage time for considered ground stations. With an additional ±15° pointing capability, the S-Band has on average 1100 seconds of access to the SAASST GS in a week. While the S-Band has a transmission rate of 1 Mbps (128 kb/s), the GS has a minimum receive rate of 128 kbps which restricts the communication rate; thus, the minimum rate was used in calculations. Consequently, a total of 17.19 MB of data can be downloaded per week using the S-Band transmitter. Table 2.15 and Table 2.16 presents how much payload data can be generated and downloaded based on these assumptions.

Table 2.15: SharjahSat-1 data budget per week (128 kbps)

Data	Data size with packaging (MB)	#	Total data (MB)/week	Time to download (s)	In Mins	Per one set (sec)
5 MP JPEG	0.7	5	3.5	219	3.65	44.3
2 MP JPEG	0.25	5	1.25	78	1.30	15.6
Subtotal	-	-	4.75	297	3.95	-
iXRD Data	0.285	7	2	128	2.13	18.3
Total	-	-	6.75	325	6.08	-

Table 2.16: SharjahSat-1 data budget per week (1 Mbps)

Data	Data size with packaging (MB)	#	Total data (MB)/week	Time to download (s)	In Mins	Per one set (sec)
5 MP Raw	5	2	10	80	1.33	40
5 MP JPEG	0.7	5	3.5	28	0.47	5.6
2 MP Raw	2	2	4	32	0.53	16
2 MP JPEG	0.25	5	1.25	10	0.17	2
Subtotal	-	-	18.75	150	2.5	-
iXRD Data	0.285	7	2	16	0.27	0.038
Total	-	-	20.75	166	2.77	-

2.5.4 Link budget

Link budget represents transceiver systems RF power redundancy to the losses. Losses includes, but not limited to, transmission line losses, antenna pointing losses, antenna polarization losses, path loss, atmospheric loss, ionospheric losses etc. In this section link budgets are presented for VHF/UHF modem and S-Band Transmitter. For VHF/UHF modem both downlink and uplink budgets calculated. For S-Band Transmitter only downlink budget is required.

Link parameters and link margins of VHF and UHF communication between SharjahSat-1 and ground station for uplink and downlink are presented in Table 2.17. System link margin for downlink is calculated as 7.8 dB and the system link margin for the uplink is calculated as 34.6 dB.

Table 2.17: Downlink and uplink link budget for VHF and UHF communication

DOWNLINK		UPLINK	
Parameter	**Value**	**Parameter**	**Value**
Spacecraft		***Ground Station***	
Spacecraft Transmitter Power Output	1.0 watts -10.0 dBW 20.0 dBm	Ground Station Transmitter Power Output	100.0 watts 20.0 dBW 50.0 dBm
Spacecraft Total Transmission Line Losses	0.5 dB	Ground Station Total Transmission Line Losses	3.4 dB
Spacecraft Antenna Gain	2.2 dBi	Antenna Gain	14.4 dBi
Spacecraft EIRP	-8.4 dBW	Ground Station EIRP	31.0 dBW
Downlink Path		***Uplink Path***	
Spacecraft Antenna Pointing Loss	1.9 dB	Ground Station Antenna Pointing Loss	0.2 dB
S/C-to-Ground Antenna Polarization Loss	1.2 dB	Gnd-to-S/C Antenna Polarization Losses	1.2 dB
Path Loss	149.9 dB	Path Loss	140.3 dB
Atmospheric Loss	1.1 dB	Atmospheric Loss	1.1 dB
Ionospheric Loss	0.4 dB	Ionospheric Loss	0.7 dB
Rain Loss	0.0 dB	Rain Loss	0.0 dB
Isotropic Signal Level at Ground Station	-162.9 dBW	Isotropic Signal Level at Spacecraft	-112.5 dBW
Ground Station (EbNo Method)		***Spacecraft (EbNo Method)***	
Ground Station Antenna Pointing Loss	1.3 dB	Spacecraft Antenna Pointing Loss	1.2 dB
Ground Station Antenna Gain	18.9 dBi	Spacecraft Antenna Gain	2.2 dBi
Ground Station Total Transmission Line Losses	2.9 dB	Spacecraft Total Transmission Line Losses	0.3 dB
Ground Station Effective Noise Temperature	965 K	Spacecraft Effective Noise Temperature	203 K
Ground Station Figure of Merit (G/T)	-13.8 dB/K	Spacecraft Figure of Merit (G/T)	-21.2 dB/K
G.S. Signal-to-Noise Power Density (S/No)	50.6 dBHz	Spacecraft Signal-to-Noise Power Density (S/No)	93.7 dBHz
System Desired Data Rate	9600 bps 39.8 dBHz	System Desired Data Rate	1200 bps 30.8 dBHz
Telemetry System Eb/No for the Downlink	10.8 dB	Command System Eb/No	62.9 dB
Demodulation Method Selected	GMSK	Demodulation Method Selected	AFSK/FM
Forward Error Correction Coding Used	None	Forward Error Correction Coding Used	None
System Allowed or Specified Bit-Error-Rate	1.0 e-05	System Allowed or Specified Bit-Error-Rate	1.0 e-05
Demodulator Implementation Loss	0 dB	Demodulator Implementation Loss	1.0 dB

Table 2.17 (continued): Downlink and uplink link budget for VHF and UHF communication

DOWNLINK		UPLINK	
Parameter	**Value**	**Parameter**	**Value**
Telemetry System Required Eb/No	9.6 dB	Telemetry System Required Eb/No	23.2 dB
Eb/No Threshold	9.6 dB	Eb/No Threshold	24.2 dB
System Link Margin	1.2 dB	System Link Margin	38.7 dB
Ground Station Alternative Signal Analysis Method (SNR Computation):			
Ground Station Antenna Pointing Loss	1.3 dB		
Ground Station Antenna Gain	18.9 dBi		
Ground Station Total Transmission Line Losses	2.9 dB		
Ground Station Effective Noise Temperature	965 K		
Ground Station Figure of Merit (G/T)	-13.8 dB/K		
Signal Power at Ground Station LNA Input:	-148.2 dBW		
Ground Station Receiver Bandwidth (B):	500 Hz		
G.S. Receiver Noise Power (Pn = kTB)	-171.8 dBW		
Signal-to-Noise Power Ratio at G.S. Rcvr:	23.6 dB		
Analog or Digital System Required S/N:	9.6 dB		
System Link Margin	14.0 dB		

Link parameters and link margins of S-Band communication between SharjahSat-1 and ground station for downlink are presented in Table 2.18.

Table 2.18: Downlink link budget for S-Band communication

Parameter	Value
Spacecraft	
Spacecraft Transmitter Power Output	1.0 watts 0.0 dBW 30.0 dBm
Spacecraft Total Transmission Line Losses	0.5 dB
Spacecraft Antenna Gain	7.0 dBi
Spacecraft EIRP	6.5 dBW
Downlink Path	
Spacecraft Antenna Pointing Loss	2.3 dB
S/C-to-Ground Antenna Polarization Loss	1.2 dB
Path Loss	164.7 dB
Atmospheric Loss	1.1 dB
Ionospheric Loss	0.0 dB
Rain Loss	0.0 dB
Isotropic Signal Level at Ground Station	-163.0 dBW
Ground Station (EbNo Method)	
Ground Station Antenna Pointing Loss	13.4 dB
Ground Station Antenna Gain	37.6 dBi
Ground Station Total Transmission Line Losses	2.9 dB
Ground Station Effective Noise Temperature	965 K
Ground Station Figure of Merit (G/T)	4.9 dB/K
G.S. Signal-to-Noise Power Density (S/No)	57.1 dBHz
System Desired Data Rate	9600 bps 39.8 dBHz
Telemetry System Eb/No for the Downlink	17.3 dB
Demodulation Method Selected	QPSK
Forward Error Correction Coding Used	None
System Allowed or Specified Bit-Error-Rate	1.0 e-05
Demodulator Implementation Loss	0 dB
Telemetry System Required Eb/No	9.6 dB
Eb/No Threshold	9.6 dB
System Link Margin	7.7 dB
Ground Station Alternative Signal Analysis Method (SNR Computation)	
Ground Station Antenna Pointing Loss	13.4 dB
Ground Station Antenna Gain	37.6 dBi
Ground Station Total Transmission Line Losses	2.9 dB
Ground Station Effective Noise Temperature	965 K
Ground Station Figure of Merit (G/T)	4.9 dB/K
Signal Power at Ground Station LNA Input	-141.7 dBW
Ground Station Receiver Bandwidth (B)	10000 Hz
GS Receiver Noise Power (Pn = kTB)	-158.8 dBW
Signal-to-Noise Power Ratio at GS Rcvr.	17.1 dB
Analog or Digital System Required S/N	16.6 dB
System Link Margin	0.5 dB

2.6 General Operation Phases

There are four main operation modes for SharjahSat-1. These are Leop Mode, Mission Mode, Sun pointing mode and Safe Mode.

2.6.1 Launch and early operation phase (LEOP)

LEOP mode operates after the satellite is deployed from the deployer pod. First, it checks the functionality of the subsystems and after a time period antenna deployment is done. Then, the satellite tries to obtain the desired attitude for missions. After LEOP mode completed, if there are no problem observed with the systems satellite goes to Mission Mode. LEOP mode flow chart is presented in Figure 2.14.

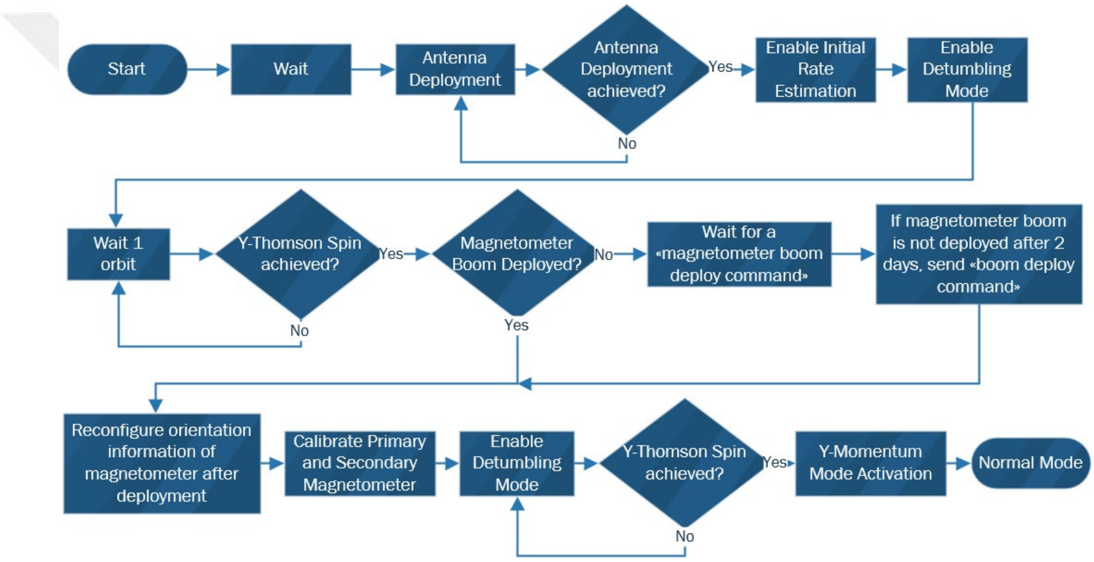

Figure 2.14 : LEOP mode flowchart

2.6.2 Normal operation phase

With normal mode satellite waits for the commands for missions. If battery voltage is in between nominal values and there is no problem with subsystems that prevent the operation, satellite continues to operate the normal mode. Normal mode flow chart shown in Figure 2.15.

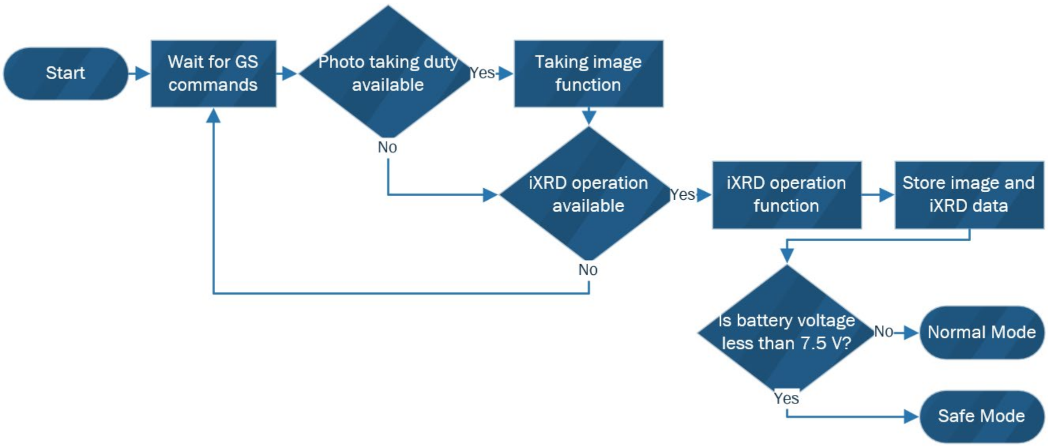

Figure 2.15 : Normal mode flowchart

2.6.3 Safe operation phase

If battery voltage is lower than the acceptable values, then satellite turns off some of the subsystems to recover the power level for mission operations. Safe mode flow chart shown in Figure 2.16.

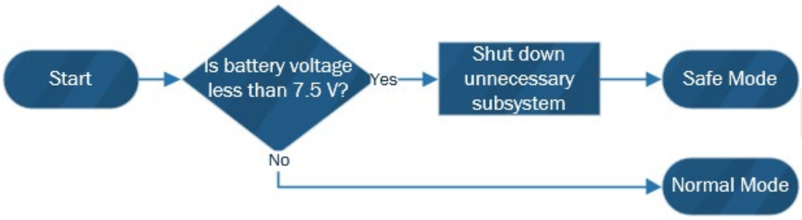

Figure 2.16 : Safe mode flowchart

2.6.4 Mission operations

There will be three different command type for starting missions.

For the main payload, which is the iXRD, scheduled, autonomous and direct X-ray observation mission flowcharts are presented in Figure 2.17.

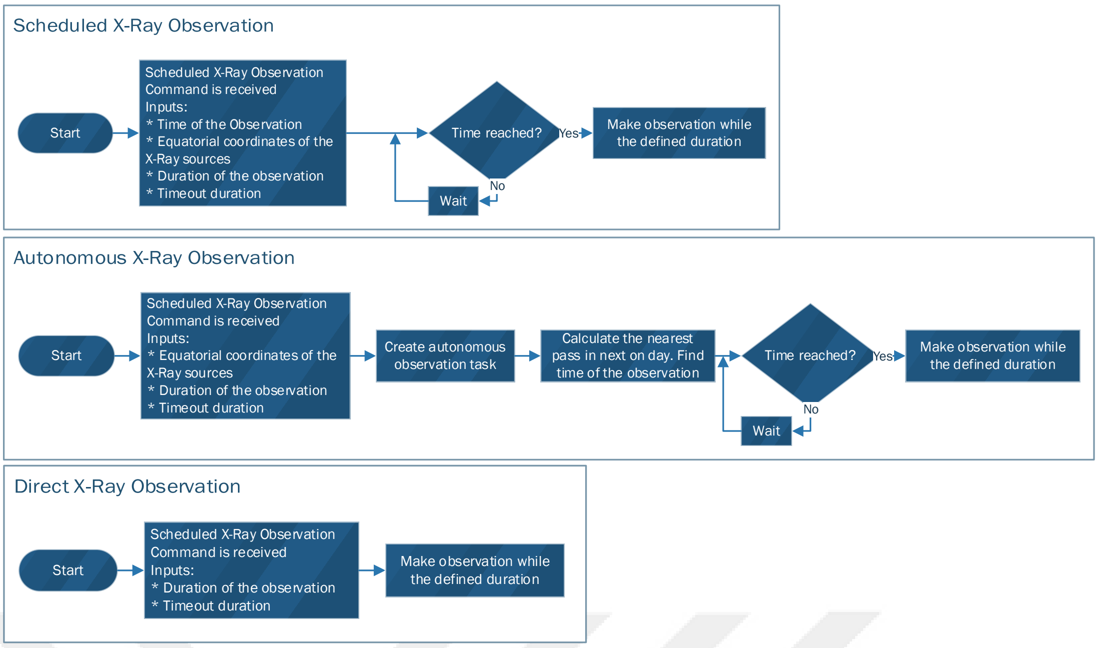

Figure 2.17 : X-Ray observation flowcharts

For the secondary payload, which is the electro-optic camera subsystem, scheduled, autonomous and direct photo mission flowcharts are presented in Figure 2.18.

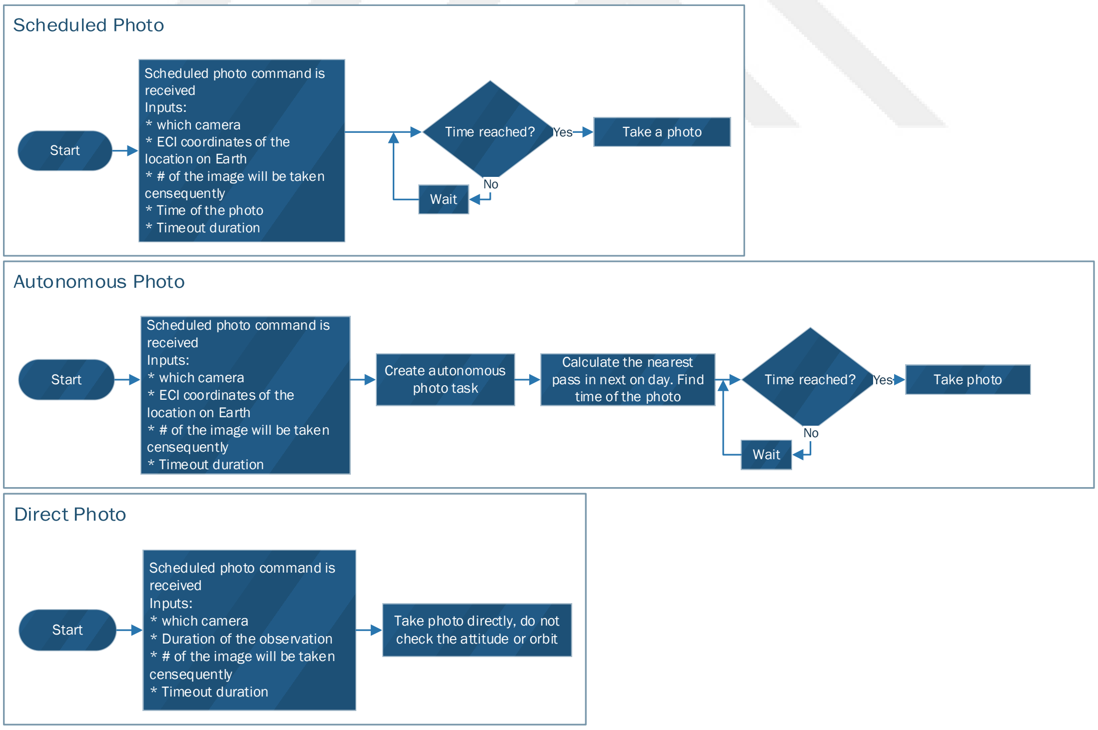

Figure 2.18 : Taking photo flowcharts

2.7 Ground Station

The GS Console software was designed in order to provide mission control attributes such as issuing telecommands and monitoring data. Its functions are given as;

- Issuing Telecommands
- Telemetry reception and processing
- Displaying and storing data
- Real time update

The ground station has antennas and uses a variety of software applications to communicate with the satellite. The SharjahSat-1 GS Console Software makes uses of this other software to provide the user with an effective and simple method to interact with SharjahSat-1 on orbit.

The developed SharjahSat-1 GS Console software can perform the following;

- Issue Telecommands: All available telecommands for SharjahSat-1 are implemented in the software as buttons that the user can simply push. Some telecommands require additional parameters, and the user has to manually enter those. The data is then packaged into the appropriate format for SharjahSat-1, modulated with the help of the AGWPE software and TNC, and sent to the radio as PPT signals.
- Process and Display Telemetry Upon Reception: the AGW Online Kiss software demodulates the received AX.25 frames and sends them to the SharjahSat-1 GS Console software via AGWPE. The obtained values are then displayed on the appropriate boxes.
- Export Telemetry: The software allows for the received telemetry data to be saved on the hard drive as a Microsoft Excel or a comma-separated text file.

3. ATTITUDE DETERMINATION

3.1 Attitude Determination Algorithms

In order to solve the Wahba's problem, TRIAD and QUEST algorithms are used within the scope of this project.

3.1.1 TRIAD algorithm

TRIAD algorithm requires 2 absolute body measurements. As inputs, it takes unit vectors of each measurement to create body frame. Then an inertial frame is created from outside measurement sources, and both frames are utilized in order to create the attitude matrix. The TRIAD frame is represented in Figure 3.1.

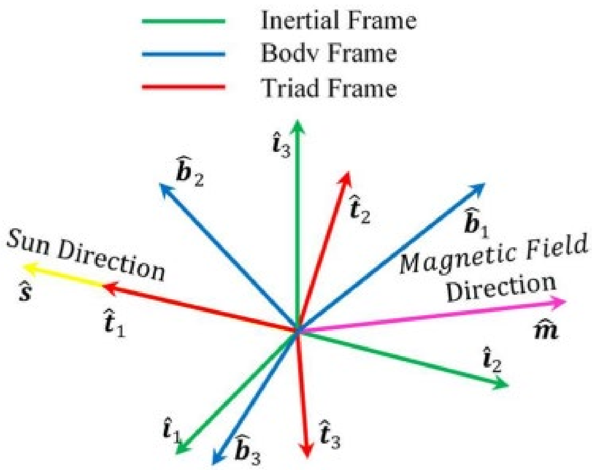

Figure 3.1 : TRIAD frame [20]

This reference frame is constructed by assuming one of the body or inertial vector pairs is correct. In the case which Sun vector measurement is assumed to be correct, the first base vector components will be as (3.1), (3.2) and (3.3). [21]

$$\hat{t}_1 = \hat{s} \tag{3.1}$$

$$t_{1b} = s_b \tag{3.2}$$

$$t_{1i} = s_i \tag{3.3}$$

Then, the second base vector is constructed as (3.4), (3.5) and (3.6).

$$\hat{t}_2 = \hat{s} \times \hat{m} \tag{3.4}$$

$$t_{2b} = \frac{s_b \times m_b}{|s_b \times m_b|} \tag{3.5}$$

$$t_{2i} = \frac{s_i \times m_i}{|s_b \times m_i|} \tag{3.6}$$

The third base vector is constructed as (3.7), (3.8) and (3.9).

$$\hat{t}_3 = \hat{t}_1 \times \hat{t}_2 \tag{3.7}$$

$$t_{3b} = t_{1b} \times t_{2b} \tag{3.8}$$

$$t_{3i} = t_{1i} \times t_{2i} \tag{3.9}$$

Two rotation matrices are constructed as in (3.10) and (3.11)

$$R^{bt} = [t_{1b} \quad t_{2b} \quad t_{3b}] \tag{3.10}$$

$$R^{ti} = [t_{1i} \quad t_{2i} \quad t_{3i}] \tag{3.11}$$

Finally, the desired attitude matrix R^{bi} is calculated as in (3.12). [21]

$$R^{bi} = R^{bt}R^{ti} = [t_{1b} \quad t_{2b} \quad t_{3b}][t_{1i} \quad t_{2i} \quad t_{3i}]^T \tag{3.12}$$

3.1.2 QUEST algorithm

QUEST algorithm is briefly described in Figure 3.2 and Figure 3.3.

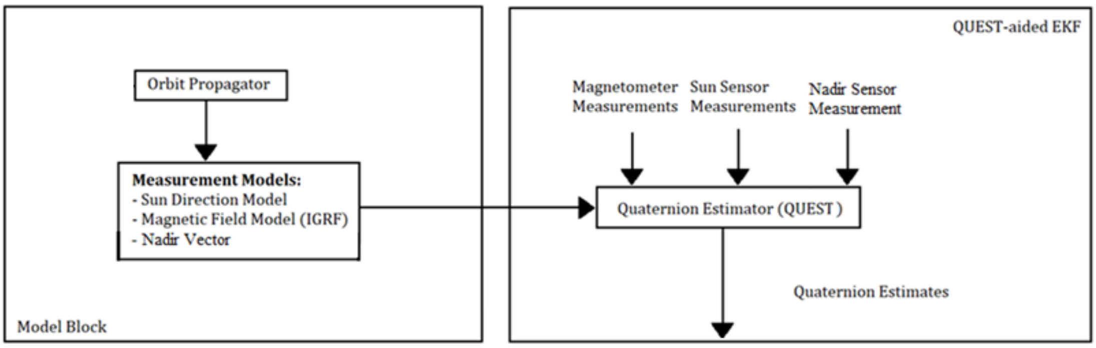

Figure 3.2 : Flowchart for Quest Algorithm for Sun Sensor, Magnetometer and Nadir Sensor Measurements

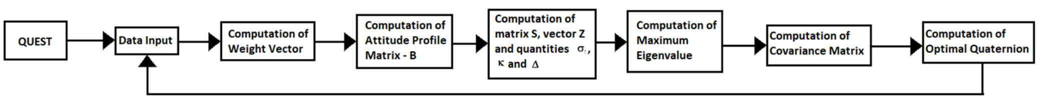

Figure 3.3 : Flowchart for QUEST algorithm

The main purpose of the algorithm is to find an orthogonal matrix A which minimizes the loss function.

$$A\hat{V}_i = \hat{W}_i \qquad (i = 1, \ldots, n) \tag{3.13}$$

$$L(A) = \frac{1}{2}\sum_{i=1}^{n} a_i \left|\hat{W}_i - A\hat{V}_i\right|^2 \tag{3.14}$$

Loss function can be scaled without affecting the determination of A, so it is possible to state as (3.15)

$$\sum_{i=1}^{n} a_i = 1 \tag{3.15}$$

Then, the gain function, $g(A)$, is defined as (3.16)

$$g(A) = 1 - L(A) = \sum_{i=1}^{n} a_i tr\left[\hat{W}_i^T A\hat{V}_i\right] = tr[AB^T] \tag{3.16}$$

Attitude profile matrix, B, is given as (3.17)

$$B = \sum_{i=1}^{n} a_i \hat{W}_i^T \hat{V}_i \tag{3.17}$$

Gain function be written by 4x4 matrix, and takes a quadratic form shown in (3.18)

$$g(\bar{q}) = \bar{q}^T K \bar{q} \tag{3.18}$$

K matrix is defined as the combination of a couple of matrices.

$$K = \begin{bmatrix} S - \sigma I & Z \\ Z^T & \sigma \end{bmatrix} \tag{3.19}$$

$$\sigma = trB = \sum_{i=1}^{n} a_i \hat{W}_i \cdot \hat{V}_i \tag{3.20}$$

$$S = B + B^T = \sum_{i=1}^{n} a_i (\hat{W}_i \hat{V}_i^{\,2} + \hat{V}_i \hat{W}_i^{\,2}) \tag{3.21}$$

$$Z = \sum_{i=1}^{n} a_i (\hat{W}_i \times \hat{V}_i) = B - B^T \tag{3.22}$$

Lagrange multipliers method is applied and a new gain function is defined maximized without constraint.

$$g'(\bar{q}) = \bar{q}^T K\bar{q} - \lambda\bar{q}^T\bar{q} \tag{3.23}$$

Then, λ is chosen to satisfy the constraint.

$$K\bar{q} = \lambda\bar{q} \tag{3.24}$$

Equations are rearranged to read for any eigenvalue.

$$Y = [(\lambda + \sigma)I - S]^{-1}Z \tag{3.25}$$

$$\lambda = \sigma + \boldsymbol{Z} \cdot \boldsymbol{Y} \tag{3.26}$$

In terms of Gibbs vector, the equation becomes as (3.27)

$$\bar{q} = \frac{1}{\sqrt{1 + Y^T Y}}\begin{bmatrix}1\\Y\end{bmatrix} \tag{3.27}$$

When λ is equal to λ_{max}, $\boldsymbol{Y}$ and $\bar{q}$ are representation of the optimal attitude solution. [22]

3.2 Attitude Determination Sensors

Within the attitude determination algorithms, 4 different sensor models are used. These are CSSs, FSSs, nadir sensor and magnetometer. These sensor models will be implemented on TRIAD and QUEST algorithms. While testing the algorithm, sensor accuracies are assumed as given in Table 3.1

Table 3.1: Sensor accuracies

Sensor	**Accuracy/Measurement Noise**
Sun Sensor	0.2 deg
Magnetometer	50 nT
Nadir Sensor	0.2 deg

Magnetometer sensor is modelled as in (3.28) and (3.29).

$$v_m = \pm 50\ nT \tag{3.28}$$

$$\bar{m}^B = m^B + v_m \tag{3.29}$$

Sun sensor is modelled as follows (3.30) and (3.31).

$$v_s = \pm 0.2° \tag{3.30}$$

$$\bar{m}^s = s^B + v_s \tag{3.31}$$

Nadir sensor is modelled as follows (3.32) and (3.33).

$$v_n = \pm 0.2° \tag{3.32}$$

$$\bar{m}^n = n^B + v_n \tag{3.33}$$

For attitude determination of SharjahSat-1, collected sensor measurement telemetries are used. For magnetometer, since configuration parameters may not be calibrated, calibrated magnetic field vector measurements are obtained by using latest valid sensitivity and offset values. After calibration is completed, ADCS time shift is calculated by using collected ADCS telemetries, which are IGRF magnetic field and magnetometer measurements. [23]

3.3 Attitude Determination and Control in SharjahSat-1

Positions and reference frames of sensors with respect to flight coordinate system are presented in Table 3.2 and Figure 3.4.

Table 3.2: Sensor positions

Sensor	Mounted On	Sensor	Mounted On
Magnetometer	+X	CSS 4	-Z
Redundant Magnetometer	+X	CSS 5	+Y
Fine Sun Sensor	-Z	CSS 6	+Y
Nadir Sensor	+Z	CSS 7	-X
Star Tracker	-Y	CSS 8	+X
CSS 1	-Y	CSS 9	+Z
CSS 2	-Y	CSS 10	+Z
CSS 3	-Z		

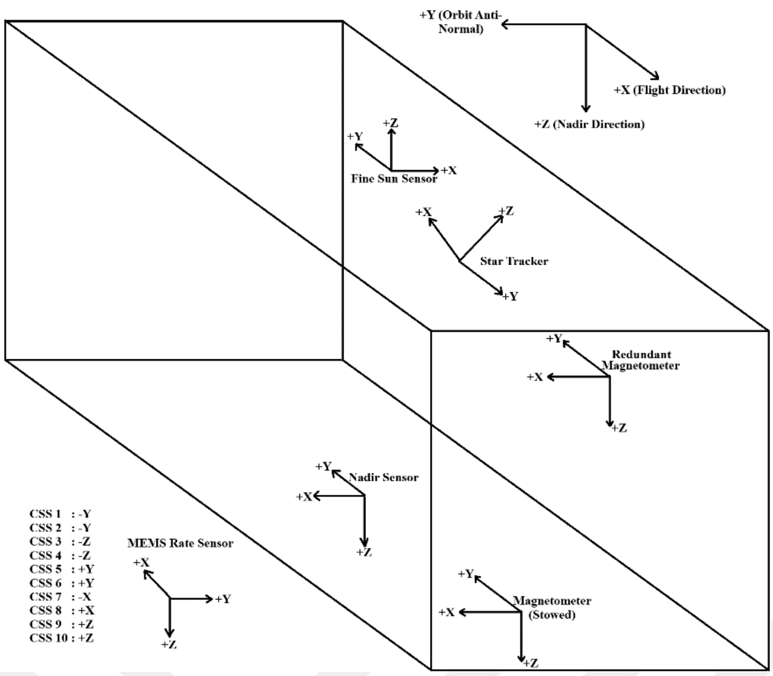

Figure 3.4 Sensor positions and reference frames

3.3.1 Attitude estimation in SharjahSat-1

ADCS estimation mode determines which attitude sensors are used and which attitude data is estimated. In current system, there are 6 different attitude estimation modes. The estimation mode can be changed by using Set Attitude Estimation Mode telecommand (TC ID 14). The estimation modes with the used sensors and estimated data are presented in Table 3.3.

Table 3.3: Attitude estimation modes in SharjahSat-1

No	Estimation Mode	Sensors Used	Estimated Information
0	No attitude estimation	None	None
1	MEMS rate sensing	X,Y,Z –axis rate sensors	X,Y,Z angular rates
2	Magnetometer rate filter	Magnetometer	X,Y,Z angular rates
3	Magnetometer rate filter with pitch angle estimator	Magnetometer	X,Y,Z angular rates; pitch angle
4	Magnetometer and fine or coarse Sun TRIAD algorithm	Magnetometer; CSS and/or Sun sensor	Roll, Pitch & Yaw angles; X,Y,Z angular rates
5	Full-state EKF	Magnetometer; Sun sensor; Nadir sensor; Star tracker	Roll, Pitch & Yaw angles; X,Y,Z angular rates
6	MEMS Gyro EKF	X,Y,Z–axis rate sensors; Magnetometer; Sun sensor; Nadir sensor; Star tracker	Roll, pitch & Yaw angles; X,Y,Z angular rates; X,Y,Z gyro bias

Estimation Mode 1 provides angular rate measurements for all the body axes. It does not perform any estimation algorithms and uses rate sensor measurements directly. Estimation Mode 2 uses successive magnetometer rate measurements in a robust Kalman filter to estimate the X, Y and Z angular rates. Estimation Mode 3 is similar to mode 2 but also includes simple pitch estimation. Estimation Mode 4 combines mode 2 with TRIAD algorithm, which gives estimated attitude angles based on modelled and measured vectors. Estimation Mode 5 uses an Extended Kalman Filter (EKF) to estimate the full attitude state. The estimator uses satellite moment of inertia tensor and estimated control torque in order to propagate the attitude state. Estimation Mode 6 uses an EKF with the MEMS rate (gyro) measurements to estimate the attitude and rate sensor offsets (gyro bias).

3.3.2 Attitude control in SharjahSat-1

ADCS control mode determines which attitude actuators are used. In current system, there are a total of 15 different attitude control modes. The control mode can be changed by using Set Attitude Control Mode telecommand (TC ID 13). The control modes with the used actuators and required estimated state are presented in Table 3.4.

Table 3.4: Attitude control modes in SharjahSat-1

No	Control Mode	Actuators Used	Required estimated state
0	No control	None	None
1	Detumbling control	Y-Magnetorquer	None
2	Y-Thomson spin	XYZ magnetorquers	Y-body rate
3	Y-Momentum wheel (Initial pitch acquisition)	Y-Momentum wheel & XYZ magnetorquers	X-,Y-,Z- body rates & pitch angle
4	Y-Momentum wheel (Steady state)	Y-Momentum wheel & XYZ magnetorquers	X-,Y-,Z- body rates & pitch angle
5	XYZ wheel control	XYZ reaction wheels & XYZ magnetorquers	X-,Y-,Z- body rates & Roll, pitch and yaw attitude
6	R-wheel Sun tracking control	XYZ reaction wheels & XYZ magnetorquers	X-,Y-,Z- body rates & Roll, pitch and yaw attitude
7	R-wheel target tracking control	XYZ reaction wheels & XYZ magnetorquers	X-,Y-,Z- body rates & Roll, pitch and yaw attitude
8	Very Fast-spin Detumbling control	XYZ magnetorquers	None
9	Fast-spin Detumbling control	XYZ magnetorquers	None
10	User Specific Control Mode 1	<reserved>	<reserved>
11	User Specific Control Mode 2	<reserved>	<reserved>
12	Stop XYZ Reaction wheels	XYZ reaction wheels	None
13	User-coded Control Mode	<reserved>	<reserved>
14	Sun-tracking yaw- or roll-only wheel control mode	XYZ reaction wheels & XYZ magnetorquers	X-,Y-,Z- body rates & Roll, pitch and yaw attitude
15	Target-tracking yaw-only wheel control Mode	XYZ reaction wheels & XYZ magnetorquers	X-,Y-,Z- body rates & Roll, pitch and yaw attitude

Control Mode 1 uses a Bdot Detumbling magnetic controller to dump the X- and Z body rates. Control Mode 2 adds Y-Thomson Spin to Mode 1 using the X- and Z-axis magnetorquers. Control Mode 3 absorbs most of the body Y-Thomson spin, but keep a slow pitch rotation about the Y-axis. Control Mode 4 uses a PD controller to control the pitch angle to the reference pitch angle. Control Mode 5 keeps the attitude as nadir pointing (for zero roll, pitch and yaw angles). Control Mode 6 is used to track the Sun vector normal to the satellite's solar panels for maximum power generation. Control Mode 7 is used to track a reference ground target at a specific location on Earth. Control Mode 8 can detumble initial body rates in all axes as high as 1000 deg/s down to zero. Control Mode 9 can detumble initial body rates in all axes as high as 100 deg/s down to zero.

Before setting a control mode, estimation mode should be set to a correct mode. An estimation mode may not be compatible with the selected control mode. Therefore, Table 3.5 should be checked. If an invalid combination of modes is tried to be set, control mode set command will fail. OK entries are the preferred combinations, OK* entries are also acceptable, and X entries are not acceptable.

Table 3.5: Valid estimation and control combinations

Estimation mode	**Control mode**				
	0	**1, 8, 9**	**2**	**3, 4**	**5, 6, 7, 12, 14, 15**
0	OK	OK	X	X	X
1	OK	OK	OK	X	X
2	OK*	OK	OK	X	X
3	OK*	OK	OK	OK	X
4	OK*	OK	OK	OK*	X
5	OK*	OK*	OK*	OK	OK
6	OK*	OK*	OK*	OK	OK

Moreover, there are also valid and invalid control mode transitions. These are shown in Table 3.6.

Table 3.6: Valid control transitions

Current control mode	**New control mode**					
	0	**1, 8, 9**	**2**	**3**	**4**	**5, 6, 7, 12, 14, 15**
0	N/A	OK	OK*	X	OK*	OK*
1, 8, 9	OK	N/A	OK	X	X	OK*
2	OK	OK	N/A	OK	X	X
3	OK	OK	OK	N/A	OK	X
4	OK	OK	OK	X	N/A	OK
5, 6, 7, 12, 14, 15	OK	OK	OK	X	X	N/A

3.3.3 Sensor and actuator performance analysis

3.3.3.1 Detumbling

The results from the simulations for the rate sensor rates while the satellite is in Detumbling mode is shown in Figure 3.5. It is seen that each component of the angular rate does not reach 0.25 °/s in magnitude.

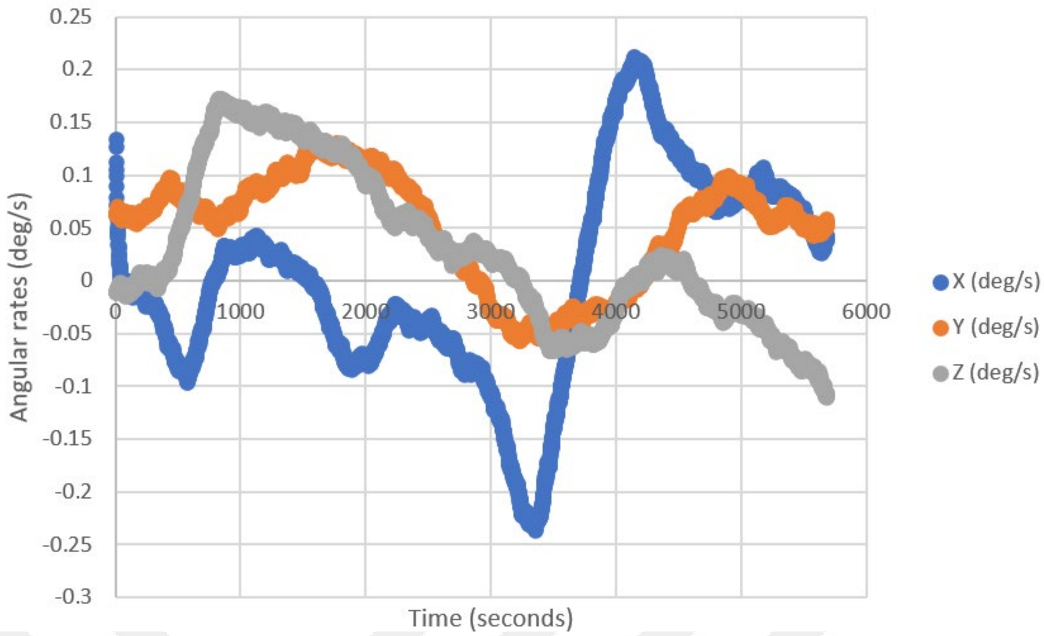

Figure 3.5: Simulation results for the rate sensor rates

Measured magnetic field angle error is investigated for the magnetometer performance comparison in simulations, which is shown in Figure 3.6. The redundant magnetometer error is higher as expected since the it is located closer to the sources of the magnetic field disturbance within the satellite. Maximum and mean errors for deployable and redundant magnetometer are given in Table 3.7.

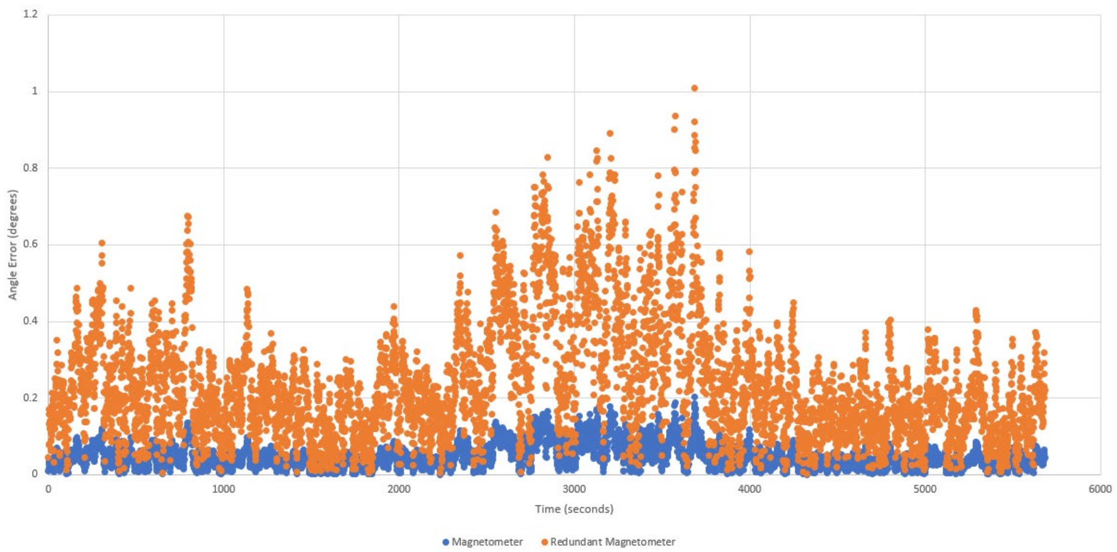

Figure 3.6: Simulation results of measured magnetic field angle error for magnetometer and redundant magnetometer

Table 3.7: Maximum and mean errors for deployable and redundant magnetometer

Sensor	Max Error	Mean Error
Deployable Magnetometer	0.202226	0.046551
Redundant Magnetometer	1.008944	0.232714

The comparison of the modelled Sun vector, coarse sun sensor vector and fine sun sensor vector is given in Figure 3.7. Also, it can be seen that FSS X data corresponds with negative values of modelled Y and CSS Y data, FSS Y data corresponds with negative values of modelled X and CSS X data, and FSS Z data corresponds with negative values of modelled Z and CSS Z data. As expected, the coarse sun sensor vector accuracy is less compared to fine sun sensor, which is also shown in Figure 3.8. However, since FSS has a limited FoV, and the satellite is in detumbling control mode, the FSS Sun vector measurements are discontinuous. Maximum and mean errors for CSS and FSS are given in Table 3.8.

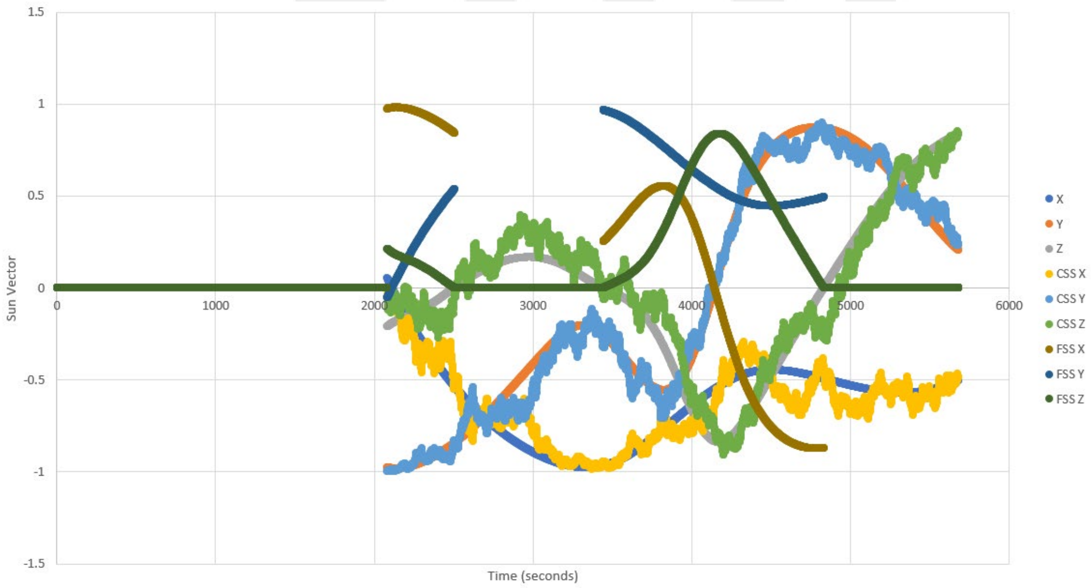

Figure 3.7: Simulation results for modelled sun, fine sun sensor and coarse sun sensor vectors

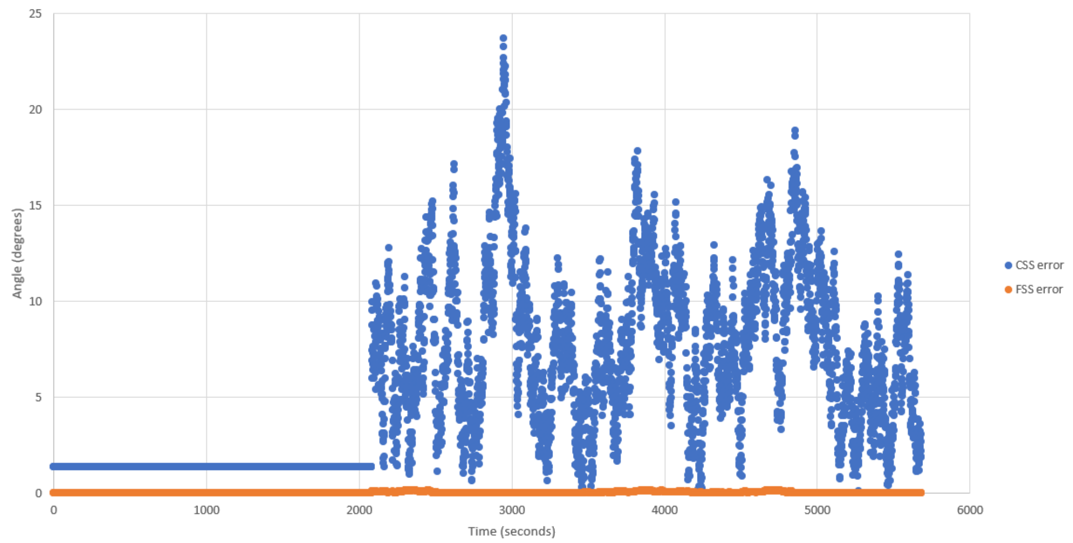

Figure 3.8: Simulation results for CSS and FSS Sun angle measurement error

Table 3.8: Maximum and mean errors for CSS and FSS

Sensor	**Max Error**	**Mean Error**
CSS	23.706500	7.836760
FSS	0.170965	0.076603

Also, again due to the limited FoV of the nadir sensor and the detumbling control mode of the satellite, the nadir vector measurements are not calculated even though the Sun is above the horizon. The simulation results for nadir vector angle measurement error are presented in Figure 3.9. Maximum and mean errors for nadir sensor is given in Table 3.9.

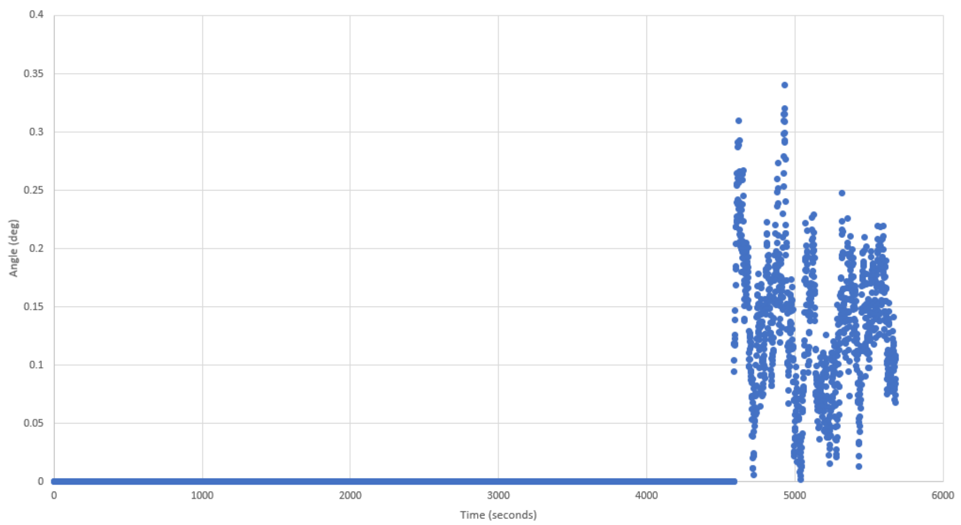

Figure 3.9: Simulation results for nadir vector angle measurement error

Table 3.9: Maximum and mean errors for Nadir sensor

Sensor	Max Error	Mean Error
Nadir Sensor	0.340584	0.133231

The simulation results for pointing error across and around star tracker FoV is presented in Figure 3.10. Maximum and mean errors for across and around star tracker FoV are given in Table 3.10.

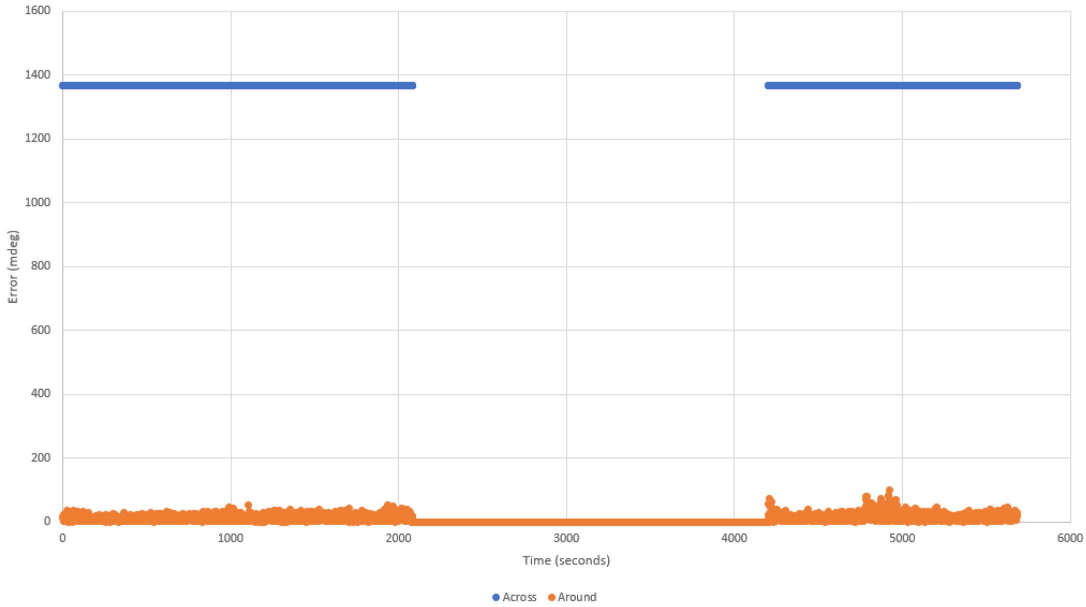

Figure 3.10: Simulation results for pointing error across and around star tracker FoV

Table 3.10: Maximum and mean errors for across and around Star tracker FoV

Sensor	Max Error	Mean Error
Across	1368.895000	859.471561
Around	101.063600	8.386192

3.3.3.2 Y-Thomson spin mode

The results from the simulations for the rate sensor rates while the satellite is in Detumbling mode is shown in Figure 3.11. It is seen that each component of the angular rate does not reach 1.5 °/s in magnitude. Also, it can be seen that the Y component of the angular rate is tried to be kept around +1 deg/s, in order to accomplish a +Y spin.

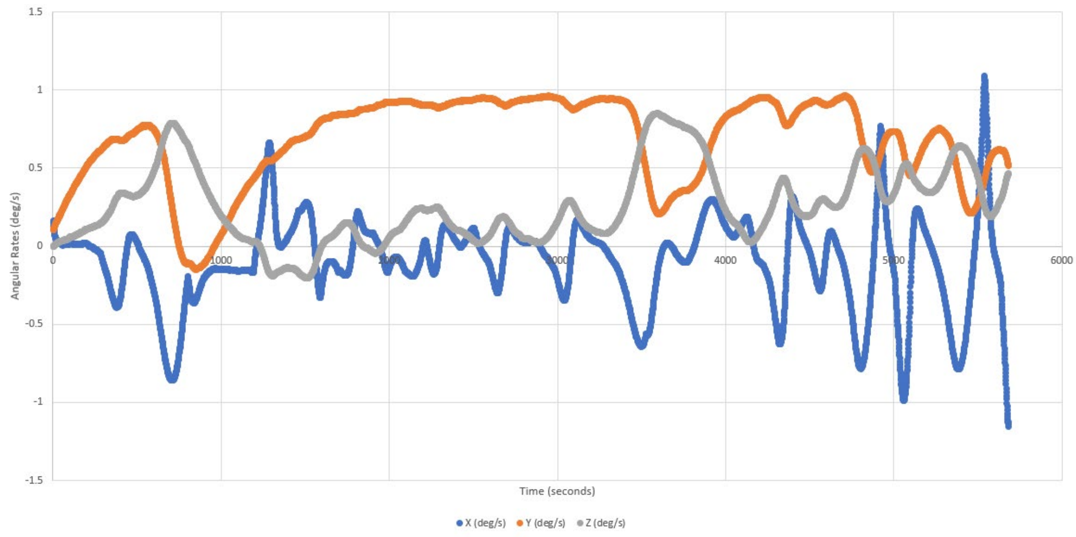

Figure 3.11: Simulation results for the rate sensor rates

Measured magnetic field angle error is investigated for the magnetometer performance comparison in simulations, which is shown in Figure 3.12. The redundant magnetometer error is higher as expected since the it is located closer to the sources of the magnetic field disturbance within the satellite. Maximum and mean errors for deployable and redundant magnetometer are given in Table 3.11.

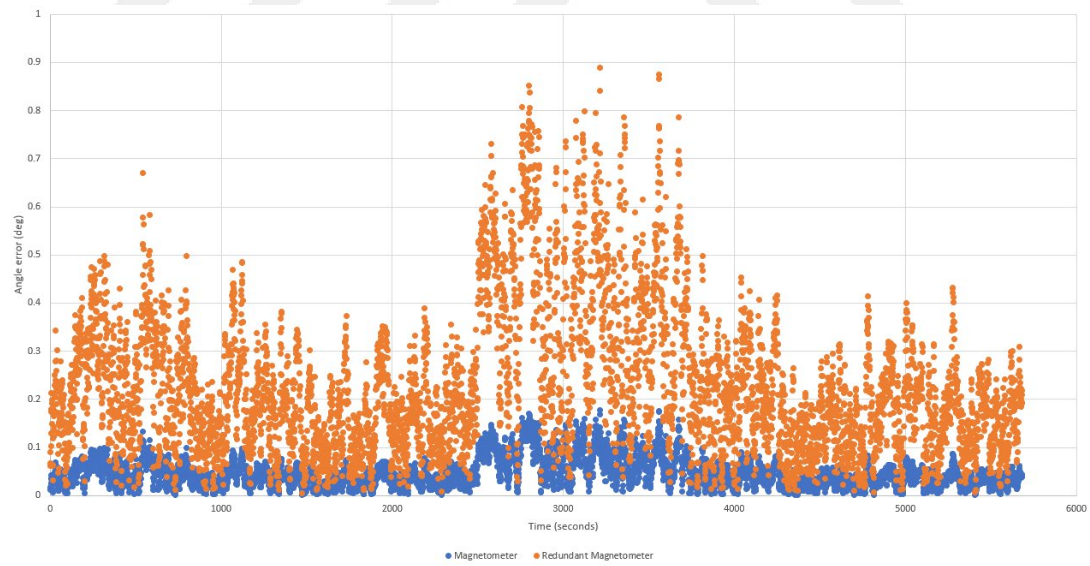

Figure 3.12: Simulation results of measured magnetic field angle error for magnetometer and redundant magnetometer

Table 3.11: Maximum and mean errors for deployable and redundant magnetometer

Sensor	Max Error	Mean Error
Deployable Magnetometer	0.177547	0.045649
Redundant Magnetometer	0.888710	0.228265

The comparison of the modelled Sun vector, coarse sun sensor vector and fine sun sensor vector is given in Figure 3.13. As expected, the coarse sun sensor vector accuracy is less compared to fine sun sensor, which is also shown in Figure 3.14. However, since FSS has a limited FoV, and the satellite is in detumbling control mode, the FSS Sun vector measurements are discontinuous. Maximum and mean errors for CSS and FSS are given in Table 3.12.

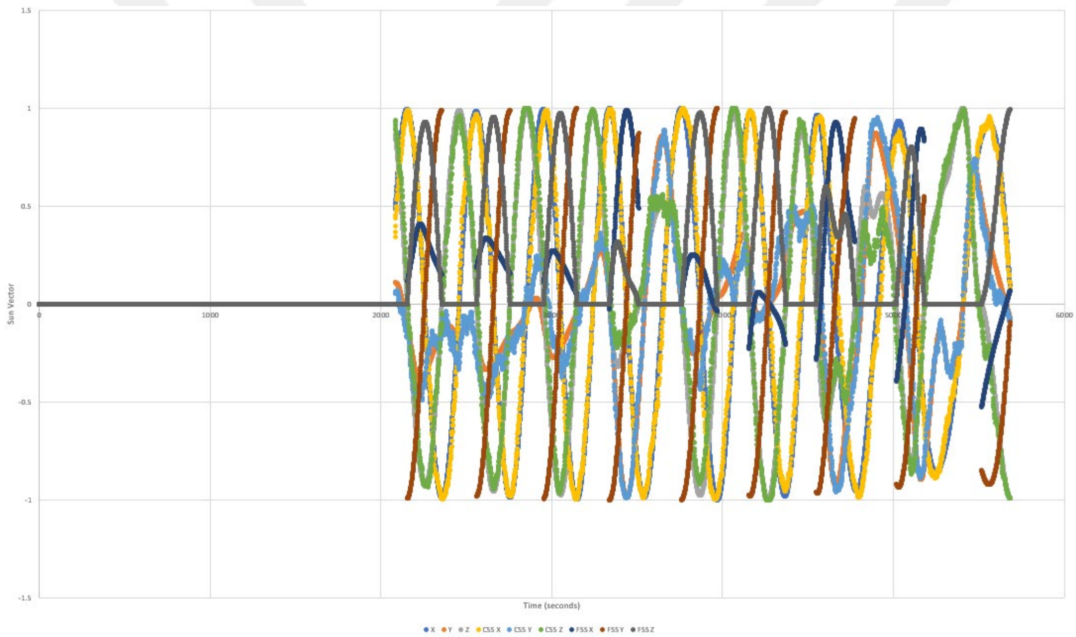

Figure 3.13: Simulation results for modelled sun, fine sun sensor and coarse sun sensor vectors

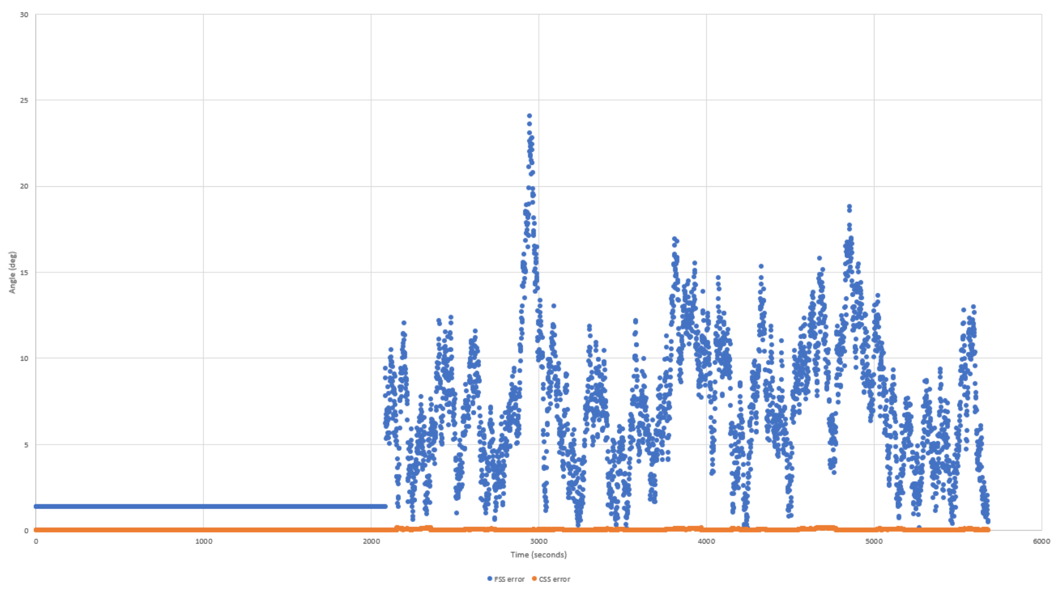

Figure 3.14: Simulation results for CSS and FSS Sun angle measurement error

Table 3.12: Maximum and mean errors for CSS and FSS

Sensor	Max Error	Mean Error
CSS	0.171056	0.029563
FSS	0.171056	0.086856

Also, again due to the limited FoV of the nadir sensor and the detumbling control mode of the satellite, the nadir vector measurements are not calculated even though the Sun is above the horizon. The simulation results for nadir vector angle measurement error are presented in Figure 3.15. Maximum and mean errors for nadir sensor are given in Table 3.13.

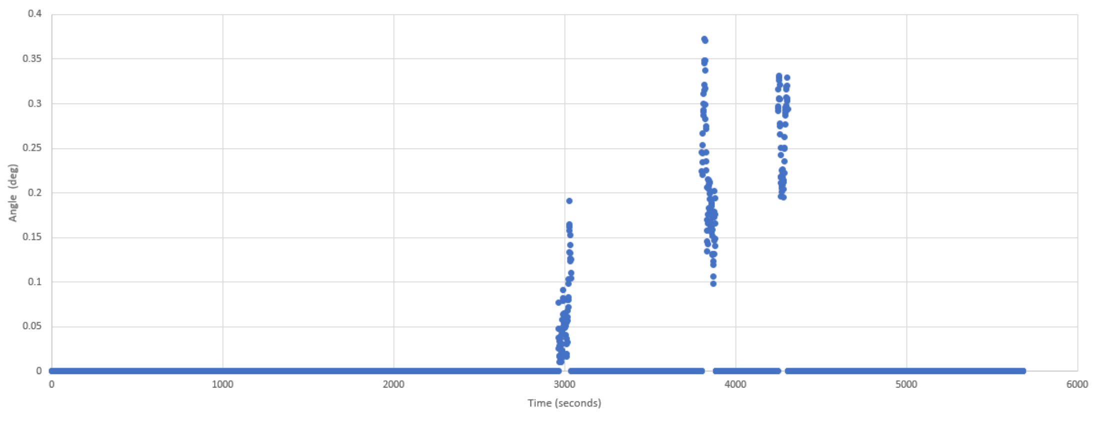

Figure 3.15: Simulation results for nadir vector angle measurement error

Table 3.13: Maximum and mean errors for nadir sensor

Sensor	Max Error	Mean Error
Nadir Sensor	0.372614	0.174667

The simulation results for pointing error across and around star tracker FoV is presented in Figure 3.16. Maximum and mean errors for across and around star tracker FoV are given in Table 3.14.

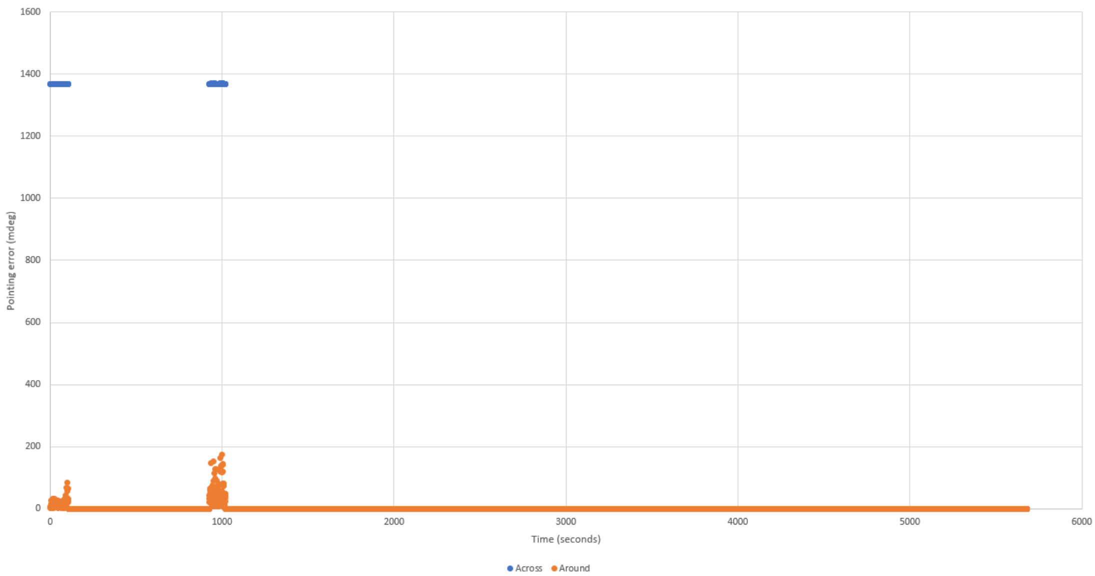

Figure 3.16: Simulation results for pointing error across and around star tracker FoV

Table 3.14: Maximum and mean errors for across and around star tracker FoV

Sensor	Max Error	Mean Error
Across	1370.107000	48.528664
Around	175.784400	1.224108

3.3.3.3 Nadir pointing mode

The results from the simulations for the rate sensor rates while the satellite is in Detumbling mode is shown in Figure 3.17. It is seen that each component of the angular rate does not reach 0.15 °/s in magnitude.

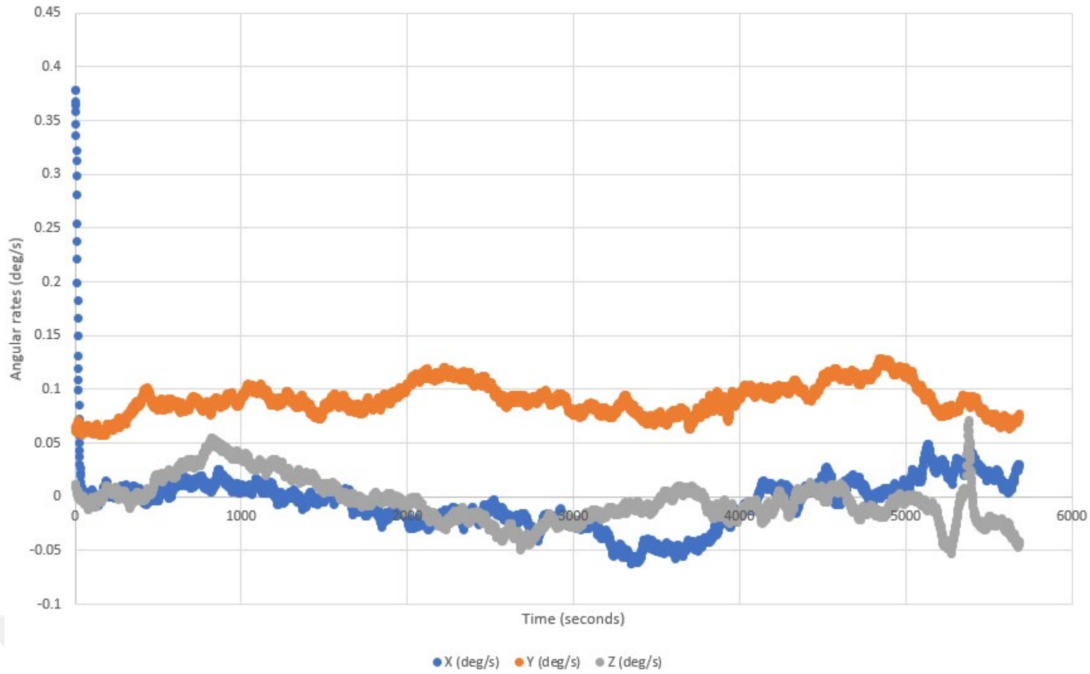

Figure 3.17: Simulation results for the rate sensor rates

Measured magnetic field angle error is investigated for the magnetometer performance comparison in simulations, which is shown in Figure 3.18. The redundant magnetometer error is higher as expected since the it is located closer to the sources of the magnetic field disturbance within the satellite. Maximum and mean errors for deployable and redundant magnetometer are given in Table 3.15.

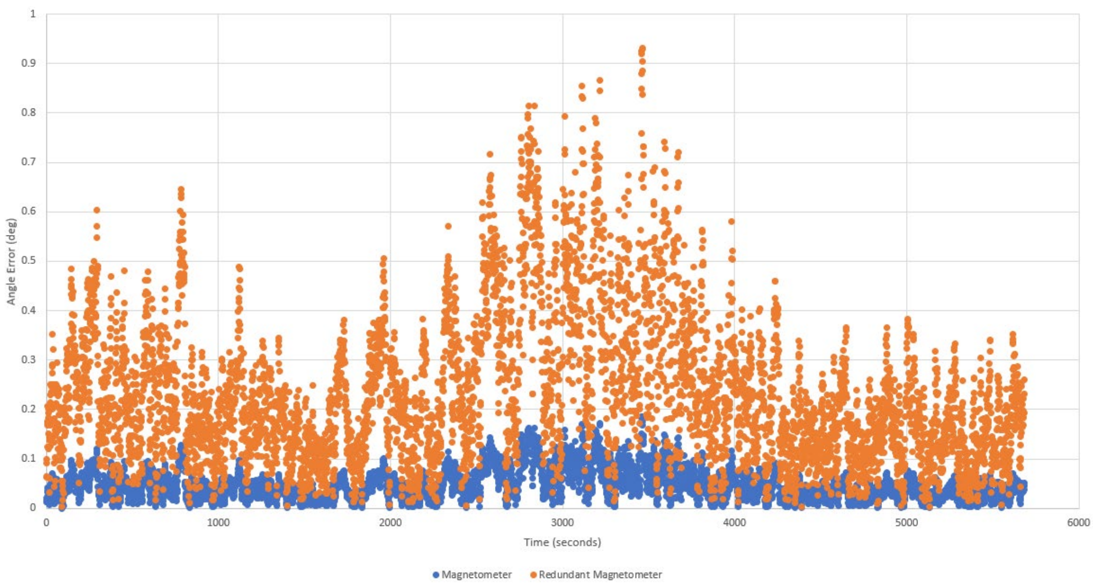

Figure 3.18: Simulation results of measured magnetic field angle error for magnetometer and redundant magnetometer

Table 3.15: Maximum and mean errors for deployable and redundant magnetometer

Sensor	Max Error	Mean Error
Deployable Magnetometer	0.186038	0.046455
Redundant Magnetometer	0.930428	0.232386

The comparison of the modelled Sun vector, coarse sun sensor vector and fine sun sensor vector is given in Figure 3.19. As expected, the coarse sun sensor vector accuracy is less compared to fine sun sensor, which is also shown in Figure 3.20. However, since FSS has a limited FoV, and the satellite is in detumbling control mode, the FSS Sun vector measurements are discontinuous. Maximum and mean errors for CSS and FSS are given in Table 3.16.

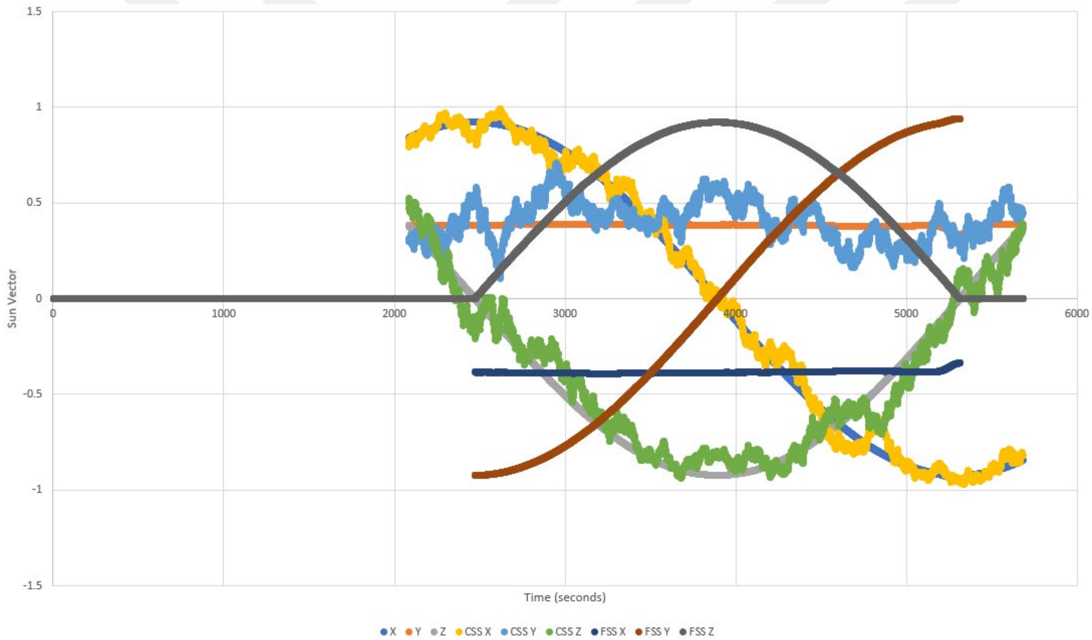

Figure 3.19: Simulation results for modelled sun, fine sun sensor and coarse sun sensor vectors

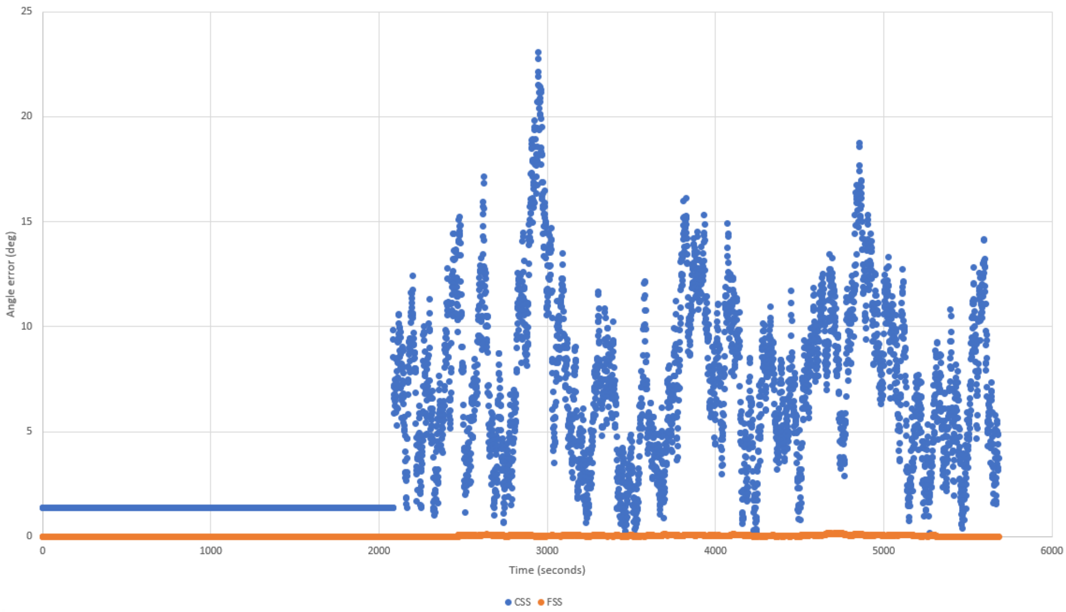

Figure 3.20: Simulation results for CSS and FSS Sun angle measurement error

Table 3.16: Maximum and mean errors for CSS and FSS

Sensor	Max Error	Mean Error
CSS	23.05732	7.503612632
FSS	0.1697263	0.054175343

Also, again due to the limited FoV of the nadir sensor and the detumbling control mode of the satellite, the nadir vector measurements are not calculated even though the Sun is above the horizon. The simulation results for nadir vector angle measurement error are presented in Figure 3.21. Maximum and mean errors for nadir sensor are given in Table 3.17.

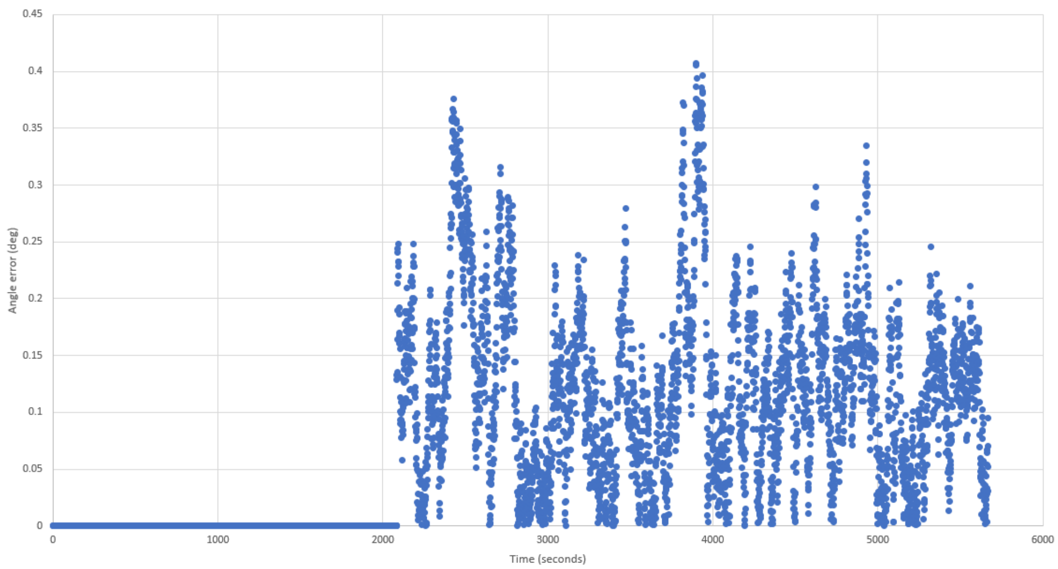

Figure 3.21: Simulation results for nadir vector angle measurement error

Table 3.17: Maximum and mean errors for nadir sensor

Sensor	Max Error	Mean Error
Nadir Sensor	0.4071052	0.119707294

The simulation results for pointing error across and around star tracker FoV is presented in Figure 3.22. Maximum and mean errors for across and around star tracker FoV are given in Table 3.18.

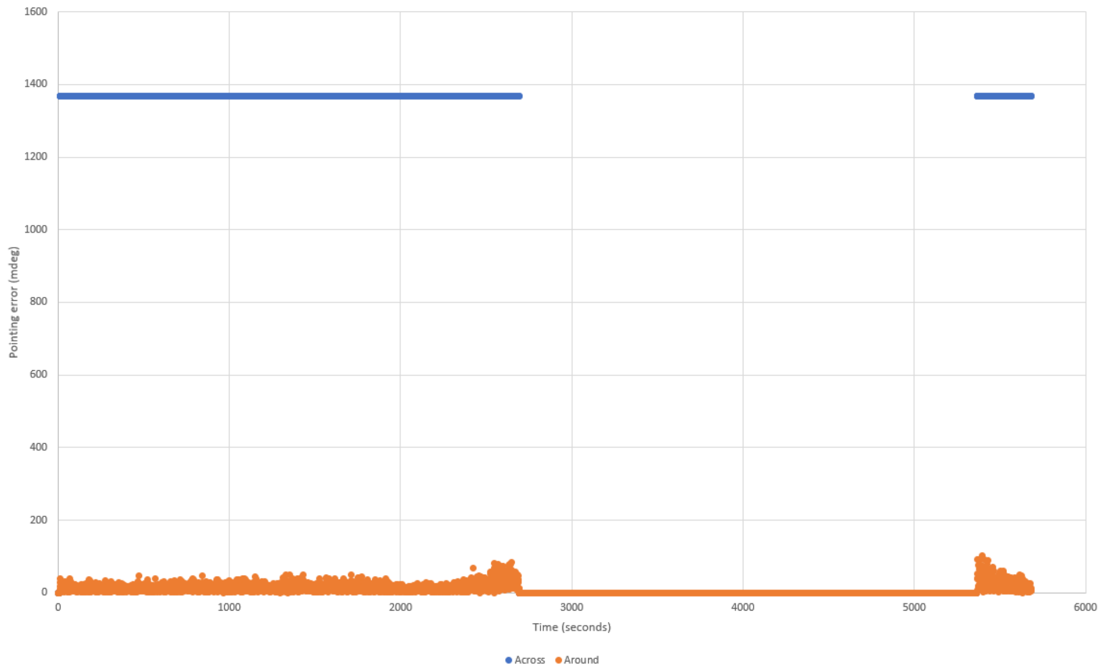

Figure 3.22: Simulation results for pointing error across and around star tracker FoV

Table 3.18: Maximum and mean errors for across and around star tracker FoV

Sensor	Max Error	Mean Error
Across	1368.597000	1368.242440
Around	101.264300	15.141074

3.3.3.4 Target tracking mode

The results from the simulations for the rate sensor rates while the satellite is in Detumbling mode is shown in Figure 3.23. It is seen that each component of the angular rate does not reach 0.25 °/s in magnitude.

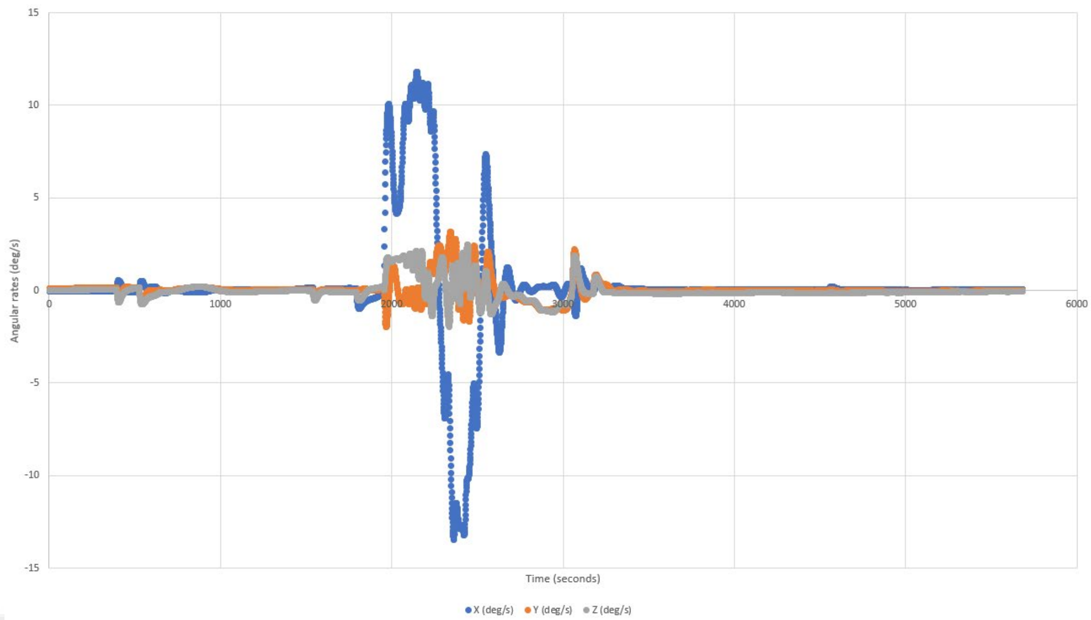

Figure 3.23: Simulation results for the rate sensor rates

Measured magnetic field angle error is investigated for the magnetometer performance comparison in simulations, which is shown in Figure 3.24. The redundant magnetometer error is higher as expected since the it is located closer to the sources of the magnetic field disturbance within the satellite. Maximum and mean errors for deployable and redundant magnetometer are given in Table 3.19.

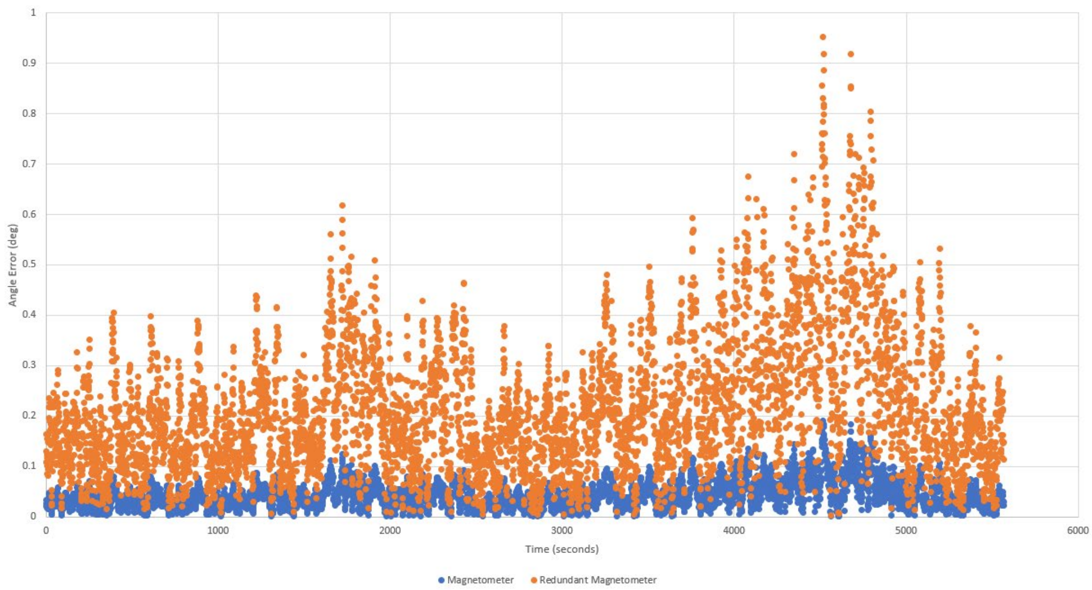

Figure 3.24: Simulation results of measured magnetic field angle error for magnetometer and redundant magnetometer

Table 3.19: Maximum and mean errors for deployable and redundant magnetometer

Sensor	Max Error	Mean Error
Deployable Magnetometer	0.181586	0.047348
Redundant Magnetometer	0.907106	0.236812

The comparison of the modelled Sun vector, coarse sun sensor vector and fine sun sensor vector is given in Figure 3.25. As expected, the coarse Sun sensor vector accuracy is less compared to fine sun sensor, which is also shown in Figure 3.26. However, since FSS has a limited FoV, and the satellite is in detumbling control mode, the FSS Sun vector measurements are discontinuous. Maximum and mean errors for CSS and FSS are given in Table 3.20.

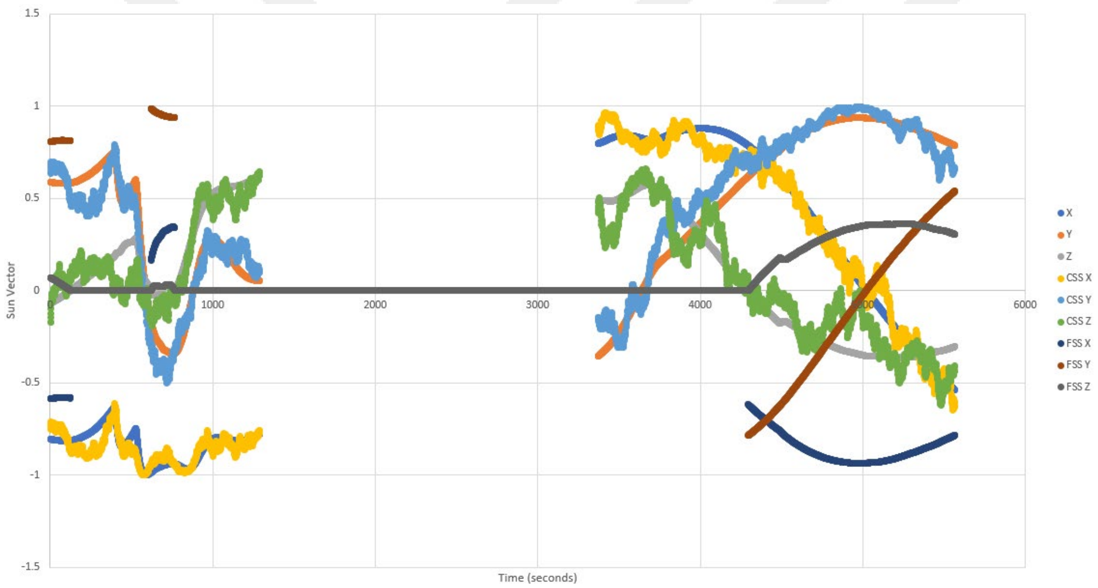

Figure 3.25: Simulation results for modelled sun, fine sun sensor and coarse sun sensor vectors

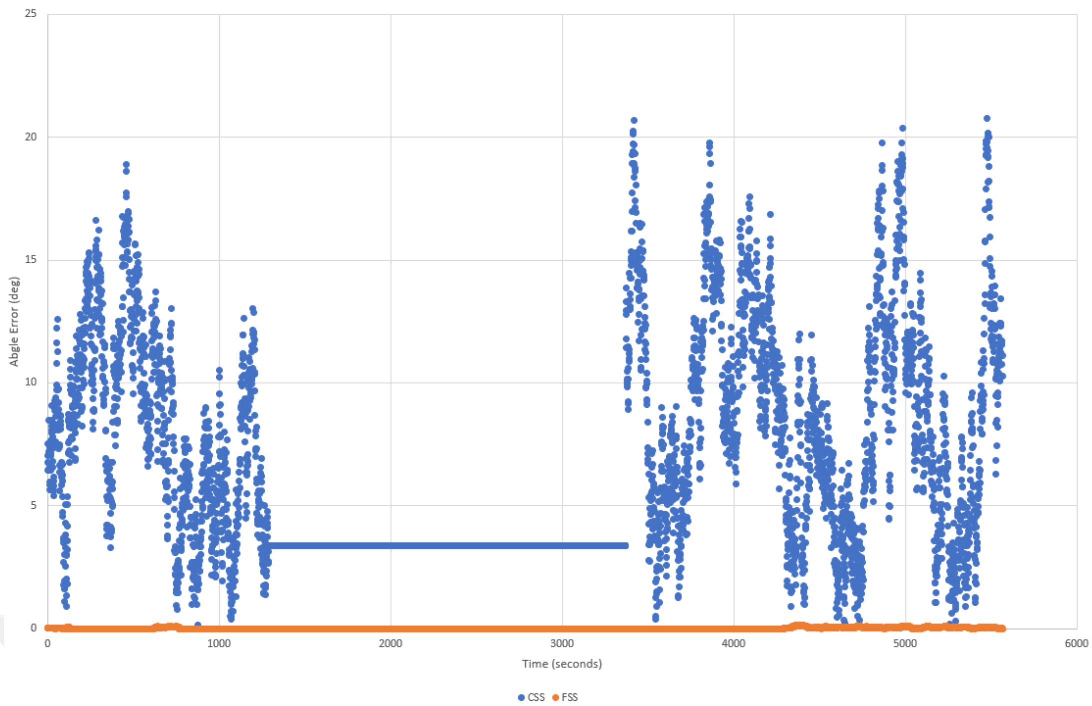

Figure 3.26: Simulation results for CSS and FSS Sun angle measurement error

Table 3.20: Maximum and mean errors for CSS and FSS

Sensor	Max Error	Mean Error
CSS	20.75296	7.537516184
FSS	20.75296	0.055791238

Also, again due to the limited FoV of the nadir sensor and the detumbling control mode of the satellite, the nadir vector measurements are not calculated even though the Sun is above the horizon. The simulation results for nadir vector angle measurement error are presented in Figure 3.27. Maximum and mean errors for nadir sensor are given in Table 3.21.

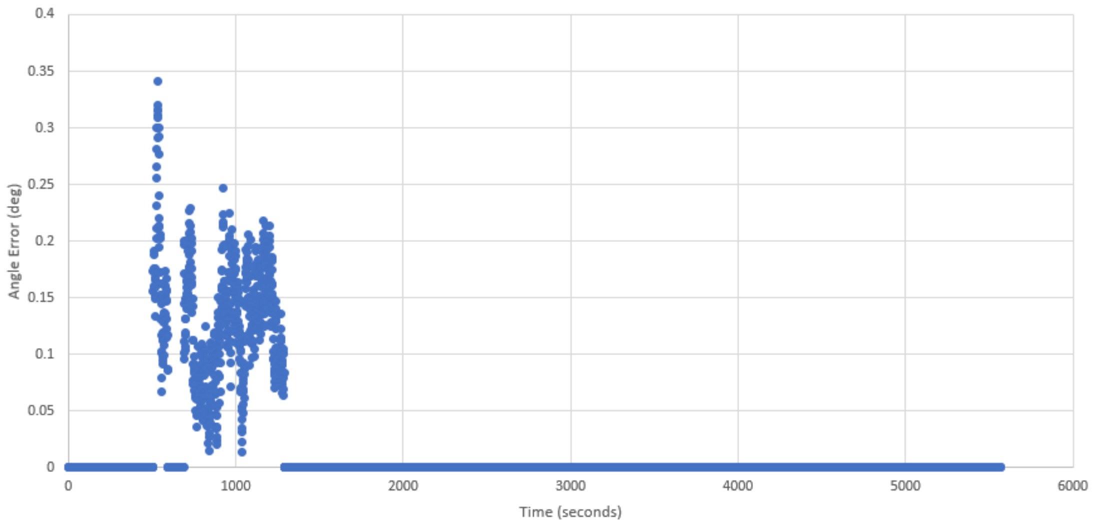

Figure 3.27: Simulation results for nadir vector angle measurement error

Table 3.21: Maximum and mean errors for nadir sensor

Sensor	Max Error	Mean Error
Nadir Sensor	0.3410738	0.114384796

The simulation results for pointing error across and around star tracker FoV is presented in Figure 3.28. Maximum and mean errors for across and around star tracker FoV are given in Table 3.22.

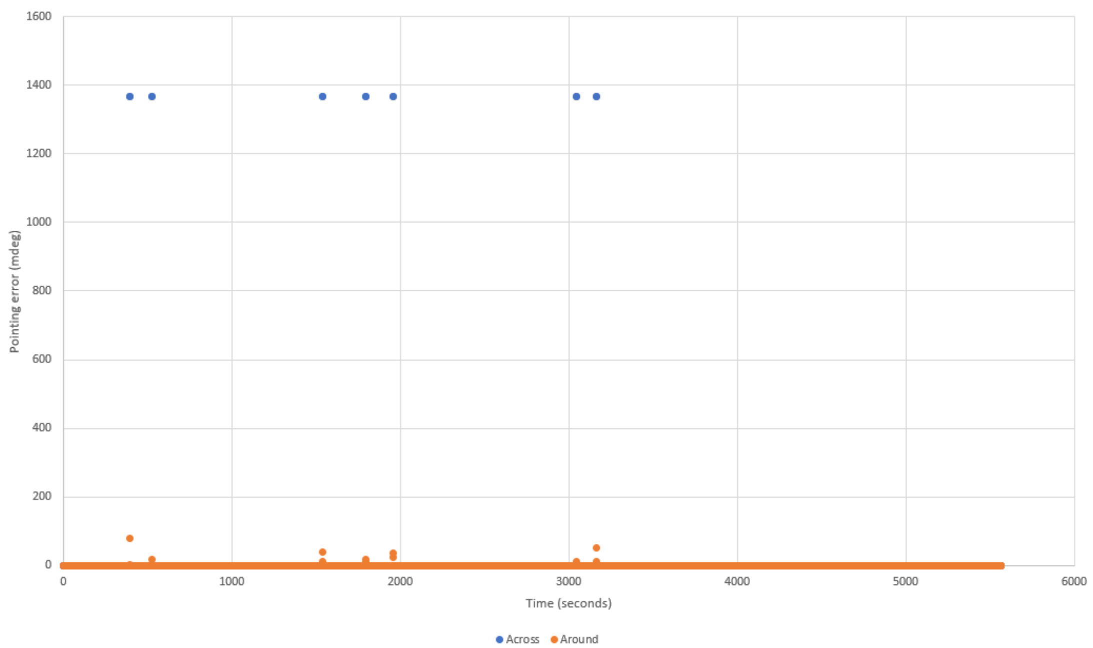

Figure 3.28: Simulation results for pointing error across and around star tracker FoV

Table 3.22: Maximum and mean errors for across and around star tracker FoV

Sensor	Max Error	Mean Error
Across	1368.437000	1368.305786
Around	80.524440	23.111083

3.3.4 Telecommands and telemetries used for ADCS

Telecommands which are sent from GS side for ADCS operations are represented in Table 3.23.

Table 3.23: List of telecommands

ID	Name	Description
1	Reset	Performs a reset
2	Current Unix Time	Current Unix Time
7	Deploy Magnetometer Boom	Deploy magnetometer boom
9	Unix Time Save to Flash	Configuration settings for Unix time flash memory persistence
10	ADCS Run Mode	Set ADCS enabled state & control loop behaviour
11	ADCS Power Control	Control power to selected components
13	Set Attitude Control Mode	Set attitude control mode
14	Set Attitude Estimation Mode	Set attitude estimation mode
15	Commanded Attitude Angles	Commanded attitude angles
16	Set Magnetorquer Output	Set magnetorquer output (only valid if Control Mode is None)
17	Set Wheel Speed	Set wheel speed (only valid if Control Mode is None)
20	ADCS Configuration	Current configuration
21	Set Magnetorquer Configuration	Set magnetorquer configuration parameters
22	Set Wheel Configuration	Set wheel configuration parameters
23	Set Rate Gyro Configuration	Set rate gyro configuration parameters
24	CSS Configuration	Photodiode pointing directions and scale factors

Table 3.23 (continued): List of telecommands

ID	Name	Description
25	CubeSense Configuration	CubeSense configuration parameters
26	Magnetometer Configuration	Magnetometer configuration parameters
27	Estimation Parameters	Estimation noise covariance and sensor mask
28	Augmented-SGP4 Parameters	Settings for GPS augmented SGP4
30	ADCS System Configuration	Current hard-coded system configuration
34	Inertial Pointing Reference Vector	Reference unit vector for inertial pointing control mode
36	Redundant Magnetometer Configuration	Redundant magnetometer configuration parameters
37	Set Star Tracker Configuration	Set configurations of CubeStar
38	Set Detumbling Control Parameters	Set controller gains and reference values for Detumbling control mode
39	Set Y-Wheel Control Parameters	Set controller gains and reference value for Y wheel control mode
40	Set Reaction Wheel Control Parameters	Set controller gains and reference value for reaction wheel control mode
41	Moment of Inertia Matrix	Satellite moment of inertia matrix
45	SGP4 Orbit Parameters	SGP4 Orbit Parameters
54	Set Tracking Controller Gain Parameters	Set controller gains for tracking control mode
55	Tracking Controller Target Reference	Target reference for tracking control mode
56	Set Mode of Magnetometer Operation	Use of main or redundant magnetometer
63	Save Configuration	Save current configuration to flash memory
64	Save Orbit Parameters	Save current orbit parameters to flash memory
80	Save Image	Save and capture image from one of CubeSense cameras or CubeStar camera to SD card
33	Format SD card	Formats SD card

Table 3.23 (continued): List of telecommands

ID	Name	Description
104	SD Log1 Configuration	Log selection and period for LOG1
105	SD Log2 Configuration	Log selection and period for LOG2
108	Erase File	Erases a file

Telemetries which are sent from GS side for ADCS operations are represented in Table 3.24.

Table 3.24: List of telemetries

ID	Name	Description
129	Boot And Running Program Status	Boot And Running Program Status
132	Current ADCS State	Current state of the Attitude Control Processor frame 1
135	CubeACP State	Contains flags regarding the state of the ACP
136	Set Magnetorquer Configuration	Set magnetorquer configuration parameters
137	Set Wheel Configuration	Set wheel configuration parameters
138	Set Rate Gyro Configuration	Set rate gyro configuration parameters
139	CSS Configuration	Photodiode pointing directions and scale factors
140	Current Unix Time	Current Unix Time
145	Unix Time Save to Flash	Configuration settings for Unix time flash memory persistence
146	Estimated Attitude Angles	Estimated attitude angles
147	Estimated Angular Rates	Estimated angular rates relative to orbit reference frame
148	Satellite Position (ECI)	Satellite position in ECI frame
149	Satellite Velocity (ECI)	Satellite velocity in ECI frame
150	Satellite Position (LLH)	Satellite position in WGS-84 coordinate frame
151	Magnetic Field Vector	Measured magnetic field vector
152	Coarse Sun Vector	Measured coarse sun vector
153	Fine Sun Vector	Measured fine sun vector
154	Nadir Vector	Measured nadir vector

Table 3.24 (continued): List of telemetries

ID	Name	Description
155	Rate Sensor Rates	Rate sensor measurements
156	Wheel Speed	Wheel speed measurement
157	Magnetorquer Command	Magnetorquer commands
158	Wheel Speed Commands	Wheel speed commands
159	IGRF Modelled Magnetic Field Vector	IGRF modelled magnetic field vector (orbit frame referenced)
160	Modelled Sun Vector	Modelled sun vector (orbit frame referenced)
161	Estimated Gyro Bias	Estimated rate sensor bias
162	Estimation Innovation Vector	Estimation innovation vector
163	Quaternion Error Vector	Quaternion error vector
164	Quaternion Covariance	Quaternion covariance
165	Angular Rate Covariance	Angular rate covariance
166	Raw Cam2 Sensor	Cam2 sensor capture and detection result
167	Raw Cam1 Sensor	Cam1 sensor capture and detection result
168	Raw CSS 1 to 6	Raw CSS measurements 1 to 6
169	Raw CSS 7 to 10	Raw CSS measurements 7 to 10
170	Raw Magnetometer	Raw magnetometer measurements
171	CubeSense1 Current Measurements	CubeSense1 current measurements
172	CubeControl Current Measurements	CubeControl current measurements
173	Wheel Currents	XYZ Wheel current measurement
174	ADCS Temperatures	Magnetometer + MCU temperature measurements
175	Rate sensor temperatures	Rate sensor temperatures
195	Power and Temperature Measurements	Power and temperature measurements
198	ADCS Misc Current Measurements	CubeStar and Torquer current and temperature measurements
181	Star 1 Body Vector	Star 1 Body Vector
182	Star 2 Body Vector	Star 2 Body Vector
183	Star 3 Body Vector	Star 3 Body Vector
184	Star 1 Orbit Vector	Star 1 Orbit Vector

Table 3.24 (continued): List of telemetries

ID	Name	Description
185	Star 2 Orbit Vector	Star 2 Orbit Vector
185	Star 3 Orbit Vector	Star 3 Orbit Vector
187	Star Magnitude	Instrument magnitude of identified stars
188	Star Performance1	Performance parameters of star measurement
189	Star Timing	Timing information of star measurement
190	ADCS State	Current ADCS state
191	ADCS Measurements	Calibrated sensor measurements
192	Actuator Commands	Actuator commands
193	Estimation Data	Estimation meta-data
194	Raw Sensor Measurements	Raw sensor measurements
197	ADCS Power Control	Control power to selected components
199	Commanded Attitude Angles	Commanded attitude angles
200	Tracking Controller Target Reference	Target reference for tracking control mode
201	Fine Estimated Angular Rates	High resolution estimated angular rates relative to orbit reference frame
202	Set Star Tracker Configuration	Set configurations of CubeStar
203	CubeSense Configuration	CubeSense configuration parameters
204	Magnetometer Configuration	Magnetometer configuration parameters
205	Redundant Magnetometer Configuration	Redundant magnetometer configuration parameters
206	ADCS Configuration	Current configuration
207	SGP4 Orbit Parameters	SGP4 Orbit Parameters
208	Set Detumbling Control Parameters	Set controller gains and reference values for Detumbling control mode
209	Set Y-Wheel Control Parameters	Set controller gains and reference value for Y wheel control mode – Table 196: Set Y-Wheel Control Parameters Message Format
211	Raw Star Tracker	Raw Star Tracker Measurement
212	Star 1 Raw Data	Catalogue index and detected coordinates for star 1

Table 3.24 (continued): List of telemetries

ID	Name	Description
213	Star 2 Raw Data	Catalogue index and detected coordinates for star 2
214	Star 3 Raw Data	Catalogue index and detected coordinates for star 3
215	Secondary Magnetometer Raw Measurements	Secondary Magnetometer raw measurements
216	Raw Rate Sensor	Raw rate sensor measurements
217	Set Reaction Wheel Control Parameters	Set controller gains and reference value for reaction wheel control mode
218	Estimated Quaternion	Estimated quaternion set
219	ECEF Position	Satellite position in ECEF coordinates
221	Set Tracking Controller Gain Parameters	Set controller gains for tracking control mode
222	Moment of Inertia Matrix	Satellite moment of inertia matrix
223	Estimation Parameters	Estimation noise covariance and sensor mask
224	Current ADCS State 2	Current state of the Attitude Control Processor – frame 2
225	ADCS System Configuration	Current hard-coded system configuration
227	Augmented-SGP4 Parameters	Settings for GPS augmented SGP4
228	ASGP4 TLEs	ASGP4 TLEs generated
229	CubeStar Estimated Rates	Angular rates estimated by CubeStar
230	CubeStar Estimated Quaternion	Attitude quaternion estimated by CubeStar
235	SD Log1 Configuration	Log selection and period for LOG1
236	SD Log2 Configuration	Log selection and period for LOG2
238	Inertial Pointing Reference Vector	Reference unit vector for inertial pointing control mode

3.3.5 ADCS flowcharts implemented in SharjahSat-1

The ADCS flowcharts in this section are implemented in the satellite OBC SW. Telemetries and telecommands which are mentioned within these flowcharts are represented in Table 3.23 and Table 3.24.

3.3.5.1 LEOP

Implemented LEOP ADCS Flowchart is given in Figure 3.29.

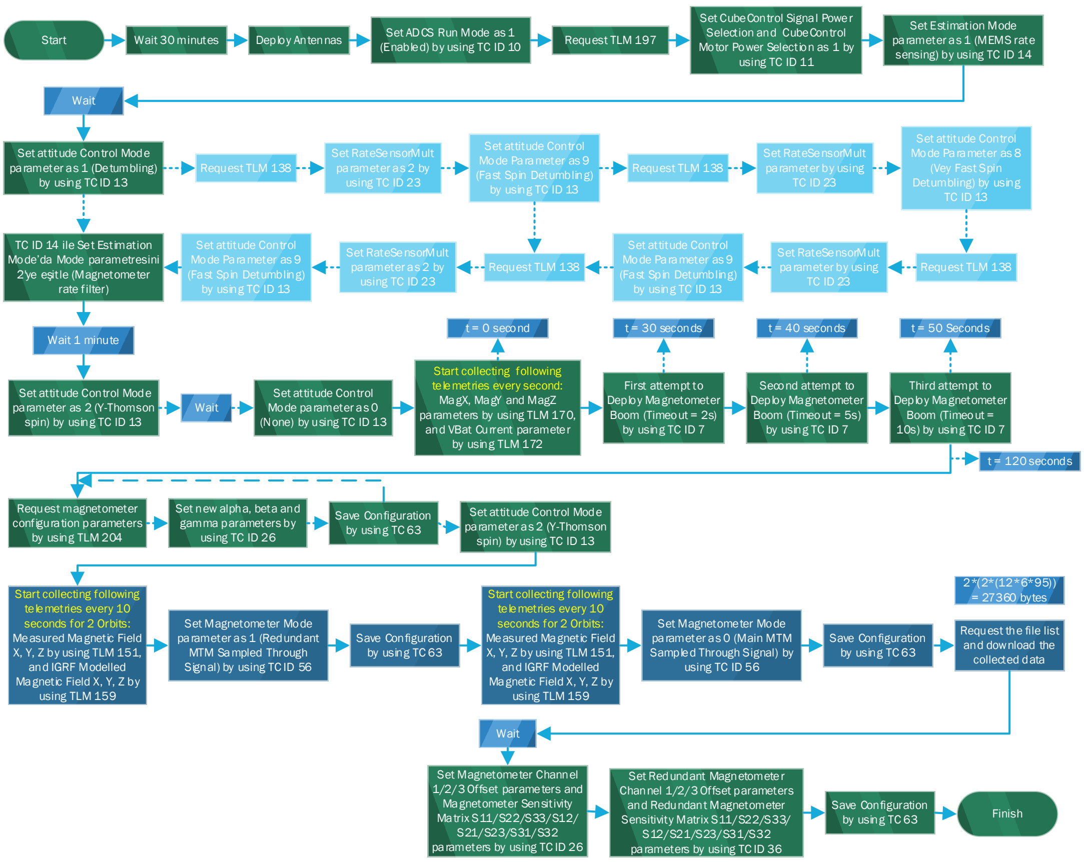

Figure 3.29 : LEOP ADCS flowcharts

Following the antenna deployment process, ADCS is turned on. After powering on essential ADCS components, estimation mode is set to MEMS rate sensing mode. At this point GS communication needs to be done in order to continue to LEOP. During the GS communication, if angular rates of the satellite are observed as higher than 40 degrees/second, ADCS control mode is set to fast spin detumbling or very fast spin detumbling mode to reduce the angular rates. If the angular rates are already low, these steps are skipped and ADCS estimation mode is set to Magnetometer rate filter mode. After it is observed that the estimated attitude gives a valid result, ADCS control mode is set to Y-Thomson spin. When it is confirmed that a stabilized control is obtained, ADCS control mode is set to none and magnetometer deployment process starts. In the case which magnetometer deployment does not occur, the process would be repeated few more times and if the deployment is successfully done, new magnetometer mounting angle configuration parameters are set. This process is followed by magnetometer calibration process which includes magnetic field telemetry collection, calibration on ground and magnetometer sensitivity matrix and offset parameters update. After parameter updates are confirmed, LEOP is completed.

3.3.5.2 Safe

Safe mode Flowchart for ADCS implemented in SharjahSat-1 is presented in Figure 3.30.

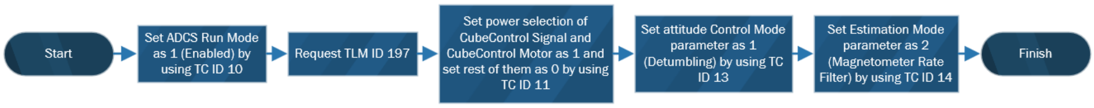

Figure 3.30 : Safe mode ADCS flowcharts

ADCS is set to detumbling control mode and magnetometer rate filter estimation mode for Safe mode since these modes requires sensors and controllers which consume less power compared to the other modes.

3.3.5.3 Sun pointing

Sun pointing flowchart for ADCS implemented in SharjahSat-1 is presented in Figure 3.31.

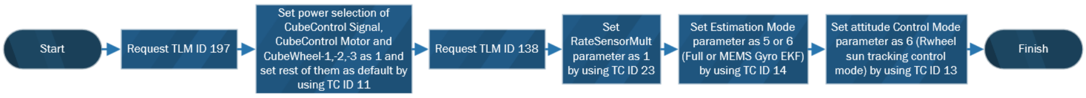

Figure 3.31 : Sun pointing mode ADCS flowcharts

After powering on the required sensors and actuators, ADCS estimation mode is set to full EKF or MEMS gyro EKF mode. Estimator needs some time to converge. Therefore, after confirming that estimator is converged, ADCS control mode is set to r-wheel Sun tracking control mode.

3.3.5.4 Transmit

Transmit mode flowchart for ADCS implemented in SharjahSat-1 is presented in Figure 3.32.

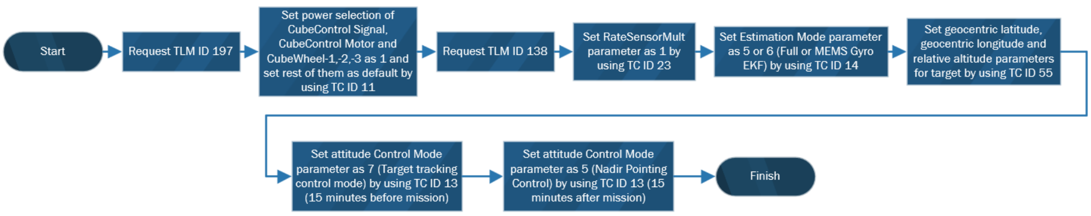

Figure 3.32 : ADCS flowcharts for transmit

Similar to the Sun pointing mode, sensors and actuators are powered on and ADCS estimation mode is set. After these, GS coordinate parameters are set. In order to achieve a stabilized control, ADCS control mode is set to target track 15 minutes prior to the start of the GS pass. ADCS control mode is set to nadir pointing, 15 minutes after GS pass is ends.

3.3.5.5 Camera

Camera mode flowchart for ADCS implemented in SharjahSat-1 is presented in Figure 3.33. Operations for camera mode are similar to transmit mode operations. Figure

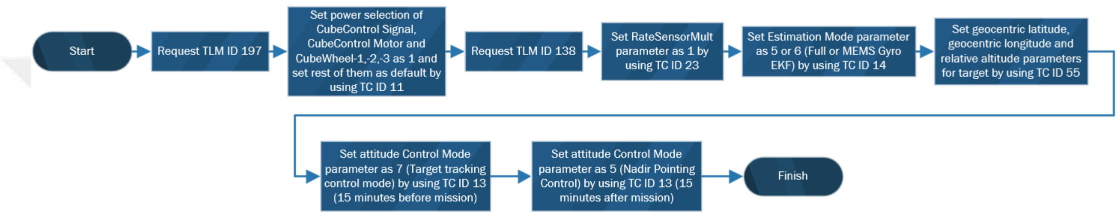

Figure 3.33 : ADCS flowcharts for camera

3.3.5.6 iXRD

iXRD mode flowchart for ADCS implemented in SharjahSat-1 is presented in Figure 3.34. Operations for camera mode are very similar to transmit and camera mode operations. Only differences are that target coordinates are defined in inertial reference frame and ADCS control mode is set to specific control mode 1 instead of target track control mode.

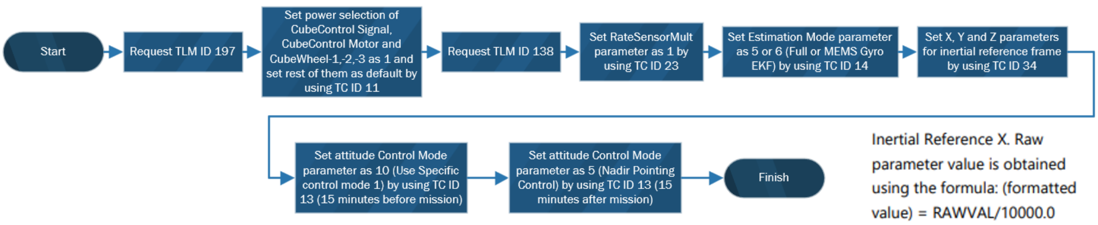

Figure 3.34 : ADCS flowcharts for iXRD

4. IN ORBIT OPERATIONS

From the date that SharjahSat-1 is deployed, many in-orbit operations are done. The logs of these operations are recorded, which are briefly represented in Figure 4.1.

Figure 4.1: SharjahSat-1 in-orbit operations throughout time

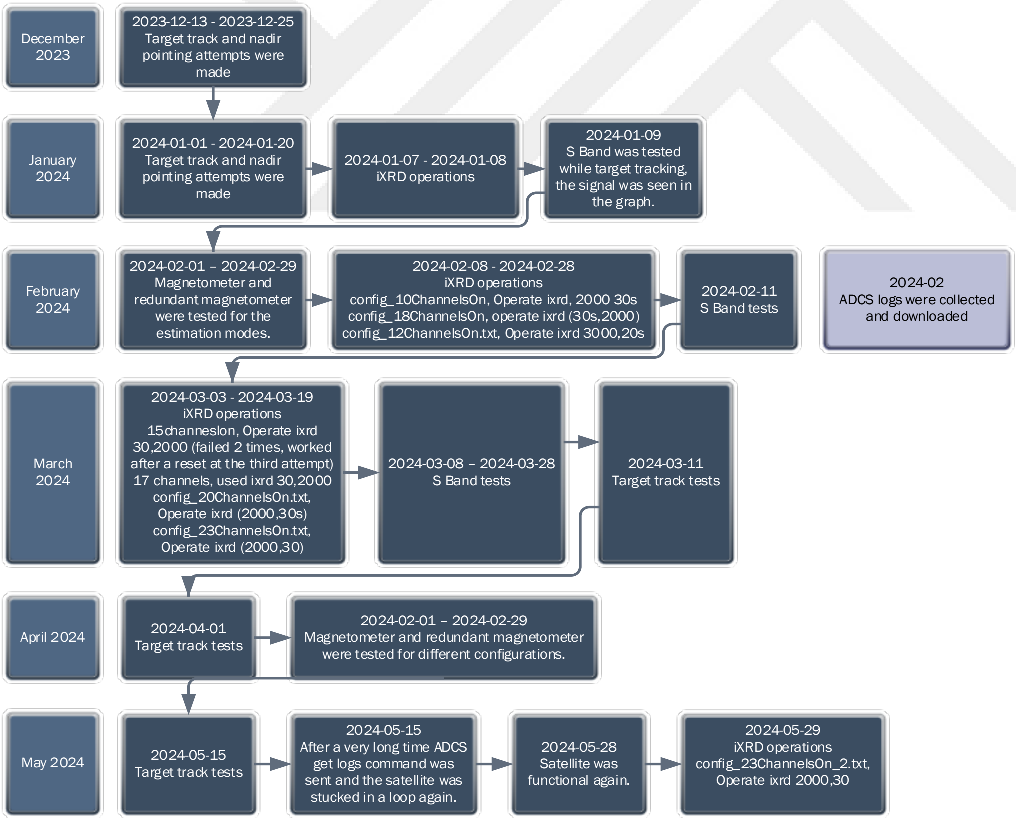

Figure 4.1 (continued): SharjahSat-1 in-orbit operations throughout time

4.1 In Orbit Scenarios

In-orbit scenarios for the SharjahSat-1 are a little bit different from the planned scenarios in the design and testing procedures.

First of all, due to the undesired attitude mode changes after a reset, attitude estimation and control modes are set by manually.

Additionally, after a reset all the configuration parameters should be sent to the satellite again. There is an automatic reset every 2 days in order to prevent the satellite OBC or any other subsystem to stay in an undesired state. Therefore, every two days, 1 or 2 GS passes are used for reconfiguration and preparation of the satellite for a specified operation. In order to not come across an unwanted reset, reset command is sent manually from GS. Also, it is observed that after a reset satellite responds faster to the commands sent from GS compared to its initial state before reset.

Before any payload operation, which require fine pointing of the satellite, angular rates should be below a certain level. Also, low angular rates are better for the downlink communication, especially when a file with large number of packages is downloaded.

Detumbling and fast detumbling attitude control mode setting flowchart is shown in Figure 4.2.

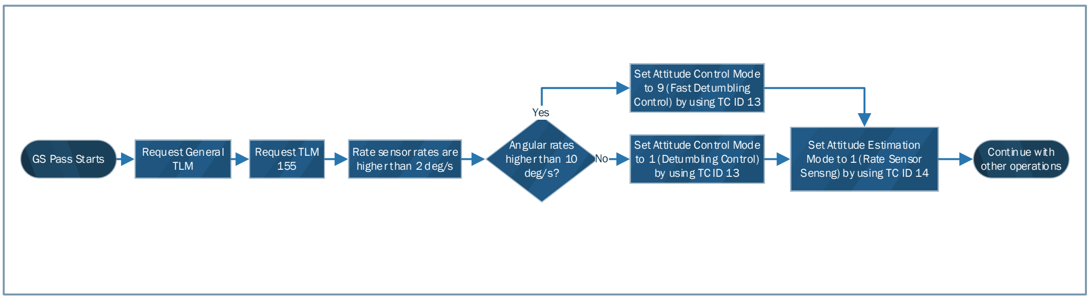

Figure 4.2: Detumbling and fast-detumbling control mode flowchart

It is recommended for the satellite, to update the TLE and time information as often as possible, especially before the operations which may require high accuracy pointing. ADCS TLE and Unix time update sequence for the satellite is presented in Figure 4.3.

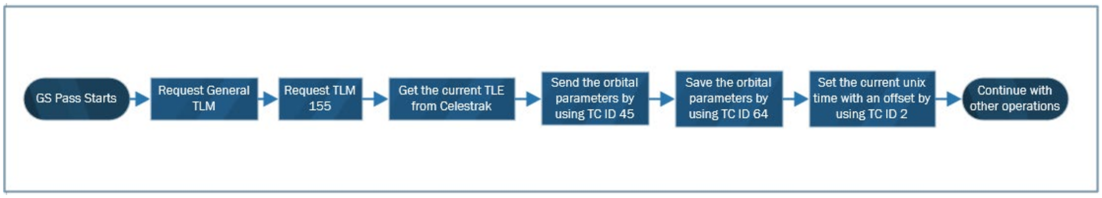

Figure 4.3: ADCS TLE and Unix time update sequence

If a payload operation will be set within next GS passes, which require nadir pointing or target tracking, previously mentioned configuration parameters should be reconfigured after the TLE and Unix time update process. The sequence is given in Figure 4.4.

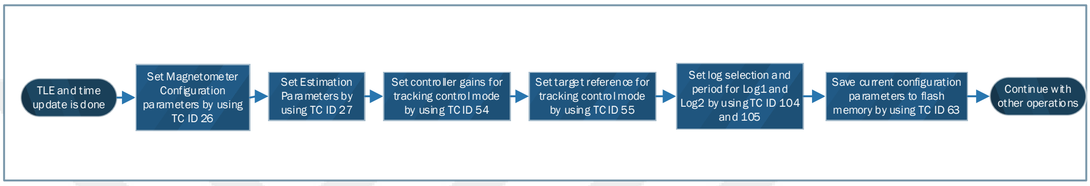

Figure 4.4: ADCS configuration set

After the angular rate of the satellite is reduced below a certain level and all the configurations are saved successfully, a mission operation for the satellite can be set. An example sequence for starting a mission that requires target tracking is presented in Figure 4.5. The mission can consist of a payload operation mission or a GS communication that requires pointing, such as S-Band operation. The configuration parameters that define the mission are set by the commands given in Figure 4.4. The wait period before ADCS xyz reaction wheel control mode should be long enough for the estimator to converge. It is an option to complete this flowchart with two GS passes: 1 pass until the “wait” and the rest in the next GS pass.

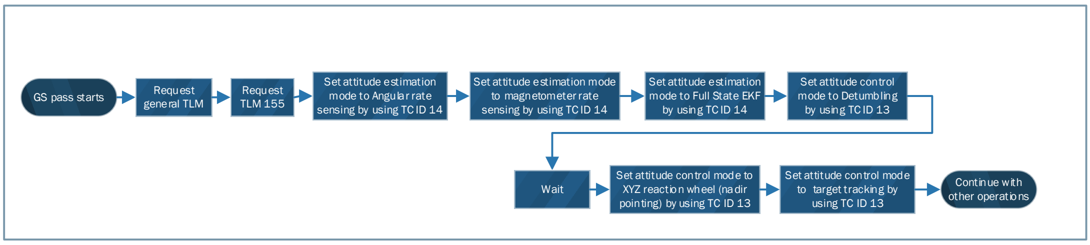

Figure 4.5: Sequence to set attitude control to target tracking

Also, after a set of data is collected, a sequence to download the data should be followed. It is described in Figure 4.6. It may take more than two passes to locate the correct data file and download it. Until the correct file is downloaded, the process is repeated.

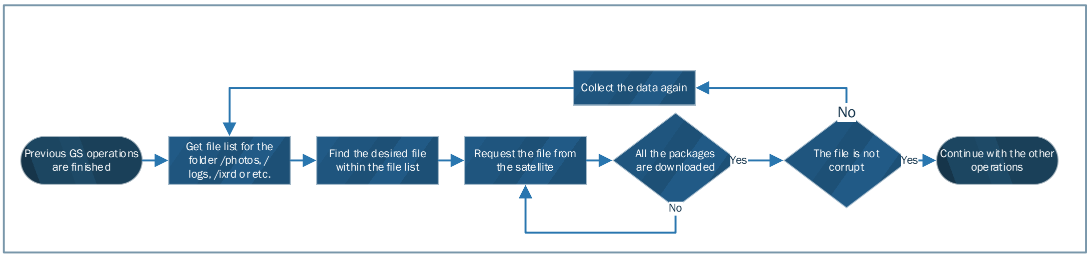

Figure 4.6: Data download sequence

4.2 In Orbit Data

From the deployment date, January 16, 2023, until today, SharjahSat-1 has been operational. Many orbital observations were done through SAASST and ITU GSs, and other ground stations around the world.

4.2.1 January 11, 2024: fast detumbling

After requesting general telemetry and rate sensor rates from the satellite, it was concluded that the satellite was spinning at high angular rates. The angular rate in total was 48.1 degrees/second. Therefore, fast-spin detumble control mode is set. The data is collected for 225 seconds after the command was sent. The data set includes timestamps, coarse sun sensor vector measurements, fine sun sensor vector measurements, nadir sensor vector measurements, rate sensor rates measurement, estimated Euler angles, and raw coarse sun sensor measurements. Estimated angular Euler angle measurements were not changing over time, so it is assumed that the data is incorrect.

Rate sensor rate data collected in this duration is presented in Figure 4.7.

Since the detumbling control and fast detumbling control works fine and reduce the angular rates, it can be stated that the rate sensor and magnetorquer axes configurations are compatible with each other.

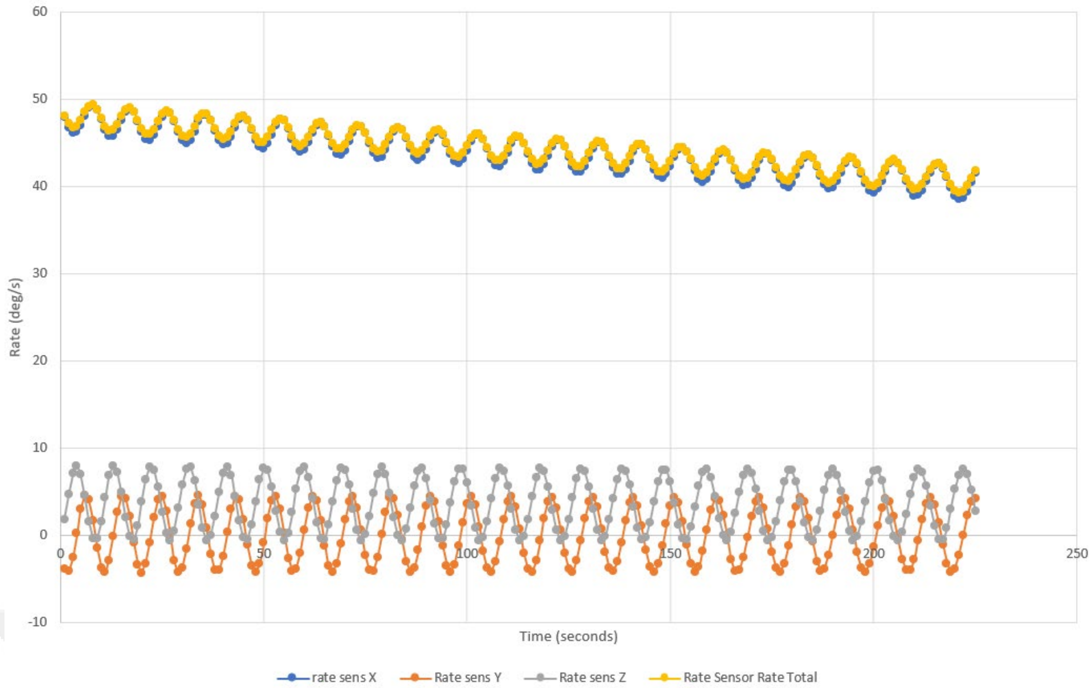

Figure 4.7: Rate sensor rate data collected by SharjahSat-1

Sun vector measurement obtained from the coarse sun sensor is presented in Figure 4.8.

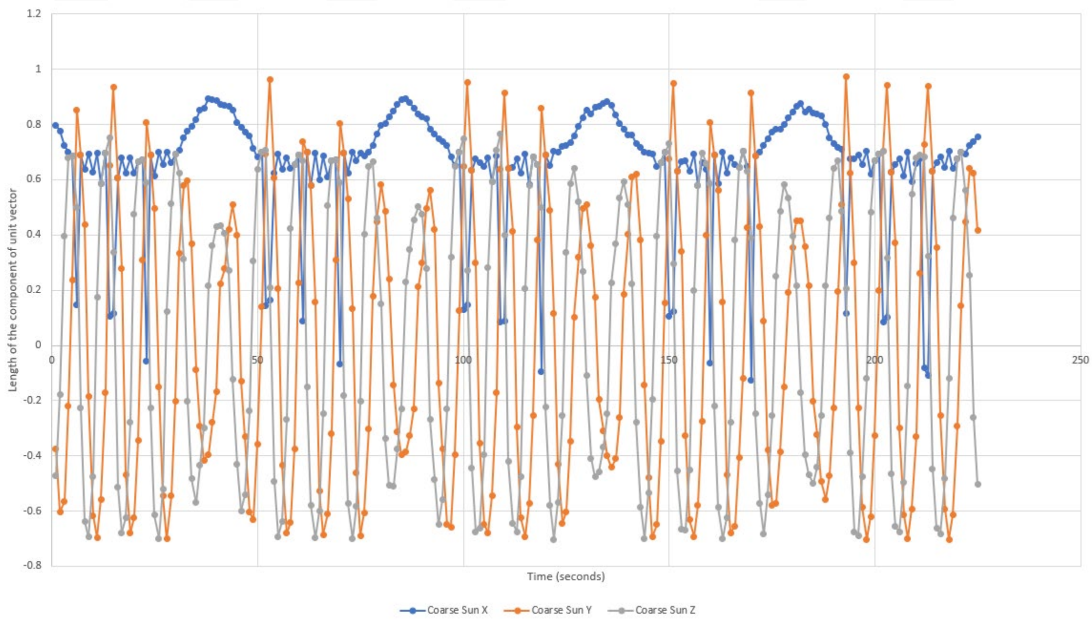

Figure 4.8: Sun vector components obtained from coarse sun sensor measurements

Since angular rates are high, fine sun sensor and nadir sensor do fewer measurements in this duration. Therefore, coarse sun sensor vector measurements are presented with the relevant fine sun sensor vector measurements in Figure 4.9.

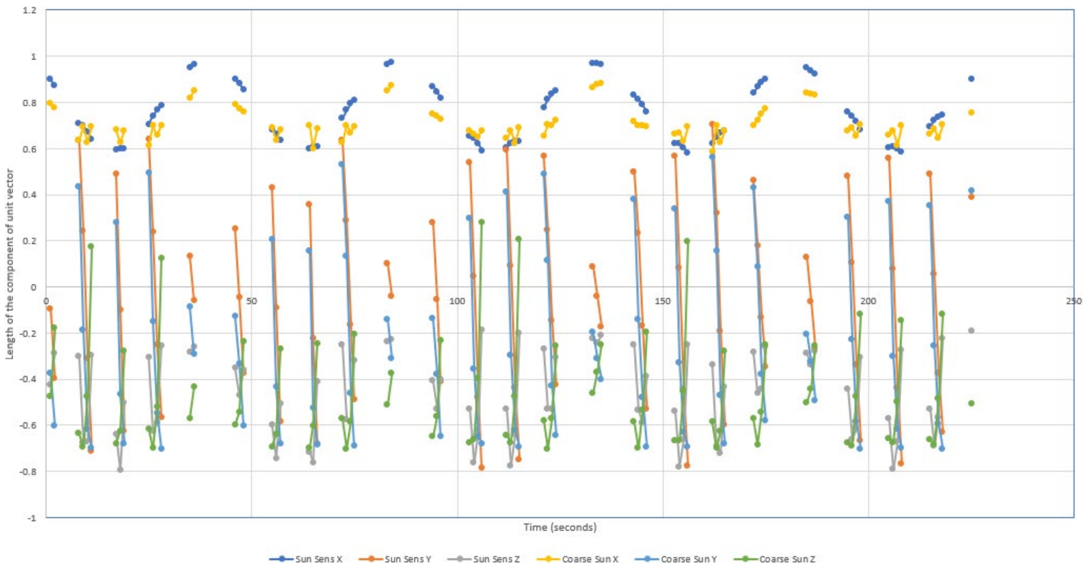

Figure 4.9: Fine Sun sensor and coarse Sun sensor measurements

Also, raw coarse sun senor measurements are presented in Figure 4.10. The order of illumination for the coarse sun sensors suggests that there is a dominant spin around X axis in positive direction., which suggests that the coarse sun sensor configurations are compatible with the satellite configuration.

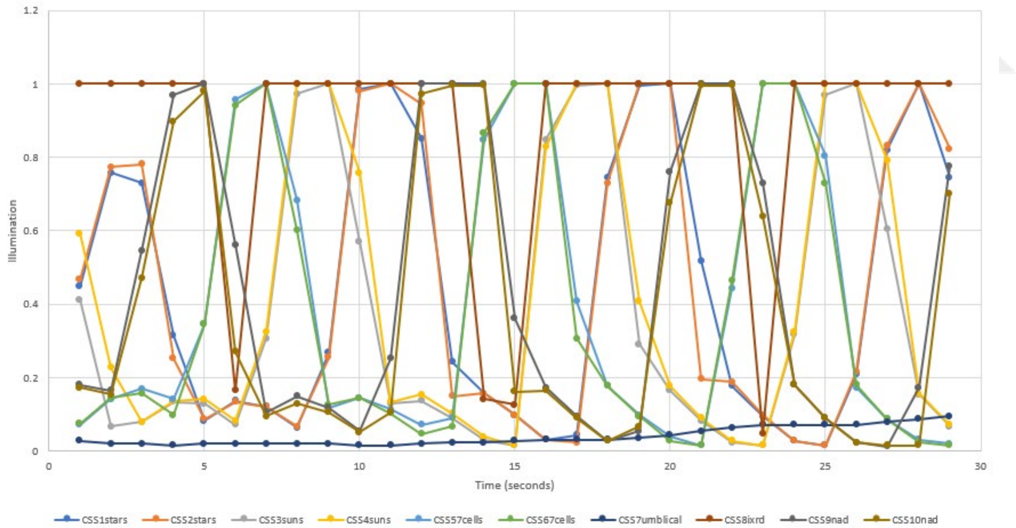

Figure 4.10: Coarse Sun sensor measurements over 30 seconds

Out of 225 timestamps, only 2 timestamps contain 2 sensor measurements.

It was observed that the detumbling control and fast spin detumbling control modes are performing well. In 1 orbit, magnetorquers can detumble the satellite from angular rates above 40 degrees/second to an angular rate below 5 degrees/second. From Figure 4.7, it can be seen that within 225 seconds, the magnetorquers detumbled the satellite from 48.1 deg/s to 41.8 deg/s.

When the angular rates of the satellite are high, fine sun sensor and nadir sensor readings are observed to be discontinuous. The reason for this is that they have a limited FoV to make the observations. From the data collected in January 11, 2024, it has been observed that within 225 seconds, nadir sensor only made 4 separate measurements, while the fine Sun sensor made 80 measurements some of which are consecutive. Out of 225 timestamps, only 2 timestamps contain 2 sensor measurements at the same time in this data set. Therefore, the data could not be used for the attitude determination.

The satellite SharjahSat-1 two-line element (TLE) information that is used within the ADCS for this telemetry collection is:

```
1 55104U 23001CZ  24009.12701412  .00007085  00000-0  35702-3 0  9994
2 55104  97.4525  69.8436 0011965  39.1343 321.0754 15.17413041 56235
```

4.2.2 February 5, 2024: XYZ wheel control, full-state EKF

In this data log, the attitude of the satellite is presented when ADCS modes are Full-State EKF and XYZ Wheel control. However, the last ADCS control mode change command sent from GS was supposed to set the control mode to fast spin detumble mode. The control mode of the satellite during the telemetry collection is probably because of an OBC reset or an ADCS reset. High angular rates of the satellite are shown in Figure 4.11 and Figure 4.12. At this case, xyz control mode would not be able to reduce the angular rates, so ADCS control mode should be set to detumbling during the next GS pass

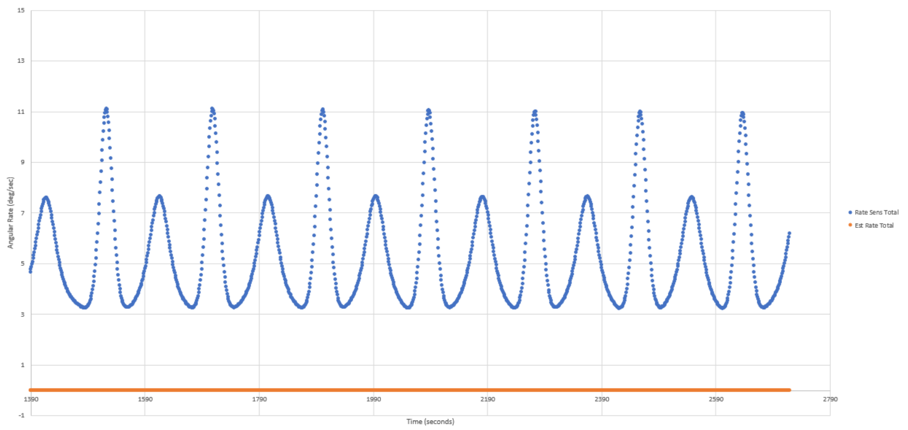

Figure 4.11: Total rate sensor rates versus estimated rates data collected by SharjahSat-1

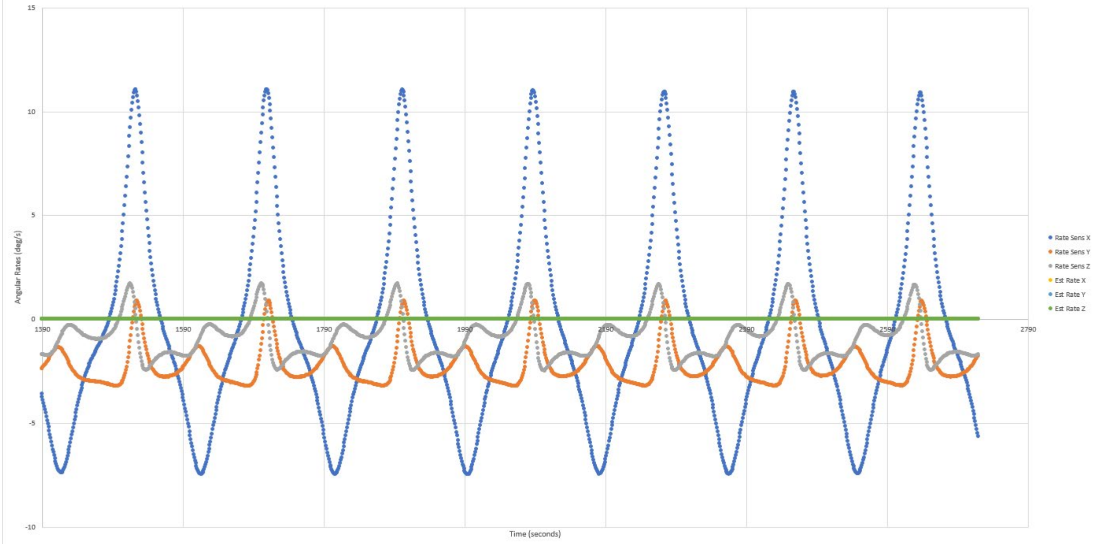

Figure 4.12: Rate sensor rates versus estimated rates data collected by SharjahSat-1

Even though it is not possible to comment solely based on magnetic field sensor measurements which are shown in Figure 4.13, total magnetic field vector calculation can be derived and compared with total IGRF magnetic field vector. In Figure 4.14, it can be seen that the magnetic field vector measurements randomly oscillate around the total IGRF magnetic field, which means the magnetometer configuration parameters are not valid and need to be updated. Since magnetometer is already calibrated before and calibration formulation is known, calibrated magnetometer measurements can be calculated on ground.

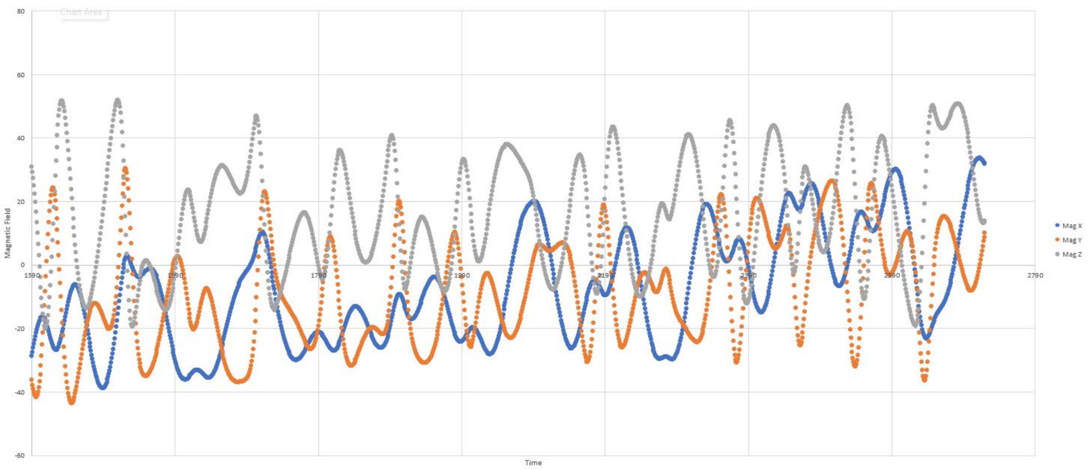

Figure 4.13: Components of the magnetic field vector measurement data collected by SharjahSat-1

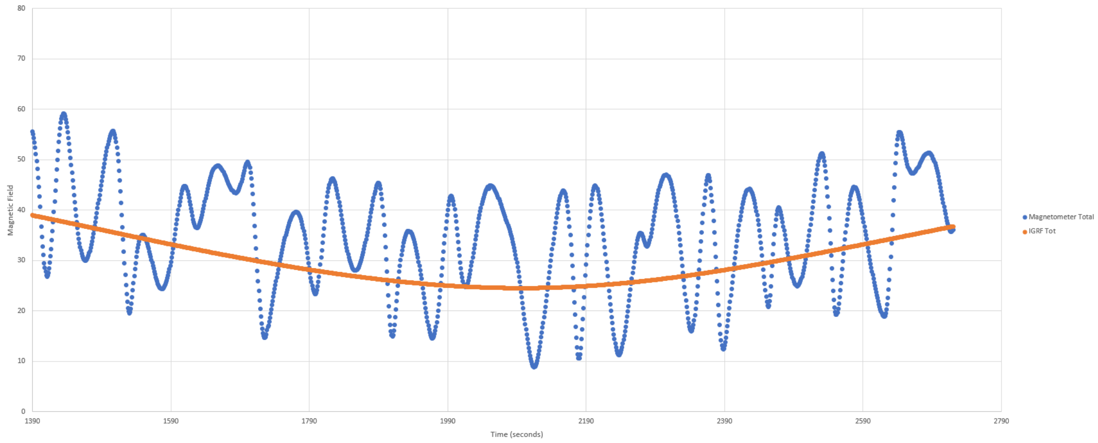

Figure 4.14: Total magnetic field data versus IGRF modelled total magnetic field data collected by SharjahSat-1

When each component of the deployable and redundant magnetometer is compared with each other in Figure 4.15, it can be seen that there is a constant difference between each same component of the redundant and deployable magnetometer. Raw magnetometer data for each component are shared in Figure 4.16, Figure 4.17, and Figure 4.18.

Figure 4.15: Raw magnetic field measurement data of deployable and redundant magnetometer collected by SharjahSat-1

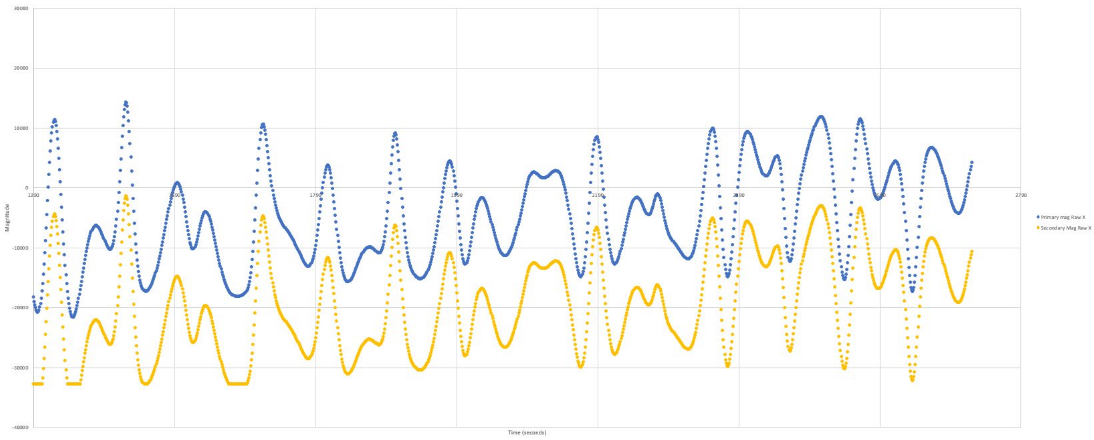

Figure 4.16: X component of the raw magnetic field measurement data of deployable and redundant magnetometer collected by SharjahSat-1

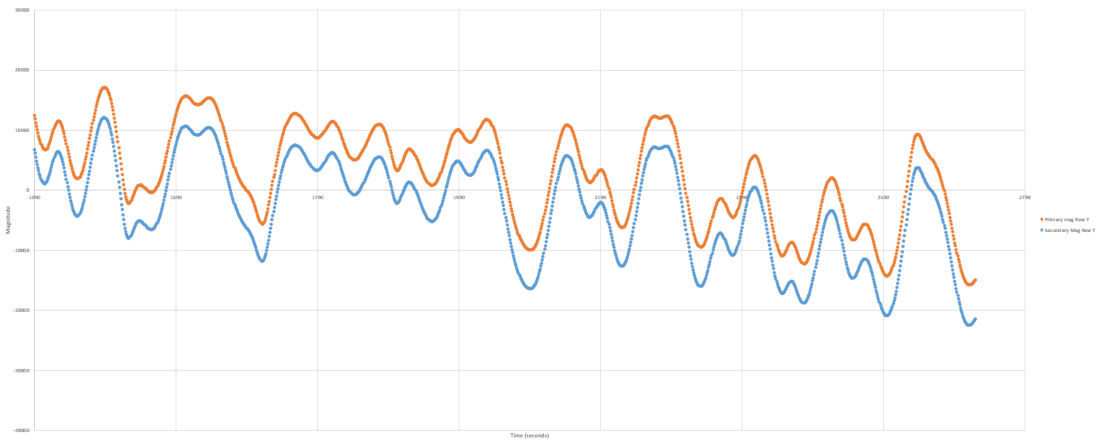

Figure 4.17: Y component of the raw magnetic field measurement data of deployable and redundant magnetometer collected by SharjahSat-1

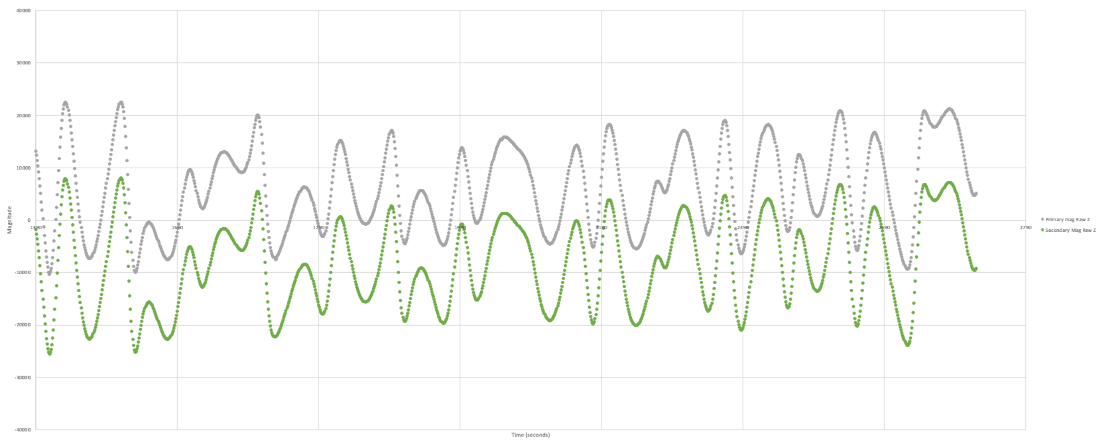

Figure 4.18: Z component of the raw magnetic field measurement data of deployable and redundant magnetometer collected by SharjahSat-1

All FSS and CSS components are shown in Figure 4.19 together. Also, each component is presented separately in Figure 4.20, Figure 4.21, and Figure 4.22. X, Y and Z components of FSS measurements match with CSS measurements. Since FSS has a limited FoV, it is normal to read Sun vector measurement as zero from time to time.

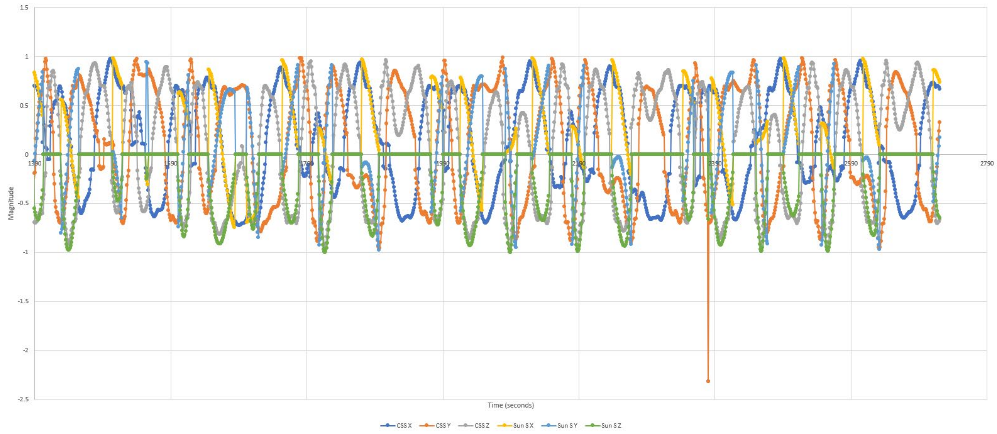

Figure 4.19: Sun vector components of CSS and FSS data collected by SharjahSat-1

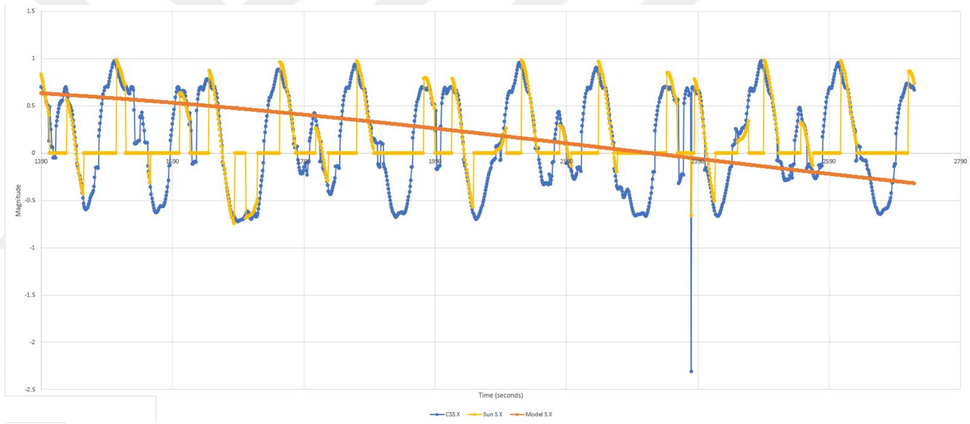

Figure 4.20: Comparison of CSS, FSS and modelled Sun vector X component collected by SharjahSat-1

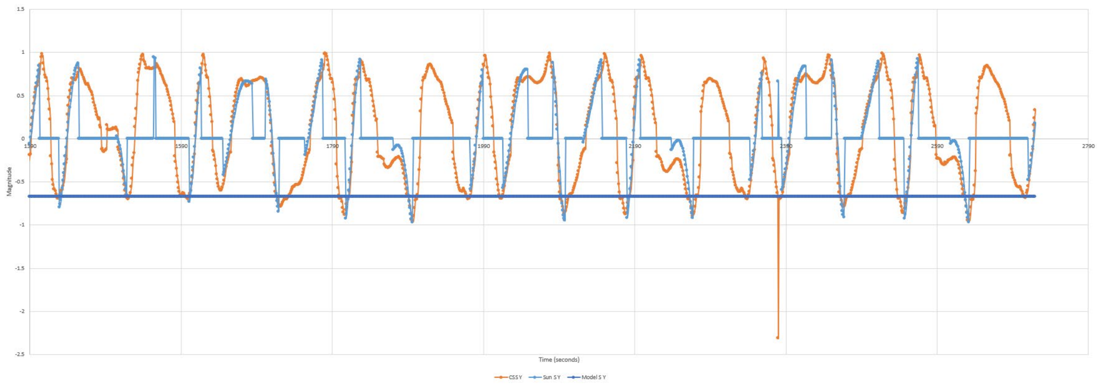

Figure 4.21: Comparison of CSS, FSS and modelled Sun vector Y component collected by SharjahSat-1

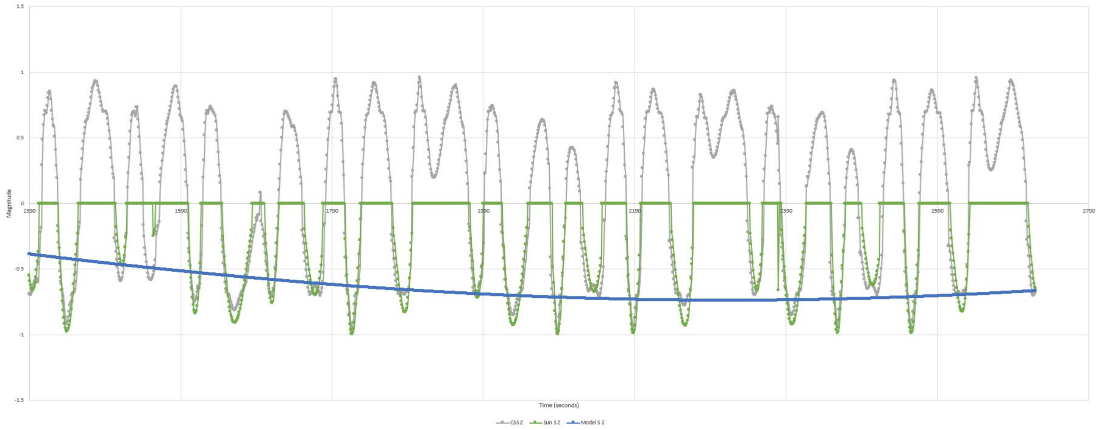

Figure 4.22: Comparison of CSS, FSS and modelled Sun vector Z component collected by SharjahSat-1

Compared to the other data sets, there are more timestamps with two sensor measurements. Even three sensor measurements within the same timestamp are present. Thus, the data is used for attitude determination algorithm.

The satellite SharjahSat-1 TLE information that is used within the ADCS for this telemetry collection is:

```
1 55104U 23001CZ 24036.42280867 .00008962 00000+0 44436-3 0 9991
2 55104 97.4478 96.6992 0009630 302.5915 57.4388 15.17922696 60379
```

4.2.3 March 4, 2024: detumbling, full-state EKF

From Figure 4.23, it is observed that the total angular rate is below 2.5 degrees /second, which is the expected behaviour from the satellite since it is in detumbling control mode.

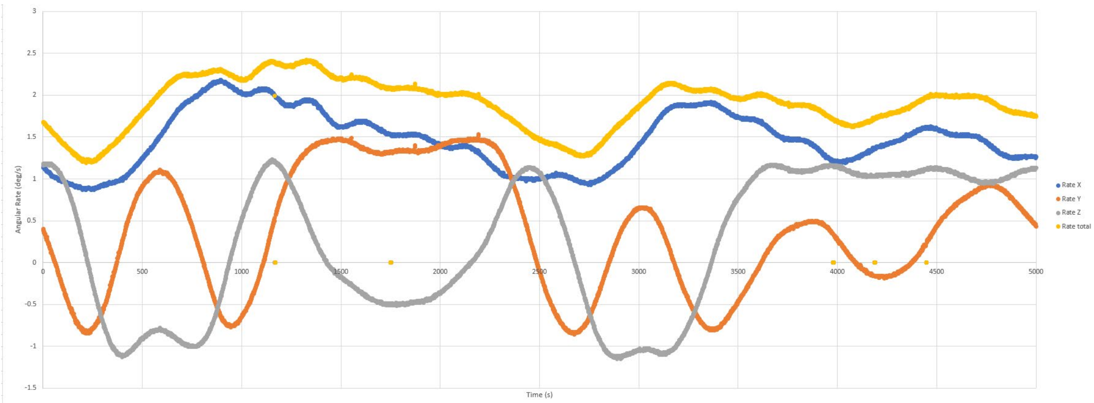

Figure 4.23: Rate sensor measurements collected by SharjahSat-1

In Figure 4.24 and Figure 4.25, FSS and nadir sensor measurements are presented. However, within this data set, magnetometer and CSS data could not be collected, so there is not enough number of data to use for the attitude determination algorithm.

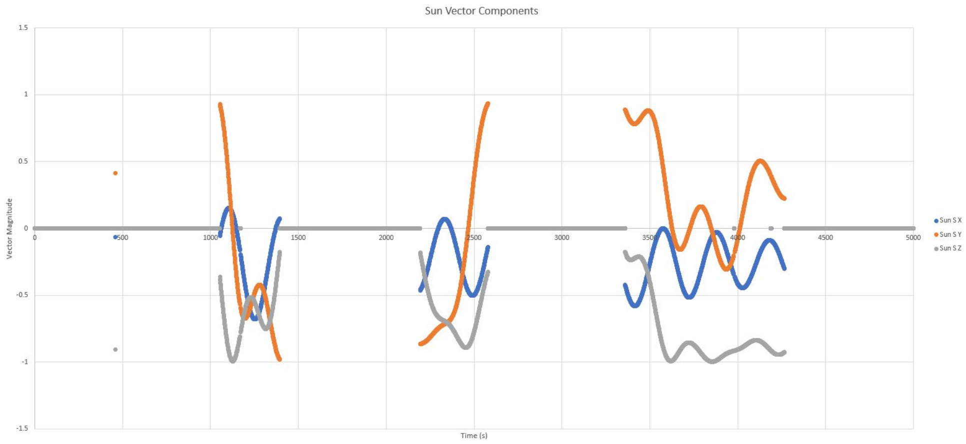

Figure 4.24: Comparison of CSS, FSS and modelled Sun vector Z component collected by SharjahSat-1

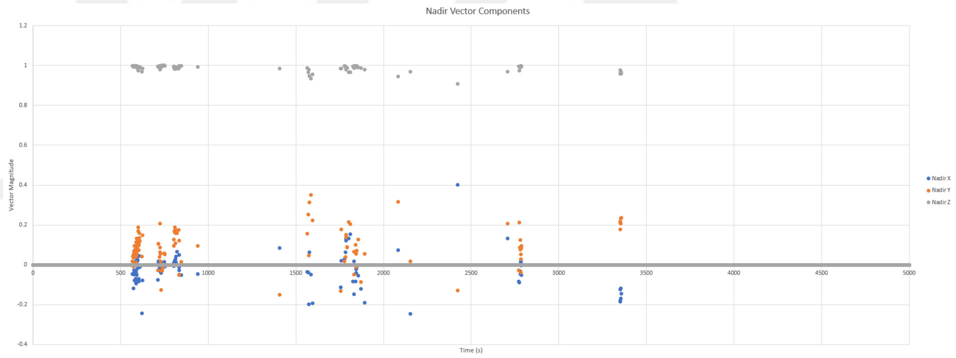

Figure 4.25: Nadir sensor measurements collected by SharjahSat-1

It can be stated that fine sun sensor is more practical compared to the nadir sensor. This can be also due to the configuration of the nadir sensor. Performance of the nadir sensor may be increased by reconfiguration; in that case it may do more observations.

Out of 5016 timestamps only 1 timestamp contains two sensor measurements which are fine Sun sensor and nadir sensor.

The satellite SharjahSat-1 TLE information that is used within the ADCS for this telemetry collection is:

```
1 55104U 23001CZ 24064.10461222 .00014865 00000-0 72255-3 0 9993
2 55104 97.4412 123.9391 0010540 194.4122 165.6813 15.18476805 64572
```

5. RESULTS AND DISCUSSION

5.1 TRIAD and QUEST Results from Modelled Sensors

Mean pitch, roll and yaw errors for TRIAD and QUEST are presented in Table 5.1. Mean errors for QUEST method are less than the mean errors for TRIAD method. When QUEST is used with three sensors, the mean errors drop significantly.

For TRIAD method, selection of magnetometer as the base vector resulted smaller mean error compared to selecting Sun sensor as the base vector. Mean errors over time for each case are presented in Figure 5.1, Figure 5.2, Figure 5.3, and Figure 5.4.

Table 5.1: Mean pitch, roll and yaw errors for different cases

	Mean Errors		
Method	**Pitch**	**Roll**	**Yaw**
TRIAD – Magnetometer and Sun Sensor	0.0963	0.0809	0.0709
TRIAD – Sun Sensor and Magnetometer	0.0918	0.0931	0.0850
QUEST– Sun Sensor and Magnetometer	0.0875	0.0639	0.0790
QUEST– Sun Sensor, Magnetometer and Nadir Sensor	0.0544	0.0528	0.0619

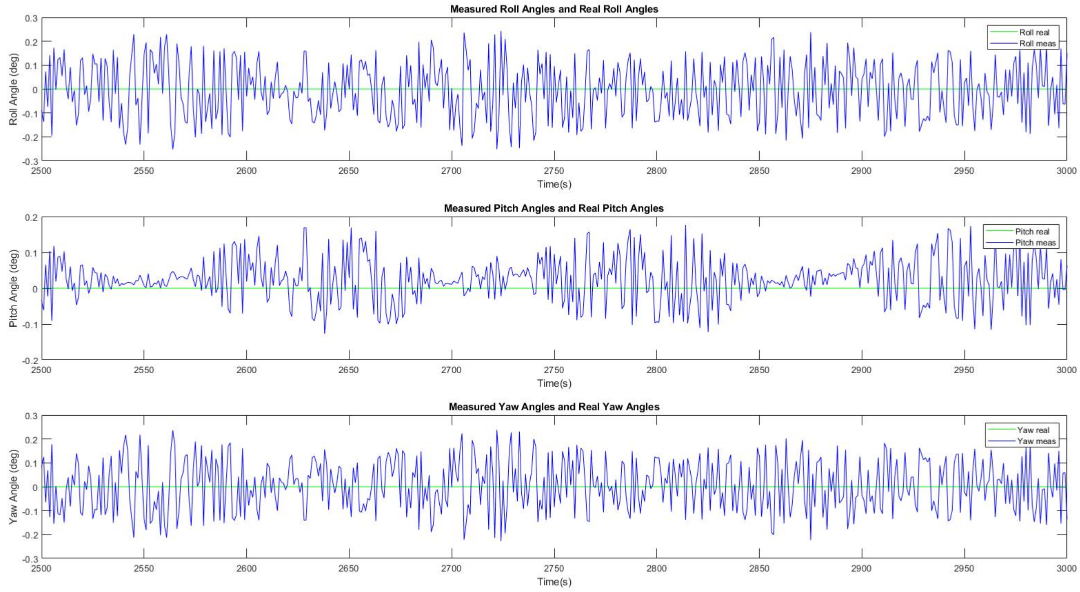

Figure 5.1: TRIAD algorithm results with modelled Sun sensor (as base) and magnetometer measurements

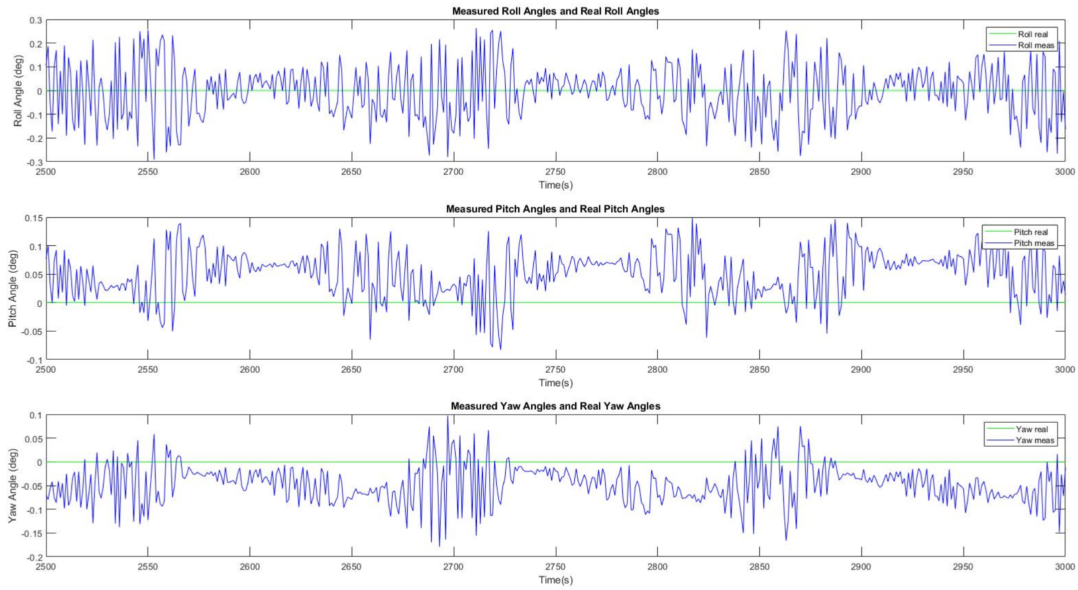

Figure 5.2: TRIAD algorithm results with modelled magnetometer (as base) and Sun sensor measurements

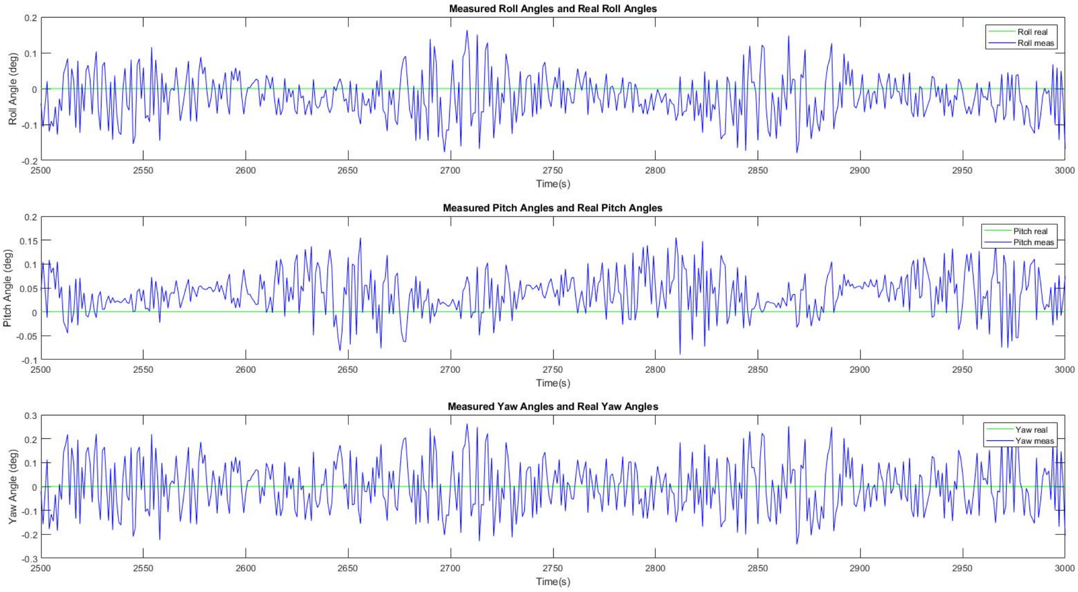

Figure 5.3: QUEST algorithm results with modelled Sun sensor and magnetometer measurements

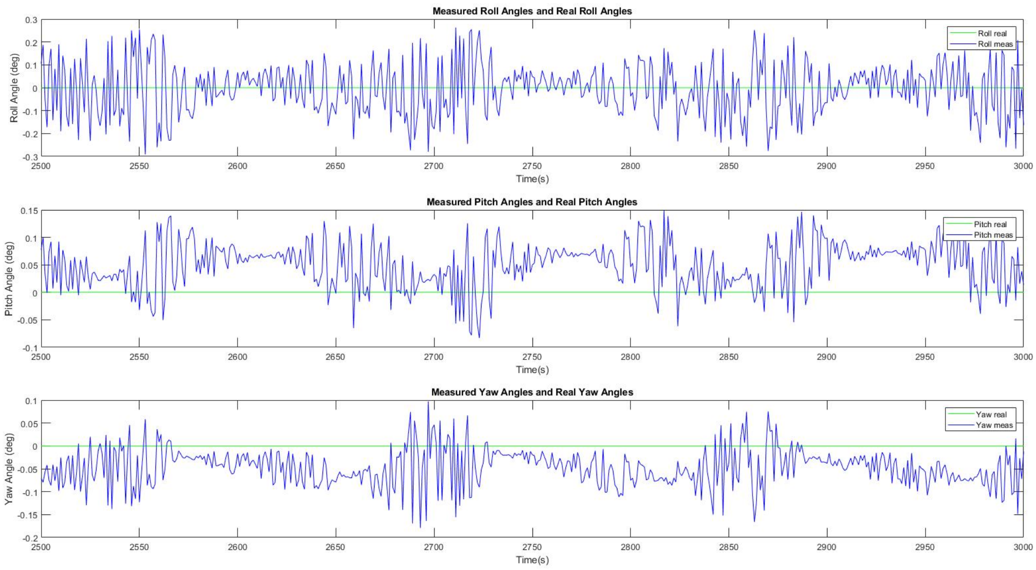

Figure 5.4: QUEST algorithm results with modelled Sun sensor, nadir sensor and magnetometer measurements

5.2 TRIAD and QUEST Results for SharjahSat-1 Telemetry

It has been already mentioned that the magnetometer data was not calibrated during telemetry logging process. Therefore, latest valid sensitivity matrix and offset matrix values are used and magnetometer measurements are calibrated. After this process, IGRF magnetic field vector data and magnetometer measurements are compared and it is calculated that there is a 3-second time shift in ADCS computer.

Magnetometer, CSS and FSS measurements are used as sensor inputs for TRIAD and QUEST algorithms. Since nadir sensor measurements are not consistent enough, it was not possible to use them as input parameters.

The results from the TRIAD algorithm when magnetometer is selected as base measurement vector are presented in Figure 5.5 and Figure 5.6. Even though there are visible differences in attitude determination between two figures, the graphs follow a similar pattern. Difference between the accuracies of the sensors may be the cause of this.

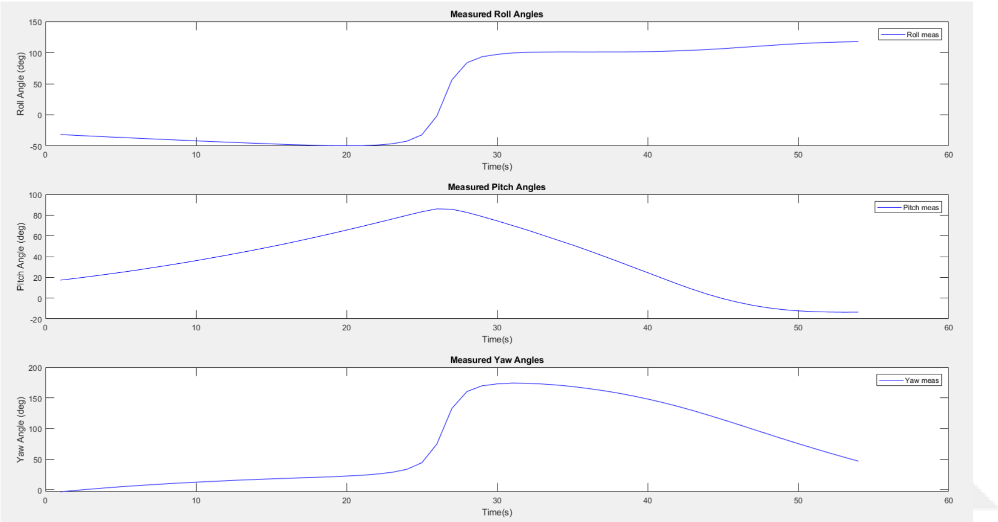

Figure 5.5: TRIAD algorithm results with magnetometer (base) and FSS measurements

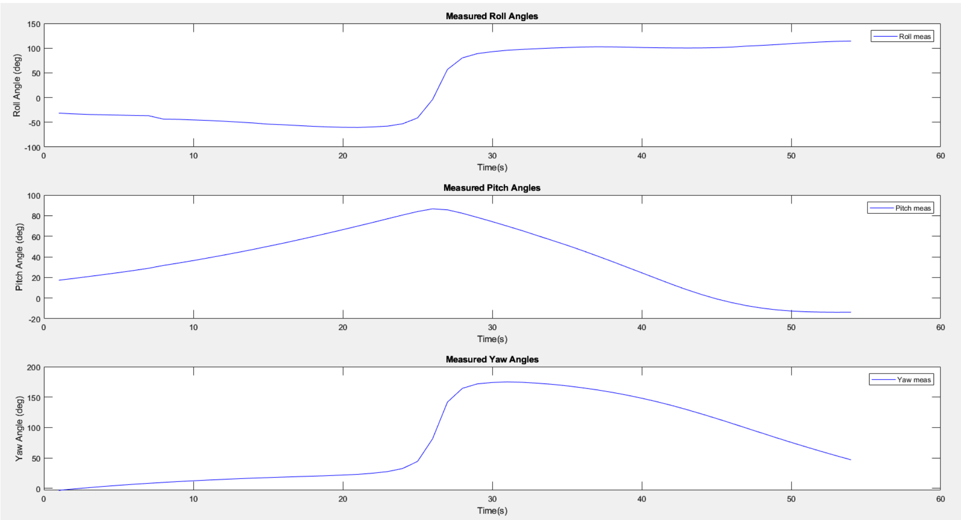

Figure 5.6: TRIAD algorithm results with magnetometer (base) and CSS measurements

Then in Figure 5.7 and Figure 5.8, the results from TRIAD when CSS and FSS are selected as the base measurement vector. Similar to the previous figures, there is a visible difference in calculated attitude but still the graphs follow a similar pattern. The fact that FSS has higher accuracy can be seen when both Sun sensors are chosen as base vectors.

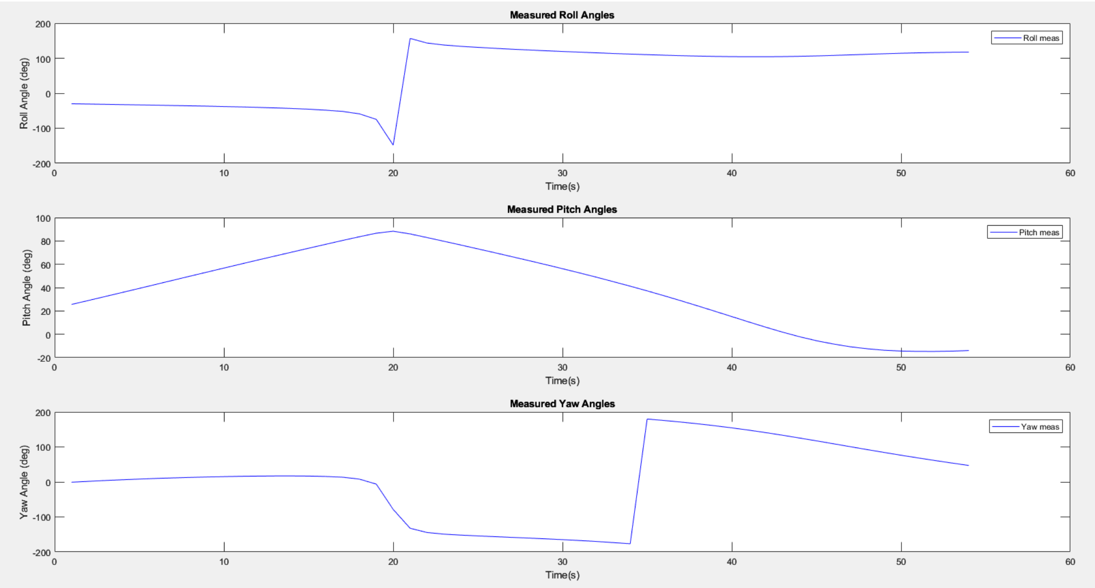

Figure 5.7: TRIAD algorithm results with FSS (base) and magnetometer measurements

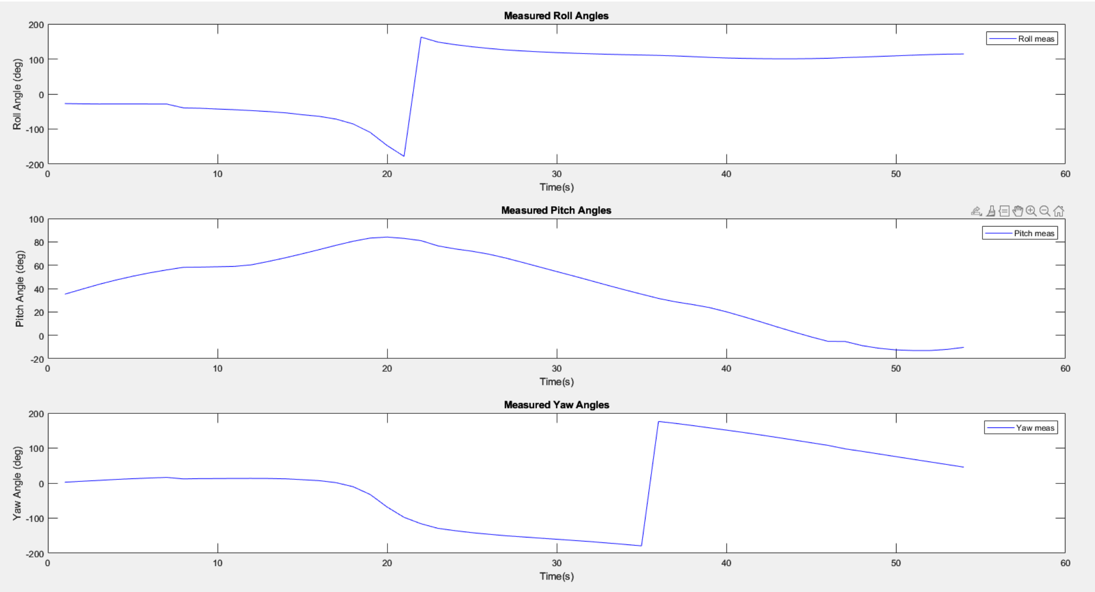

Figure 5.8: TRIAD algorithm results with CSS (base) and magnetometer measurements

In Figure 5.9 and Figure 5.10, QUEST algorithm results are shown. The results are different from TRIAD algorithm which may be caused by implementation of the algorithm or reference frame rotations. It would have been good if attitude estimation data of the SharjahSat-1 were valid.

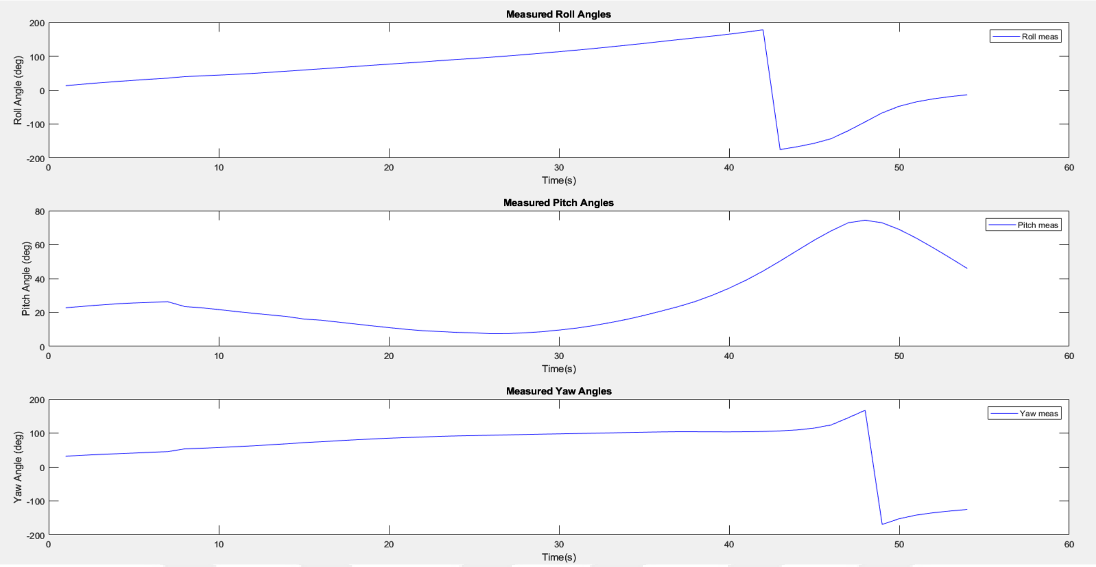

Figure 5.9: QUEST algorithm results with magnetometer and CSS measurements

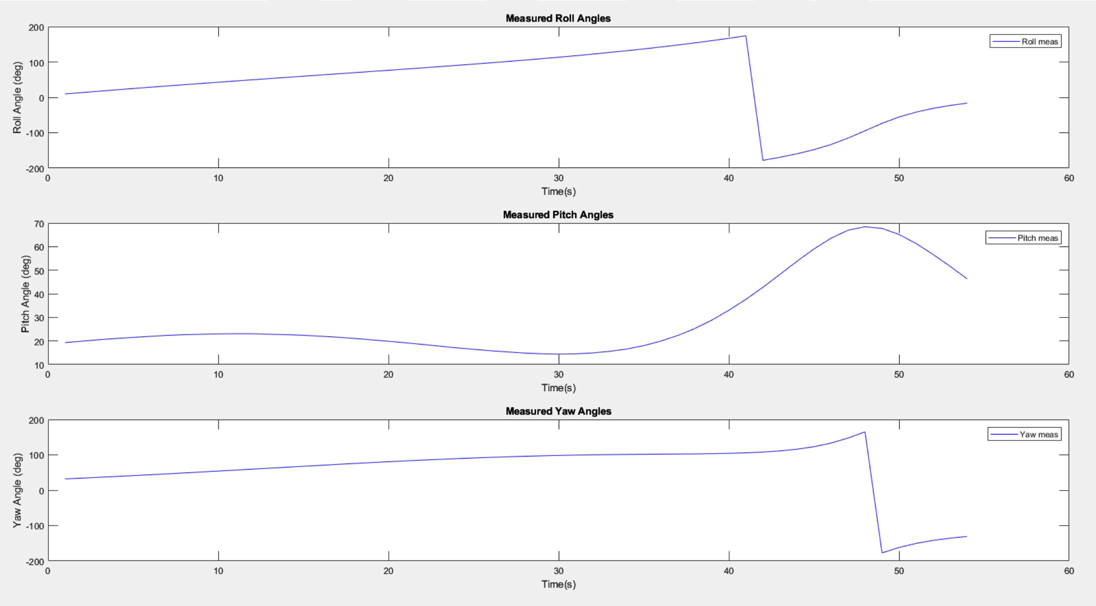

Figure 5.10: QUEST algorithm results with magnetometer and FSS measurements

6. CONCLUSION

Starting from the early development phases, many challenges are faced throughout the mission, which is normal considering the risks of the space missions and hazardous space environment. Dealing with these challenges have led to a better understanding of the satellite missions had become an important knowledge to be used in the future satellite projects. Attitude determination and control is one of the crucial aspects for the mission operations. Therefore, mission operations and planning are mostly done by focusing on ADCS, which can be seen throughout the thesis. In order to pinpoint the problem with the attitude control had required many bug fixes. Even though many of these were related to problems with hardware and software, some of these would have been resolved earlier if the issues with these were recorded during development and testing phases of the satellite. It may not seem practical to log every minor piece, but those issues that seem minor, would save a lot of time if they are recorded properly.

After dealing with all these problems, the first successful target tracking of a desired coordinate at the desired time and taking an image after a long time, have meant that even if the success rate is low, there is still hope. That very first image is shown in Figure 6.1.

Figure 6.1: Image of Van Lake taken via SharjahSat-1 (left) and image of Van Lake from map

REFERENCES

[1] **Kalemci, E., Altıngün, A. M., Bozkurt, A., Aslan, A. R., Yalçin, A., ….. Öztekin, O.** (2022). The Improved X-ray Detector iXRD on Sharjah-Sat-1, design principles, tests and ground calibration.

[2] **Aslan, A. R., AlNaimly, H. M. K., Fernini, I., Manousakis, A., Shaikh, M. & Madara, S. R.** (2019). Space Technology Capacity Building in Support of SDG 2030 Through CubeSat SharjahSat-l, *9th International Conference on Recent Advances in Space Technologies (RAST)*

[3] **Wertz, J. R.** (1978). *Spacecraft Attitude Determination and Control.* Kluwer.

[4] **Barnhart, D. J., Vladimirova, T. & Sweeting, M. N.** (2007). Very-Small-Satellite Design for Distributed Space Missions, *AIAA Journal of Spacecraft and Rockets,* vol. 44, no. 6, p. 1294–1306.

[5] **CUBESAT** (n.d.). *Cal Poly,* Retrieved September 24, 2024, from https://static1.squarespace.com/static/5418c831e4b0fa4ecac1bacd/t/62193b7fc9e72e0053f00910/1645820809779/CDS+REV14_1+2022-02-09.pdf.

[6] **Norton, C., Pellegrino, S. & Johnson, M.** (2013). Findings of the KECK Institute for Space Studies Program on Small Satellites: A Revolution in Space Science, *Proceedings of the AIAA/USU Conference on Small Satellites*, Logan, UT.

[7] **Hwang, J. T., Lee, D. Y., Cutler, J. W. & Martins, J. R. R. A.** (2013). Large-Scale Multidisciplinary Optimization of a Small Satellites Design and Operation, *AIAA Journal of Spacecraft and Rockets.*

[8] **Starin, S. R. & Eterno, J.** (2011). Spacecraft Subsystems II – Control Systems, *Space Mission Engineering: The New SMAD*, Microsm Press, p. 565–600.

[9] **Markley, F. L. & Crassidis, J. L.** (2019). Fundamentals of Spacecraft Attitude Determination, New York: Springer Science+Business Media.

[10] **Krogh, K. & Schreder, E.** (2002). Attitude Determination for AAU CubSAT, Aalborg University.

[11] **Wahba, G.** (1965). A least-squares estimate of satellite attitude, *SIAM*.

[12] **Markley, F. L.** (2002). Fast quaternion attitude estimation from two vector measurements, *Journal of Guidance, Control and Dynamics,* Vols. March-April.

[13] **Kalemci, E., Aslan, A. R., Bozkurt, A., Bas, M. E., Diba, M., ….. Ümit, E.** (2019). X-Ray Detector XRD on BeEagleSat and the Development of the Improved X-Ray Detector iXRD, *RAST*, Istanbul.

[14] **Krimm, H. A., Holland, S. T., Corbet, R. H. D., Pearlman, A. B. ….. Ukwatta, T. N.** (2013). Swift/BAT Hard X-ray Transient Monitor, *The Astrophysical Journal Supplement Series.*

[15] **ArduCAM-Mini-5MP-Plus OV5642 Camera Module** (2016). *ArduCAM*, Retrieved September 20, 2024, from https://arducam.com/downloads/shields/ArduCAM_Mini_5MP_Plus_OV5642_Camera_Module_DS.pdf.

[16] **OV2060 Color CMOS UXGA (2.0 MegaPixel) CameraChip Sensor** (2007). *ArduCAM,* Retrieved September 20, 2024, from https://www.uctronics.com/download/OV2640_DS.pdf.

[17] **CubeSat Design Specification (Revision 13)** (2014). *CUBESAT,* Retrieved September 20, 2024, from http://www.cubesat.org/

[18] **Curtis, H. D.** (2005). Orbital Mechanics for Engineering Students, Elsevier Butterworth-Heinemann, Oxford.

[19] **Javaraiah, J.** (2019). North--South Asymmetry in Solar Activity and Solar Cycle Prediction, IV: Prediction for Lengths of Upcoming Solar Cycles, *Cornell University ArXiv Solar and Stellar Astrophysics*.

[20] **Schaub, H.** (n.d.) Kinematics: Describing the Motion of Spacecraft, University of Colorado Boulder.

[21] **Hall, C. D.** (2000). Spacecraft Attitude Dynamics and Control.

[22] **Shuster, M. D. &. Oh, S. D.** (1981). Three-axis attitude determination from vector observations, *Journal of Guidance, Control, and Dynamics,* vol. 4, no. 1, p. 70–77.

[23] **Ağırbaş, A. & Aslan, A. R.** (2023) Time Shift Determination from Calibrated Magnetometer Data for CubeSats, *2nd International Graduate Research Symposium (IGRS'23)*, Istanbul.

CURRICULUM VITAE

Aybüke Ağırbaş:

EDUCATION:

- B.Sc.: 2021, Istanbul Technical University, Faculty of Aeronautics and Astronautics, Department of Astronautical Engineering

PROFESSIONAL EXPERIENCE AND REWARDS:

- 01/04/2021 – CURRENT, ADCS ENGINEER SPACE SYSTEMS DESIGN AND TESTING LABORATORY, ITUNOVA CO. INC., Istanbul, Türkiye
  - Contribution to the development and implementation of ADCS
  - Derivation of the pointing requirements from the System specification
  - Definition and development of the ADCS algorithms
  - Development of ADCS simulator in Matlab, Simulink environment
  - Providing technical expertise in troubleshooting and resolving ADCS-related issues during satellite development and operations
  - Development and performing test plans and procedures for ADCS and evaluate test results for requirements verification
  - Conducting simulations and analysis to assess the performance of ADCS under various mission scenarios
  - Supporting AIT activities on ADCS
  - Definition and development of spacecraft operational modes and modes transition
  - Definition of mission scenarios and execution of operations analysis
  - Development and analysis of failure modes and support definition and implementation of FDIR strategies and associated validation
  - Development of spacecraft nominal and off-nominal procedures
  - Investigating and resolving satellite in-orbit anomalies
  - Generating satellite performance reports and trend analysis
  - Building and editing tools to automate manual processes in satellite operations
  - Development and maintenance of operational documentation and flight procedures
  - Maintenance of accurate logs of satellite operations activities and update the logs with subsystem status changes as appropriate
  - Validation of on-orbit performance of the payload by analyzing observation data and satellite telemetry
  - Perform orbital and mission analysis (lifetime, power generation, coverage, access, attitude)

    - Support the corresponding system design reviews (PDR, CDR) and the verification planning
    - Contribution to the elaboration of proposals
    - Perform system budgets: pointing, electrical power, telemetry
    - Definition of requirements associated to spacecraft operations and FDIR aspects in system, subsystem and equipment level

- 03/08/2020 – 26/02/2021, ENGINEERING INTERN HASEFE OTO INŞAAT INDUSTRY AND TRADE LTD. CO., Kocaeli, Türkiye
    - Observing manufacturing processes of composite wind turbine blades

PUBLICATIONS, PRESENTATIONS AND PATENTS ON THE THESIS:

- 16/05/2023 – 18/05/2023, Presenter for "Time Shift Determination from Calibrated Magnetometer Data for CubeSats", 2nd International Graduate Research Symposium, Istanbul

OTHER PUBLICATIONS, PRESENTATIONS AND PATENTS:

- 01/06/2021, Manned Travel and Colonization of Mars and Effect on Astronauts, Bachelor's Thesis